Understanding the Structure – Function Relationships in Metal (Oxy)Chalcogenides: Towards the Development of Materials for Targeted Applications in Energy Conversion and Sensing

By

BRIAN ALAN WUILLE BILLE

DISSERTATION

Submitted in partial satisfaction of the requirements for the degree of

DOCTOR OF PHILOSOPHY

in

Chemistry

in the

OFFICE OF GRADUATE STUDIES

of the

UNIVERSITY OF CALIFORNIA

DAVIS

Approved:

Jesús M. Velázquez, Chair

Susan M. Kauzlarich

Frank E. Osterloh

Committee in Charge
2023

Dedication

Quiero dedicar este trabajo a mi familia, cuyo apoyo incondicional me permitió embarcar en una de las aventuras más inciertas y, a la vez, gratificantes de mi vida: Ailin, Nélida, Eduardo, no podría haber perseguido mis sueños sin ustedes. Yaki, Misha, Tita, Tigra, las llevo en mi corazón.

Acknowledgements

I am eternally grateful to my advisor, Professor Jesús Velázquez for his unwavering support throughout this journey. Through his kindness he provided a home away from home, where I could feel confident to tackle all challenges, both academic and personal. His mentorship has made an indelible mark in me, which I hope to carry on, sharing the spark of joy for science everywhere I go.

I want to thank my dissertation committee members Professor Susan Kauzlarich and Professor Frank Osterloh for their mentorship during my studies at the University of California, Davis. Their guidance has been instrumental in my growth as a scientist and in my successful navigation of the complex landscape of professional research.

This great adventure may not have started if it wasn't for the support that Professors Fernando Molina, Hernán Rodríguez, and Mercedes Perullini provided me at the University of Buenos Aires, Argentina. I am grateful for their kindness, commitment to education and for their trust in me. I also want to acknowledge Dr. Sara Bari and Dr. Andrea Montenegro for fostering my creativity and excitement for science at a very early age.

Imagination and creativity are vital for the advancement of science. Perhaps the most important of all jobs is the nurturing of these qualities in the youngest. I wholeheartedly want to thank my high school Professors: Sergio Begonja, Pablo Jung, Claudio Castaño, and Ana Krzack for believing in the excitement and curiosity of a young kid; a kid who would look forward to every laboratory time, every extra experiment, and always ask a little more. Thanks for keeping the flame alive.

I would also like to acknowledge Prof. Frank Osterloh, Prof. Charles Musgrave, Prof. Christopher Patridge, and Dr. David Prendergast for their collaborations. I want, additionally, to acknowledge Dr. Erik Nelson, Dr. Ryan Davis, and Dr. Kevin Stone for their constant support during my many trips to the Stanford Synchrotron Radiation Lightsource.

This work would not have been possible without the support of the Chemistry Department Staff. I would like to especially acknowledge Brad Wolf, Scott Berg, Marlene Slichter and Rose Smith, for their essential work to keep the department running, but more importantly, for always being available to have a talk, especially on those days when nothing worked.

Finally, I would like to thank the Velázquez research team. Their encouragement and support have made this an extraordinary experience, and I will forever treasure the moments shared.

Understanding the Structure – Function Relationships in Metal (Oxy)Chalcogenides: Towards the Development of Materials for Targeted Applications in Energy Conversion and Sensing

Abstract

With the increasing deterioration of the global climate, ushered in by fossil-fueled industrialization, a call to action is set forth to develop technologies that will transform our current manufacturing and energy landscapes into sustainable ones, where materials chemistry plays a central role. Among the biggest challenges of our time lies the realization of carbon neutral and negative emission technologies as ways to ameliorate the effects of global warming. From a materials' perspective, this realization can be achieved by the design of efficient light absorbers that can harvest intermittent sunlight, through the development of higher capacity batteries wherein this collected energy can be stored, and by the conception of selective catalyst materials that can directly or indirectly utilize renewably-sourced energy inputs to enable the conversion of molecules, whose products can act as energy vectors or replace petroleum-derived commodities. Metal chalcogenides represent a material space with apt characteristics to tackle these problems owing to the wide range of properties that sulfides, selenides, and tellurides encompass.

Chapter 1 provides a summary of the advantageous properties that metal chalcogenides present in the field of energy storage and conversion, with a focus on the fundamental principles that underpin them. Additionally, gaps in the current understanding of catalytic and sensing properties in these materials are introduced. Essential information related to important characterization techniques applied in this work is incorporated as well.

Chapter 2 delves into the study of the structural and electronic changes induced by the intercalation of transition metals into the framework of Chevrel Phase chalcogenides ($M_xMo_6T_8$, where M = transition metal, T = S, Se, Te) – a series of materials with promising applications as

catalysts and battery electrodes, for which the connection between composition and function is still poorly understood. Using X-ray absorption spectroscopy (XAS) techniques our study indicates that significant changes to the local structure of the clusters occurs upon intercalation, as evidenced by the decrease in the Mo_6 trigonal antiprism anisotropy in sulfides and selenides, and its increase in tellurides. Furthermore, the charge transfer that occurs upon intercalation is dominated by the chalcogen ions, with the molybdenum atoms remaining largely redox inactive.

Chapter 3 comprehends a thorough investigation into the structural, electronic and photophysical properties of a series of lanthanoid oxysulfides of formula $Ln_{10}S_{14}O$ (Ln = La, Ce, Pr, Nd, Sm). Reflectance spectroscopy shows that these materials have band gaps in the visible range of the electromagnetic spectrum, exhibiting n-type semiconductivity, with electrons as majority carriers, and striking long lifetimes, possibly indicating the presence of surface defects.

Chapter 4 presents the first report of the high temperature reversible thermochromism of $Ln_{10}S_{14}O$. Color space analysis determines the temperature regions in which the most dramatic color transitions occur for each lanthanoid. *In situ* X-ray diffraction experiments provide a detailed look at the evolution of the structural parameters with temperature, and calorimetric measurements show the reversibility and susceptibility of these materials to their environments between 300 °C – 600 °C.

Contents

Dedication ..... **ii**
Acknowledgements ..... **iii**
Contents ..... **vii**
List of Abbreviations ..... **ix**
List of Figures ..... **xi**
List of Tables ..... **xvi**
1. Chapter 1 – Introduction **1**
Chalcogenide Materials Design for Energy Conversion 1
Chevrel Phase Chalcogenides Composition-Function Relationship 3
Optical Thermometry in Lanthanoids 6
X-Ray Absorption Spectroscopy 7
Surface Photovoltage Spectroscopy 10
References 11
2. Chapter 2 – X-ray Absorption Spectroscopy Insights on the Structure Anisotropy and Charge Transfer in Chevrel Phase Chalcogenides **19**
Abstract 19
Introduction 19
Results and Discussion 22
Conclusions 32
Acknowledgements 32
Publication Information, Copyright, and Author Acknowledgements 33
References 34
Supporting information 37
3. Chapter 3 – $Ln_{10}S_{14}O$ (Ln = La, Pr, Nd, Sm) Oxysulfides: A Series of Direct n-Type Semiconductors **70**
Abstract 70
Introduction 70
Results and Discussion 72
Conclusions 87
Experimental Method 87
Acknowledgements 91
Publication Information, Copyright, and Author Acknowledgements 91

References 92
Supporting Information 99
4. Chapter 4 – Understanding the High-Temperature Reversible Thermochromism in $Ln_{10}S_{14}O$ **116**
Abstract 116
Introduction 116
Results and Discussion 118
Conclusions 126
Future Work 126
Experimental Method 127
Acknowledgements 129
References 129
Supporting Information 133

List of Abbreviations

AC	alternating current
CO2RR	carbon dioxide reduction reaction
CP	Chevrel Phase
CPD	contact potential difference
DASF	derivation of absorption spectrum fitting
DC	direct current
DFT	density functional theory
EDS	energy dispersive X-ray spectroscopy
EXAFS	extended X-ray absorption fine structure
FTO	fluorine-doped tin oxide
HER	hydrogen evolution reaction
ITO	indium tin oxide
KS	Kohn Sham
LIR	luminescence intensity ratio
MBXAS	many-body X-ray absorption spectroscopy
NTC	negative temperature coefficient
ORR	oxygen reduction reaction
PBE	Perdew-Burke-Ernzerhoff
PXRD	powder X-ray diffraction
RTD	resistance temperature detector
SEM	scanning electron microscopy
SPEIS	staircase potentio-electrochemical impedance spectroscopy
SPS	surface photovoltage spectroscopy
SSRL	Stanford Synchrotron Rediation Ligthsource

VEC	valence electron count
XANES	X-ray absorption near-edge structure
XAS	X-ray absorption spectroscopy
XCH	excited-electron core-hole
XPS	X-ray photoelectron spectroscopy

List of Figures

Figure 1.1. Diagram illustrating metal chalcogenides as a vessel that unlocks a multitude of beneficial properties in materials designed for energy conversion. 1
Figure 1.2. Scheme of a representative single CP cluster, showing the large compositional tunability and three common compositional handles that facilitate functional changes. 4
Figure 1.3. Schematic energy diagram showing the effect of intercalation in the Mo_6S_8 Chevrel Phase cluster electronic structure, based on Burdett et al.,[39] and Andersen et al..[40] The binary phases have 20 valence electrons, and their bonding orbitals can accommodate 4 additional electrons. A greater charge transfer from the intercalant ions into the cluster leads to destabilization of the cluster due to population of orbitals of antibonding character. 5
Figure 1.4. Example of an X-ray spectrum with its characteristic 3 regions: Pre-edge, Edge and Post-edge in increasing energy. Data corresponds to the O K-edge spectrum of $La_{10}S_{14}O$, in which the edge is characterized by multiple absorption bands associated with the crystal field splitting of the La^{3+} 5d orbitals and 6p orbitals, both hybridized with the O 2p states.[52] 8
Figure 1.5. Graphical representation of the one-body core-hole approach calculation based on a ΔSCF method. The crystal structures on the left correspond to a 2x2x2 Mo_6S_8 supercell viewed from the *a*-axis. 9
Figure 1.6. Schematic diagram of the experimental setup used in surface photovoltage spectroscopy measurements, and the contact potential difference response as a function of incident photon energy obtained for p- and n-type semiconductors, in which the majority carriers are holes and electrons, respectively. 11
Figure 2.1. Crystal structure of the rhombohedral (R-3) CPs studied herein ($Cu_2Mo_6T_8$ T = S, Se) depicting (a) an individual Mo_6T_8 cluster where the Mo atoms are represented in blue, and chalcogen atoms in gold, (b)adjacent Mo_6T_8 clusters detailing a 3-fold rotational axis where cluster-linking undercoordinated chalcogens (T_2) are represented in white, and an intercluster cavity into which metals can be intercalated, and (c) the $M_xMo_6T_8$ framework where intercalant metal atom sites are represented by magenta. 20
Figure 2.2. (a) SEM micrographs of (a) $Cu_2Mo_6S_8$, (b) $Cu_2Mo_6Se_8$ and (c) $NiMo_6Te_8$ along with their corresponding PXRD diffractograms (d)–(f). 23
Figure 2.3. Mo K-edge FT-EXAFS data (circles) and fits (solid lines) showing the non-phase-corrected magnitude (top lines) and real (bottom lines) components of the Fourier transform of $k^3\chi(k)$ in radial space for the sulfide, selenide, and telluride binary CPs (a), (c), and (e), and the Cu intercalated sulfide and selenide (b), (d), and Ni intercalated telluride CPs (f). 25

Figure 2.4. Graphic representation of the intracluster and intercluster scattering paths observed in Figure 2.3 for 1s photoelectrons between an absorbing Mo and its neighboring Mo and T ions in the CP framework. Information for each path is detailed in Table S2.1. 26
Figure 2.5. Molybdenum and chalcogen XANES spectra for binary and ternary Chevrel phases. (a) Mo L_3-edge of sulfide, selenide and telluride CPs, (b) S K-edge of Mo_6S_8 and $Cu_2Mo_6S_8$, the calculated spectra are shown with dashed lines (c) Se K-edge of Mo_6Se_8 and $Cu_2Mo_6Se_8$, and (d) Te L_3- edge of Mo_6Te_8 and $NiMo_6Te_8$. 28
Figure 3.1. (a) Unit cell of $Ln_{10}S_{14}O$ oxysulfides viewed along the c axis, represented using the corresponding ionic radii in which the yellow, red, and green circles represent S^{2-}, O^{2-}, and Ln^{3+}. (b) Structures highlighting the multiple 7- and 8-fold coordination environments surrounding the Ln(III) ions. (c) Powder X-ray diffractograms of the corresponding lanthanoid oxysulfides. 72
Figure 3.2. Non-phase-corrected lanthanoid L_3-edge FT-EXAFS fits for (a) $La_{10}S_{14}O$, (b) $Ce_{10}S_{14}O$, (c) $Pr_{10}S_{14}O$, (d) $Nd_{10}S_{14}O$, and (e) $Sm_{10}S_{14}O$. The top trace represents the magnitude of $\chi(R) \cdot k^3$, whereas the bottom constitutes its real component. 74
Figure 3.3. X-ray photoelectron spectroscopy of the Ln 3d region for (a) $La_{10}S_{14}O$, (b) $Ce_{10}S_{14}O$, (c) $Pr_{10}S_{14}O$, (d) $Nd_{10}S_{14}O$, and (e) $Sm_{10}S_{14}O$. (f) Comparison between the binding energy difference and area ratio of the satellite-to-$3d_{5/2}$ signal as a function of the lanthanoid ion. 77
Figure 3.4. (a) Digital photographs of lanthanoid oxysulfide films on ITO substrates, and their (b) diffuse reflectance UV–vis spectra (shown offset for clarity). $F(R)$ is proportional to the absorption coefficient. $F(R) = 2R/(1- R)^2$ (Kubelka–Munk function) 78
Figure 3.5. Comparison between Tauc direct, indirect, and DASF analyses for the determination of the optical band gap. The solid and dashed black lines represent linear regressions for Tauc analyses (left and middle columns) and Gaussian peak fittings for DASF analysis (right column). 82
Figure 3.6. Comparison of band gap energy values obtained through Tauc plot and DASF analysis 83
Figure 3.7. Comparison between DR UV–vis (top) and surface photovoltage spectra (bottom) of (a) $La_{10}S_{14}O$, (b) $Pr_{10}S_{14}O$, (c) $Nd_{10}S_{14}O$, and (d) $Sm_{10}S_{14}O$ films on fluorine-doped tin oxide (FTO)-coated glass slides in vacuum. ΔCPD is the contact potential difference versus the dark CPD value. For details, see the Experimental Section. Films of $Ce_{10}S_{14}O$ did not produce any photovoltage signal (Figure S3.9). 85
Figure 3.8. Photovoltage decay data of $La_{10}S_{14}O$, $Pr_{10}S_{14}O$, $Nd_{10}S_{14}O$, and $Sm_{10}S_{14}O$. (a) ΔCPD as a function of time, indicating the illumination period; (b) logarithmic plot of the normalized ΔCPD decay, and straight lines indicate linear regressions; (c) excitation and charge transfer pathways

from both band gap and sub-band gap states *E*T contribute to the surface photovoltage signal; and (d) electron transfer into surface states *E*S limits the recombination rate at t > 800 s..... 86
Figure 4.1. a) Photographs of $Ln_{10}S_{14}O$ powders showing the change in their colors as a function of temperature, obtained during the cooling cycle; b) Color space analysis plane (projected in the L = 55) for La, Ce, Pr, Nd, and Sm oxysulfides. The background color represents the observed colors, while the colors inside the scatter plot correspond to the temperature scale on the right. c) demonstrates the progressive changes in *a* and *b* CIE-Lab parameters with temperature..... 118
Figure 4.2. In situ X-ray diffractograms for a) $La_{10}S_{14}O$, b) $Ce_{10}S_{14}O$, c) $Pr_{10}S_{14}O$, d) $Nd_{10}S_{14}O$, and e) $Sm_{10}S_{14}O$. The top panels show the room temperature diffractograms, while the bottom panel in each pair represents color maps as a function of temperature. The more intense the color, the higher the intensity of the corresponding reflection. The ⁕ symbol identifies the characteristic peak of BN used as diluent. 120
Figure 4.3. Expansion of the tetragonal lattice parameters *a*, *b*, and *c* as a function of temperature for a) $La_{10}S_{14}O$, b) $Ce_{10}S_{14}O$, c) $Pr_{10}S_{14}O$, d) $Nd_{10}S_{14}O$, and e) $Sm_{10}S_{14}O$. Both lanthanum and neodymium showed the presence of a solid solution between the corresponding nominal phase and $Ln_{10}S_{14.5}O_{0.5}$, for which cases their lattice parameters are also included. $Pr_{10}S_{14}O$ data is limited to 500 °C due to oxidation happening at 600 °C because of depletion of inert gas flow in the sample cell at the time of measurement. 122
Figure 4.4. X-ray absorption near edge structure spectra corresponding to a) O K-edge, and b) S K-edge of $Ln_{10}S_{14}O$ samples at room temperature.....123
Figure 4.5. PXRD data corresponding to *ex-situ* experiments performed with a) $La_{10}S_{14}O$, and b) $Nd_{10}S_{14}O$; as well as *in-situ* studies in c) $La_{10}S_{14}O$, and d) $Sm_{10}S_{14}O$. 124
Figure 4.6. Differential scanning calorimetry, thermogravimetric analysis measurements, and PXRD performed for $La_{10}S_{14}O$ (a, b, c) and $Nd_{10}S_{14}O$ (d, e, f).....125

Supporting Figures

Figure S2.1. SEM Micrographs of a) Mo_6S_8, b) Mo_6Se_8 and c) Mo_6Te_8 along their corresponding PXRD diffractograms d) - f)..... 38
Figure S2.2. Changes in 2θ values for the diffraction peak in the (101) plane upon metal intercalation in CP sulfides **a)** and selenides **b)**. Metal intercalation in CP tellurides results in a triclinic distortion, in which the diffraction peak ~2θ = 12.5° corresponds to diffraction in the (101) and (010) for binary CP telluride and metal intercalated CP telluride, respectively **c)**..... 39
Figure S2.3. First derivative of the Mo K-edge..... 42

Figure S2.4. Mo L_3-edge XANES spectra corresponding to the binary and ternary $M_XMo_6T_8$ Chevrel phases demonstrating the effect of intercalation. Comparison between: **a)** Mo_6S_8 and $Cu_2Mo_6S_8$, **b)** Mo_6Se_8 and $Cu_2Mo_6Se_8$, **c)** Mo_6Te_8 and $NiMo_6Te_8$, and insets highlight the observed energy shifts with dotted lines through peak maxima..... 45
Figure S2.5. First derivative plots of the normalized Mo L_3-edge containing insets detailing the maxima for each binary Chevrel-phase. 46
Figure S2.6. Second derivative of the respective chalcogen K- (S and Se) and L-edge (Te) spectra in **a)** Mo_6S_8 and $Cu_2Mo_6S_8$, **b)** Mo_6Se_8 and $Cu_2Mo_6Se_8$ and **c)** Mo_6Te_8 and $NiMo_6Te_8$. **a)** the twin peaks located at 2470 which unify into a single signal upon copper intercalation and the sulfur atoms along the threefold rotation are fully coordinated. **b)** focuses on the slight Se K-edge shift which occurs upon metal intercalation..... 47
Figure S2.7. Molybdenum K-edge fits in k-space corresponding to a) Mo_6S_8, b) $Cu_2Mo_6S_8$, c) Mo_6Se_8, d) $Cu_2Mo_6S_8$, e) Mo_6Te_8, and f) $NiMo_6Te_8$. 54
Figure S2.8. Spectra of the S_1 and S_2 atoms in Mo_6S_8 and $Cu_2Mo_6S_8$; note that the starkly different pre-edge in S_1 and S_2 spectra (red and blue, respectively) in Mo_6S_8 become more similar in $Cu_2Mo_6S_8$ 56
Figure S2.9. Change in Bader charge with respect to the neutral atom in structures **1-4**, colored according to the element and coordination around the given atom. 58
Figure S2.10. Structural and charge transfer effects in the spectra of S_1 for structures **1-4**..... 59
Figure S2.11. Structural and charge transfer effects in the spectra of S_2 for structures **1-4.**.... 60
Figure S2.12. Projected density of states for the Non-Intercalated (a) and Intercalated (b) phases, aligned with reference to each's Fermi level - marked by a vertical line..... 62
Figure S3.1. Rietveld refinements for a) $La_{10}S_{14}O$, b) $Ce_{10}S_{14}O$, c) $Pr_{10}S_{14}O$, d) $Nd_{10}S_{14}O$, and e) $Sm_{10}S_{14}O$. Traces in black, blue, and violet represent the experimental data, difference, and fit. The remaining 2 traces represent the $Ln_{10}S_{14}O$ and secondary phases. 101
Figure S3.2. k-space FT-EXAFS fit for each oxychalcogenide. In each graph, the scatter plot, solid trace, and grey trace represent the data, fit result, and Hanning window used, respectively. 102
Figure S3.3. Representative coordination environments corresponding to each lanthanoid crystallographic site (enclosed within the light-green polyhedra). The closest second shell S^{2-} ion (r > 3.3 Å) is highlighted in Ln1 and Ln2 with an orange crosshair. 105
Figure S3.4. a) Raman spectra for all $Ln_{10}S_{14}O$, shown offset for clarity; b) Raman shift of selected peaks [marked with reference lines of matching color in a)] as a function of lanthanoid ion; c) lattice parameter changes (derived from the Rietveld refinements). 106

Figure S3.5. Scanning electron micrographs for a) $La_{10}S_{14}O$, b) $Ce_{10}S_{14}O$, c) $Pr_{10}S_{14}O$, d) $Nd_{10}S_{14}O$, and e) $Sm_{10}S_{14}O$.....107
Figure S3.6. L_3-edge XAS spectra of $Ln_{10}S_{14}O$, shown at their corresponding energies, a), and overlaid to highlight the white line region, b). 108
Figure S3.7. Differential absorption spectrum fitting for each lanthanoid oxysulfide. The centroid of the gaussian peaks, shown in the insets, corresponds to the reported E_g through this method. 110
Figure S3.8. Surface photovoltage spectra of a) $La_{10}S_{14}O$, b) $Pr_{10}S_{14}O$, c) $Nd_{10}S_{14}O$, and d) $Sm_{10}S_{14}O$, using a tungsten halogen lamp as illumination source (emission spectrum as dotted line in a). 111
Figure S3.9. Surface photovoltage spectroscopy of $Ce_{10}S_{14}O$ films drop casted onto FTO-coated glass support without thermal treatment. 112
Figure S3.10. a) Linear region of the surface photovoltage decay of $La_{10}S_{14}O$, $Pr_{10}S_{14}O$, $Nd_{10}S_{14}O$, and $Sm_{10}S_{14}O$. Solid black lines represent linear regression curves that best describe the normalized decay (in logarithmic scale) after light irradiation. The corresponding regular residuals are displayed in the following order: b) $La_{10}S_{14}O$, c) $Sm_{10}S_{14}O$, d) $Pr_{10}S_{14}O$, and d) $Nd_{10}S_{14}O$. 113
Figure S3.11. Mott-Schottky plots corresponding to $La_{10}S_{14}O$ (a, e), $Pr_{10}S_{14}O$ (b, f), $Nd_{10}S_{14}O$ (c, g), and $Sm_{10}S_{14}O$ (d, h), at 3 different frequencies (1, 3.4 and 7.8 kHz), measured in 0.1 M Na_2SO_4 solution. a) through d) were measured at pH ~ 11.5 and show a frequency dependence, while e) to h) show the effect of pH (at a constant frequency of 1 kHz). The positive slope signifies n-type semiconduction. However, the strong frequency dependence of the signal prevents reliable dopant density and flat-band potential determinations..... 114
Figure S4.1. Photograph of experimental setup for color space analysis. 133
Figure S4.2. Photograph of the custom in-situ cell for the heating PXRD experiments, showing the capillary tube containing the powdered sample, flanked by two metal coils that provide the heating, as well as gas-tight connections for the inert gas flow.....135

List of Tables

Table 2.1. Cluster anisotropy relationship to the cluster valence electron count (VEC). The anisotropy was calculated following ref. 21, as (R_{long} – R_{short}) x 100/R_{long}, where R depicts the interatomic distance between intracluster Mo atoms as obtained from Mo K edge EXAFS data (distances can be visualized in the blue polyhedron with each vertex representing a Mo atom). VEC was calculated according to ref. 21 27
Table 3.1. Band Gap Energies Obtained through Tauc and DASF Analysis and from SPS 80

Supporting Tables

Table S2.1. Scattering path distances obtained through Mo K-edge EXAFS data fitting for the sulfide, selenide and telluride CPs. Path labels correspond to those represented graphically in Figure 2.4. 43
Table S2.2. Peak maximum of the first derivative of the Mo L_3-edge. 46
Table S2.3. Fitting parameters for the Mo K-edge of Mo_6Se_8. S_o^2 is the amplitude reduction factor, E_o is the energy of the white line, σ^2 is the Debye-Waller factor, N is the scattering path degeneracy. The distances obtained from the EXAFS analysis are listed as Absorber-Scatterer pairs. 48
Table S2.4. Fitting parameters for the Mo K-edge of Mo_6S_8 49
Table S2.5. Fitting parameters for the Mo K-edge of Mo_6Te_8 50
Table S2.6. Fitting parameters for the Mo K-edge of $CuMo_6Se_8$ 52
Table S2.7. Fitting parameters for the Mo K-edge of $NiMo_6Te_8$ 53
Table S2.8. Calculated Bader charges (Lowdin charges in parentheses) on Mo-tetracoordinated (S_1) and Mo-tricoordinated (S_2) sulfur atoms and Mo atoms in Mo_6S_8 and $Cu_2Mo_6S_8$. 56
Table S3.1. Summarized Rietveld refinement parameters for all oxysulfides 100
Table S3.2. Ln L_3-edge EXAFS fitting parameters. 103
Table S3.3. Ln-S scattering distances and coordination derived from the fitting parameters detailed in Table S3.2 104
Table S 3.4. Linear regression fitting parameters from Direct and Indirect Tauc plot analyses. 109
Table S3.5. Photovoltage decay parameters for each lanthanoid oxysulfide. ΔCPD_{max} corresponds to the maximum photovoltage at the time the illumination was turned off. ΔCPD_f is the photovoltage signal at the end of the experiment, when 27 minutes have elapsed since the end

of the illumination time. % ΔCPD_{res} and % $\Delta CPD_{recovered}$ represent the residual and recovered photocurrent signal..... 112
Table S3.6. Photovoltage decay linear fitting parameters corresponding to equation 3..... 113
Table S4.1. CIE-Lab parameters as a function of temperature for all 5 lanthanoid oxysulfides during the cooling cycle under a flowing Ar atmosphere. (L is the lightness coordinate (L = 0 is black, L = 100 is white); a is the red-green-oriented coordinate (−a means greenness, +a means redness) b is the blue-yellow-oriented coordination (−b means blueness, +b means yellowness). 134
Table S4.2. Rietveld refinement parameters corresponding to the data represented in Figure 4.2. 136

1. Chapter 1

Introduction

Chalcogenide Materials Design for Energy Conversion

At the heart of materials chemistry, lies the goal of understanding the fundamental properties of matter so as to establish their nexus with a defined function, and thus attain its control. Solid state chemistry conforms an exciting area of inorganic research mainly due to the wide range of technological applications that materials exhibit, accompanied by the intrinsic complexity in their study. With the increasing deterioration of the global climate, ushered in by fossil-fueled industrialization, a call to action is set forth to develop technologies that will transform our current manufacturing and energy landscapes into sustainable ones, where materials chemistry plays a central role.

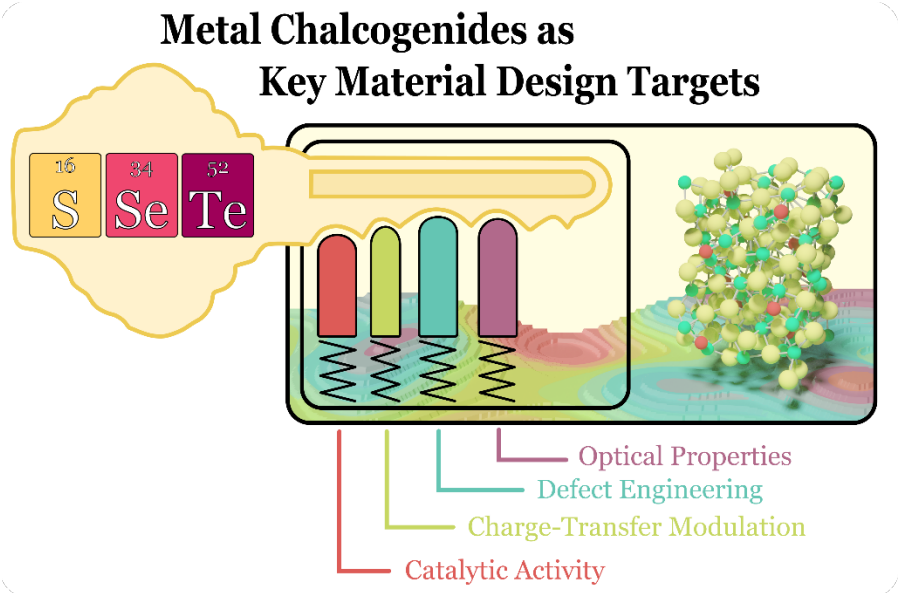


Figure 1.1. Diagram illustrating metal chalcogenides as a vessel that unlocks a multitude of beneficial properties in materials designed for energy conversion.

Among the biggest challenges of our time lies the realization of carbon neutral and negative emission technologies as ways to ameliorate the effects of global warming.[1] From a materials' perspective, this realization can be achieved by the design of light absorbers that can harvest intermittent sunlight, through the development of higher capacity batteries wherein this collected energy can be stored, and by the conception of selective catalyst materials that can directly or indirectly utilize renewably-sourced energy inputs to enable the conversion of molecules, whose products can act as energy vectors or replace petroleum-derived commodities. Metal chalcogenides represent a material space with apt characteristics to tackle these problems owing to the wide range of properties that sulfides, selenides, and tellurides encompass.[2] As light absorbers, chalcogenides offer great flexibility due to the consequential narrowing of the band gap that generally occurs as the chalcogen electronegativity decreases ($\chi_S > \chi_{Se} > \chi_{Te}$). As such, common wide band gap semiconductors like TiO_2 ($E_{g,\ rutile}$ = 3.0 eV) can be doped with sulfur resulting in smaller band gap energies (E_g < 2.9 eV) due to the rise in the valence band edge.[3] Hence, through chalcogen substitution,[4] combination of semiconductors,[5] and use of metal chalcogenides as sensitizers,[6] optimization of light absorption can be achieved. Moreover, if band edge positions have adequate energetic alignment, meaning a valence band maximum below the Gibbs free energy for an oxidation reaction, and/or a conduction band minimum above that of the Gibbs free energy for reduction reactions, generated charge carriers after light excitation can be utilized in catalytic transformations, like water splitting[7,8] and carbon dioxide reduction.[9] While some transition metal sulfides have shown hydrogen evolving activity rivaling that of precious metals like Pt,[10,11] significant challenges remain for the application of chalcogenides for oxidative reactions.[12] Nevertheless, the band structures of chalcogenides, and consequently their photophysical properties, can be extensively tuned through a multitude of methods, like the selective stacking of material layers in "2D" transition metal dichalcogenides,[13] or defect engineering.[11,14,15]

Beyond their light-absorption capabilities, metal chalcogenides have been extensively investigated as electrocatalysts, wherein their advantages rely on the diversity of chemical microenvironments and binding sites present, as opposed to the well-established monometallic transition metals. To facilitate chemical transformations, heterogeneous catalysts must offer surfaces that will interact with adsorbates with enough strength to enable sufficient residence time for the reaction to occur, but not too strong that would poison the catalyst and reach a product desorption limit; in other words, an ideal catalyst is one that facilitates a Sabatier optimum.[16] Thus, by providing diverse metallic and chalcogen-based binding sites, these materials can break the linear scaling relations observed between the adsorbate intermediates within a reaction mechanism and transition metals.[17]

Finally, the comparative softness of chalcogens, has been identified as critical in the application of chalcogenides as novel energy storage materials for anodes in sodium-ion batteries,[18,19] and applications as multivalent ion cathodes.[20,21] Chief to their functionality is the weaker interaction between intercalant ions (strongly ionic elements, like Na^+ and K^+, and in high oxidation states like Mg^{2+}, Zn^{2+}, and Al^{3+}) and the anions, allowing for higher ionic mobility and conductivity of the discharge products.

Underpinning all the applications that chalcogenide materials exhibit lies the composition–structure relationships that determine their vastly diverse morphologies, electronic properties and photophysics. Thus, a thorough understanding of the fundamental chemistry of metal chalcogenides is imperative to develop materials with new functionalities that address novel challenges.

Chevrel Phase Chalcogenides Composition-Function Relationship

Within the metal chalcogenide compositional space, transition metal dichalcogenides (TMDCs) have been the subject of extensive studies, due to their bi-dimensional nature similar to that of graphene, and ample interesting optoelectronic,[22] magnetic,[23,24] and electrocatalytic[25–27]

properties. Chevrel Phase (CP) chalcogenides ($M_xMo_6T_8$, where M = alkali, alkaline-earth, transition and post-transition metal, T = S, Se, Te; Figure 1.2) can be regarded as a dimensional expansion with a more extensive compositional landscape deriving in a more significant degree of tunability. These pseudo-molecular cluster frameworks have shown promise as superconductors,[28,29] active catalysts for the oxygen reduction reaction (ORR),[30,31] hydrogen evolution reaction (HER),[32,33] and carbon dioxide reduction reaction (CO2RR),[34,35] as well as multivalent cathode materials.[21,36–38]

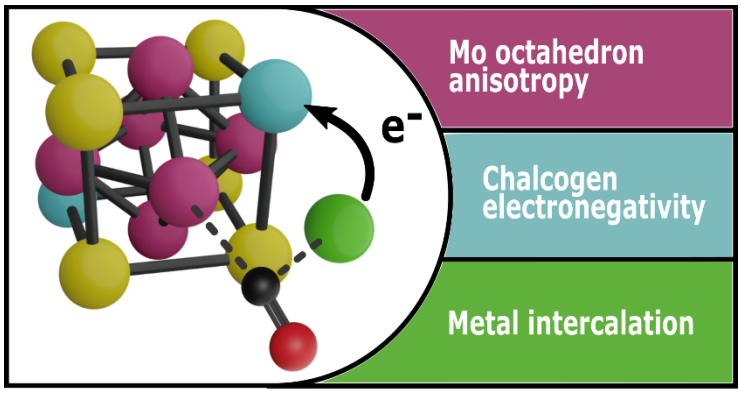


Figure 1.2. Scheme of a representative single CP cluster, showing the large compositional tunability and three common compositional handles that facilitate functional changes.

In the binary CPs, the central Mo_6 cluster is elongated along a C_3 rotational axis, which renders the anisotropic collection of atoms as trigonal antiprismatic in geometry. This is a direct consequence of the uneven electron density distribution in the surrounding face-capping chalcogens,[36,37] which regulates the degree of charge localization around each Mo center. As one of the key compositional "handles", the electronegativity of the chalcogen directly affects the Chevrel Phases' catalytic activity, as was shown for the electrocatalytic HER, wherein the reactivity decreases with the decrease in electronegativity.[33] In the extended structure, CP frameworks possess cavities and channels, in which cations can be hosted. These intercalant ions modify the bonding, crystal, and electronic structures of these chalcogenides. Generally, 1 and 2

equivalents of intercalant metal ions stabilize the clusters through charge transfer into their bonding orbitals, with the concomitant modification of electron density in the chalcogen cluster and geometric distortions in the contained Mo_6 trigonal antiprism (Figure 1.3).

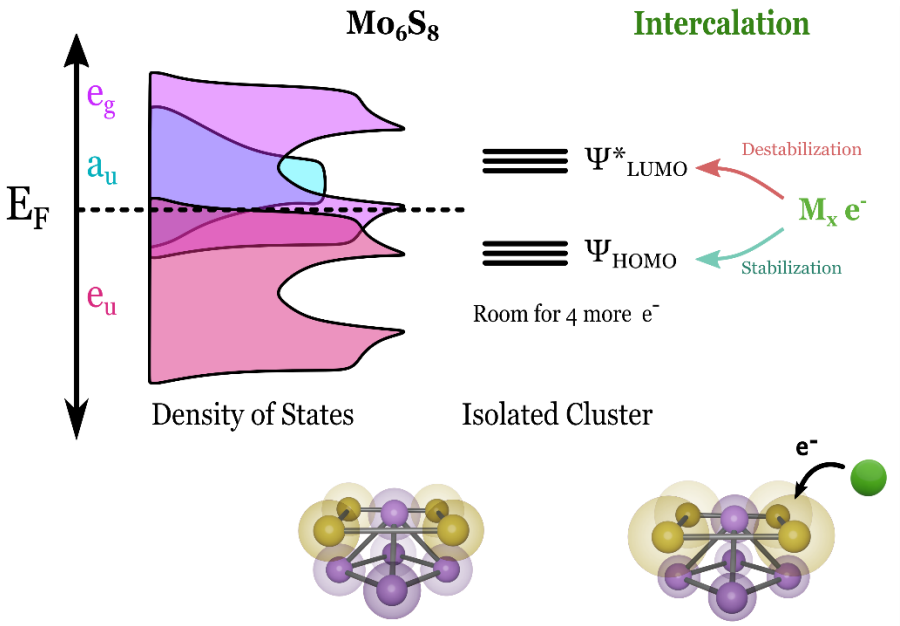


Figure 1.3. Schematic energy diagram showing the effect of intercalation in the Mo_6S_8 Chevrel Phase cluster electronic structure, based on Burdett et al.,[39] and Andersen et al..[40] The binary phases have 20 valence electrons, and their bonding orbitals can accommodate 4 additional electrons. A greater charge transfer from the intercalant ions into the cluster leads to destabilization of the cluster due to population of orbitals of antibonding character.

Such modifications can indirectly affect the catalytic properties of Chevrel Phases, in a denominated "ligand effect". However, the presence and identity of metal intercalants can also directly alter the interfacial reactivity towards the conversion of small molecules, through a geometric or "ensemble effect". As shown by Liu et al., the more electropositive K^+, facilitates the electrostatic stabilization of transition states toward the synthesis of CH_3OH. Conversely, the comparatively electronegative Cu decreases this catalytic activity, favoring the production of formate.[35] The suitability of Chevrel Phases as multivalent cathode materials is also a manifestation of their metallic electronic structure capable of shielding the charge of mono-, di-

and trivalent cations, facilitating their diffusion through the ion channels. The chalcogenide anions' lower electronegativity and higher polarizability play a central role due to their weaker ionic interaction with the intercalant ion, thus improving ion mobility compared to oxides.[21,41] Chapter 2 of this work will delve into the evolution of structural and electronic properties brought upon by the intercalation of late transition metals into the Chevrel Phase frameworks, expanding the study to the whole series of chalcogenides.

Optical Thermometry in Lanthanoids

Beyond energy conversion, the development of new materials has also revolutionized the area of physical and chemical sensors. Specifically, the accurate measurement of temperature, a key parameter in all natural and synthetic systems, is a field of research in constant evolution due to novel market demands. Among the many physical principles used in temperature sensors, optical thermometry, while in its early stages of metrological assessment, offers multiple advantages over the more common types of sensors; namely, resistance temperature detectors (RTD), negative temperature coefficient (NTC) thermistors, and thermocouples.[42] Primarily, the optical measurement of temperature is a non-contact method, thus allowing its application in more complex and harsh environments, over wide temperature ranges. Luminescence is the most used fundamental property of matter for these kinds of sensors, which rely on the emissive response of the material to an initial photon irradiation. From the decay time or energy position, a temperature readout can be obtained from the luminescence intensity ratio (LIR) between two emission bands.[43] Owing to their internal 4f electrons, largely unperturbed by their chemical environment, resulting in pure emission bands which span across the entire spectrum, lanthanoids are ubiquitously present in luminescent thermometers.[44–47] Generally existing as dopants in oxides and fluorides, most luminescence-based thermometric applications require the use of detectors in the infrared region. While there are examples in which materials demonstrate visible thermochromism, in them, the lanthanoid ions seem to only play a spectator role.[48–50]

In this body of work, we will investigate the composition-function relationships in a series of visible-light semiconducting lanthanoid oxysulfides ($Ln_{10}S_{14}O$, Ln = La, Ce, Pr, Nd, and Sm). Chapter 3 will present the thorough characterization of their local coordination, bulk and surface electronic structure, as well as their optical properties. Finally, in Chapter 4, their high-temperature reversible thermochromism will be reported, and in-situ characterization studies will seek to unravel the origin of this unusual property hardly ever identified in non-transition-metal-containing chalcogenides, which could open the study of high-temperature colorimetry-based thermometric sensors for complex environments.

X-Ray Absorption Spectroscopy

Throughout this work, we extensively use X-ray absorption spectroscopic (XAS) techniques based on synchrotron radiation. The uniqueness of this spectroscopy lies in the element specificity derived from the distinct energy differences of the core electronic levels among elements of the periodic table. A typical X-ray absorption spectrum encodes a plethora of information in its three regions, as seen below in Figure 1. 2b. The X-ray near-edge structure (XANES) consisting of the pre-edge, which comprises quadrupole allowed transitions, $\Delta l \pm 2$ (e.g., 1s → 3d, in K-edges; Figure 1.4 a), and the edge, where the dipole allowed electronic transitions ($\Delta l \pm 1$) between the core levels and the high-energy bound states as well as the threshold to photoionization exist.[51] The XANES region can provide valuable information about the ligand field and degree of centrosymmetry, spin state, covalency and orbital hybridization. At high energies, the oscillations present in the extended X-ray absorption fine structure (EXAFS) region are derived from the constructive and destructive interference that occurs from the emitted photoelectrons with those scattered from the electron density of neighboring atoms. As a result, the analysis of this spectral section provides geometric information on the local structure surrounding the absorbing element, and hence, there is no need for long range order, and this technique can be applied to amorphous materials as well as crystalline, liquid, and gaseous systems.

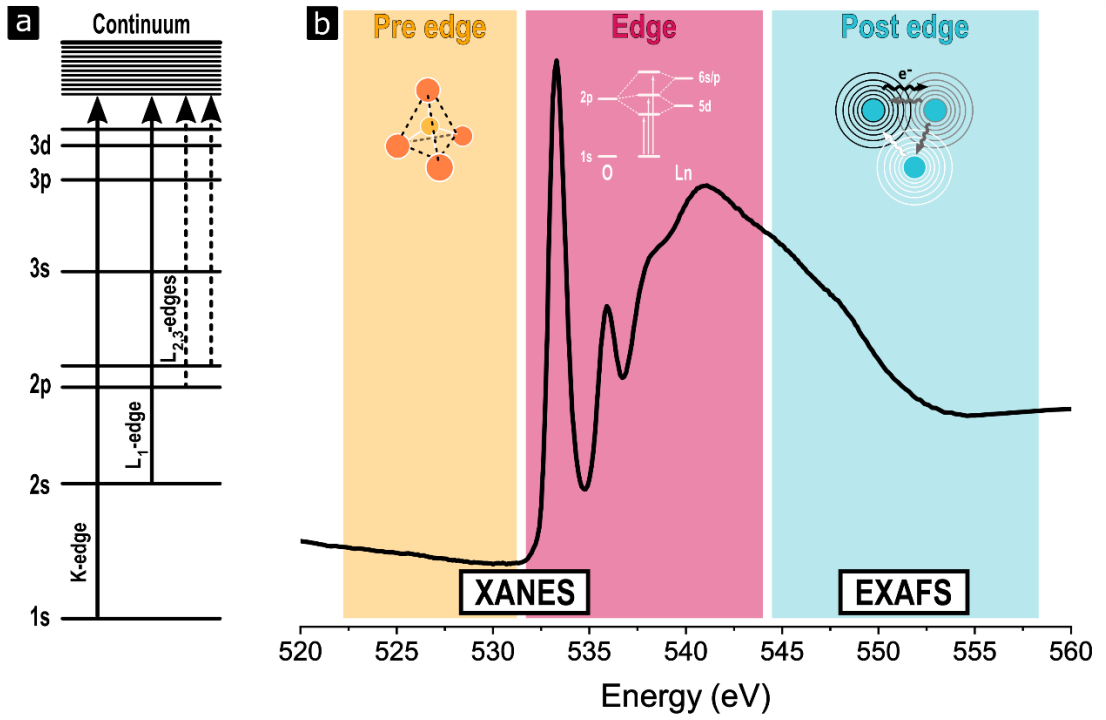


Figure 1.4. Example of an X-ray spectrum with its characteristic 3 regions: Pre-edge, Edge and Post-edge in increasing energy. Data corresponds to the O K-edge spectrum of $La_{10}S_{14}O$, in which the edge is characterized by multiple absorption bands associated with the crystal field splitting of the La^{3+} 5d orbitals and 6p orbitals, both hybridized with the O 2p states.[52]

Analysis of the XANES region can be accomplished experimentally by comparison with standards, in which the electronic properties, ligand field and bonding environment are well understood. Insight can also be derived from the study of trends in a series of similar systems. However, the most understanding is gained through the theoretical simulation of spectra, which can be performed through different means.[53] In this work, we have used a density functional theory (DFT) constrained-occupancy delta-self-consistent (ΔSCF) method coupled with a many-body explicit calculation known as the excited-electron and core-hole (XCH) method.[54,55] In essence, this computation of the absorbance σ(ω) is rooted in Fermi's golden rule:

$$\sigma(\omega) \propto \omega \sum_f \left|\langle \Psi_f | \boldsymbol{\epsilon} \cdot \boldsymbol{R} | \Psi_i \rangle\right|^2 \delta(E_f - E_i - \hbar\omega) \qquad (1.1)$$

where: $\boldsymbol{\epsilon}$ is the photon polarization, $\boldsymbol{R}$ is the many-body position operator, $|\Psi_i\rangle$ and $\langle\Psi_f|$ represents the initial (ground) and final state (excited core-hole) eigenstates of the system, with energies E_i and E_f. This sum, which contains all possible transitions from the core to excited states accounting for the multiple electronic interactions, is performed on supercells of ~1 nm^3 by using appropriate pseudopotentials that accurately describe the ground state and explicitly contain a core-hole for the final excited states (Figure 1.5).

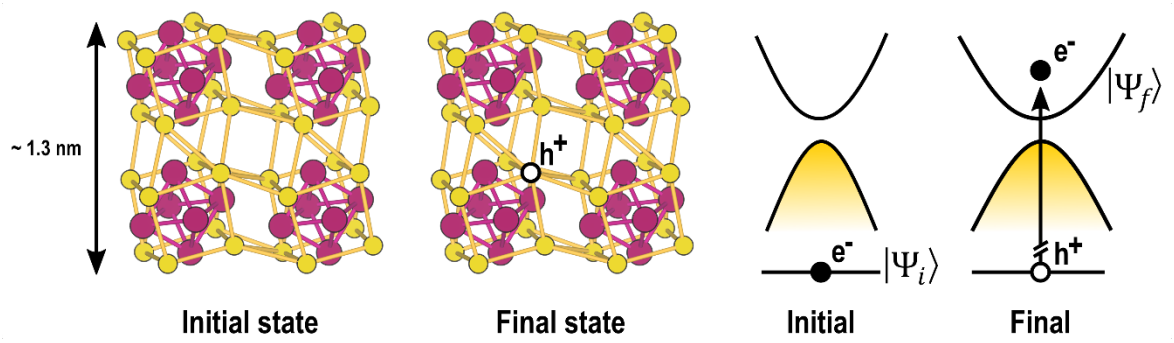


Figure 1.5. Graphical representation of the one-body core-hole approach calculation based on a ΔSCF method. The crystal structures on the left correspond to a 2x2x2 Mo_6S_8 supercell viewed from the *a*-axis.

Valuable structural information is embedded in the EXAFS portion of the spectrum. In comparison with XANES analysis, simulating and fitting EXAFS data is a much more mature field with multiple software packages that facilitate accessibility to this technique (e.g., Larch, and Athena and Artemis[56]). However, a good understanding of the material system is required to extract meaningful information. From single scattering plane wave theory, the following EXAFS equation can be obtained:

$$\chi(k) = \sum_i \underbrace{\frac{N_i A_i(k,R_i)}{kR_i^2} x e^{-2\sigma_i^2 k^2} e^{\frac{-2R_i}{\lambda(k,R_i)}}}_{\text{Amplitude}} \underbrace{\sin[2kR_i +}_{\text{Frequency}} \underbrace{\alpha_i(k,R_i)]}_{\text{Phase}} \quad (1.2)$$

where N is the number of neighboring atoms, R is the distance between absorber-scatterer, σ is the mean square deviation in R, λ is the mean free path for inelastic scattering for the photoelectron, A is the amplitude function, and α is the phase function. From the appropriate parameterization of the equation, information about the coordination number, local structure and identity of the scattering atoms can be obtained.

In Chapter 2, we explore the structural and charge transfer effects of the intercalation of transition metals into the Chevrel Phase sulfide, selenide, and telluride frameworks through Mo and ligand K- and L-edges. Later, in Chapter 3, we study the structure and local coordination surrounding trivalent lanthanoid cations by way of the lanthanoid L_3-edges.

Surface Photovoltage Spectroscopy

A critical aspect in the study of the electronic properties of semiconductors is the nature of the majority carriers as well as the charge recombination dynamics. Surface photovoltage spectroscopy (SPS) is based on the surface photovoltaic effect, that is, the change of the electrochemical potential in the space-charge region upon illumination. One way to measure this phenomenon is through the assembly of a parallel plate capacitor between a gold Kelvin probe and the material to be studied deposited onto a conductive substrate, as shown in Figure 1.6. In this configuration, the measurement of the surface photovoltage is performed indirectly by the determination of the difference in work function between the materials in the capacitor, known as contact potential difference (ΔCPD). As the Au Kelvin probe vibrates in close proximity to the sample surface, a steady-state A.C. current develops in the capacitor formed. The ΔCPD arises from the required D.C. bias necessary to compensate for the A.C. current.[57]

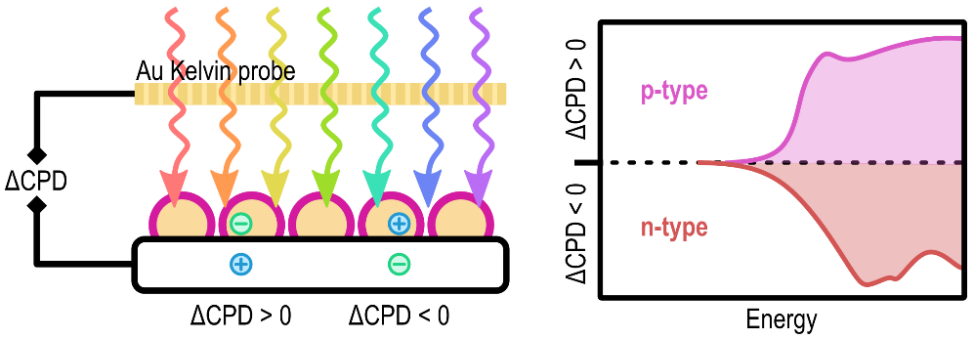


Figure 1.6. Schematic diagram of the experimental setup used in surface photovoltage spectroscopy measurements, and the contact potential difference response as a function of incident photon energy obtained for p- and n-type semiconductors, in which the majority carriers are holes and electrons, respectively.

Given its inherent insensitivity to reflection and scattering, this technique is uniquely suited for the study of polycrystalline materials. Furthermore, SPS is highly sensitive to sub-band gap effects as well as carrier trapping at surface defects,[58] which are widely present in chalcogenides. In Chapter 3, we use this spectroscopy to carry out an investigation of the charge separation phenomena occurring at the surface of lanthanoid oxysulfides ($Ln_{10}S_{14}O$), where we identify the identity of the majority carriers and analyze the striking long lifetimes after charge separation.

References

(1) Hill, C. M.; Mendoza-Cortes, J. L.; Velázquez, J. M.; Whittaker-Brooks, L. Multi-Dimensional Designer Catalysts for Negative Emissions Science (NES): Bridging the Gap between Synthesis, Simulations, and Analysis. *iScience*, 2022, *25*, 1–13.

(2) Perryman, J. T.; Velazquez, J. M. Design Principles for Multinary Metal Chalcogenides: Toward Programmable Reactivity in Energy Conversion. *Chemistry of Materials*, 2021.

(3) Umebayashi, T.; Yamaki, T.; Yamamoto, S.; Miyashita, A.; Tanaka, S.; Sumita, T.; Asai, K. Sulfur-Doping of Rutile-Titanium Dioxide by Ion Implantation: Photocurrent

Spectroscopy and First-Principles Band Calculation Studies. *Journal of Applied Physics*, 2003, *93*, 5156–5160.

(4) DeAngelis, A. D.; Horsley, K.; Gaillard, N. Wide Band Gap CuGa(S,Se) $_2$ Thin Films on Transparent Conductive Fluorinated Tin Oxide Substrates as Photocathode Candidates for Tandem Water Splitting Devices. *The Journal of Physical Chemistry C*, 2018, acs.jpcc.8b02915.

(5) Gur, I.; Fromer, N. A.; Geier, M. L.; Alivisatos, A. P. Air-Stable All-Inorganic Nanocrystal Solar Cells Processed from Solution. *Science*, 2005, *310*, 462–466.

(6) Evangelista, R. M.; Makuta, S.; Yonezu, S.; Andrews, J.; Tachibana, Y. Semiconductor Quantum Dot Sensitized Solar Cells Based on Ferricyanide/Ferrocyanide Redox Electrolyte Reaching an Open Circuit Photovoltage of 0.8 V. *ACS Applied Materials and Interfaces*, 2016, *8*, 13957–13965.

(7) Walter, M. G.; Warren, E. L.; McKone, J. R.; Boettcher, S. W.; Mi, Q.; Santori, E. A.; Lewis, N. S. Solar Water Splitting Cells. *Chemical Reviews*, 2010.

(8) Yin, J.; Jin, J.; Lin, H.; Yin, Z.; Li, J.; Lu, M.; Guo, L.; Xi, P.; Tang, Y.; Yan, C. H. Optimized Metal Chalcogenides for Boosting Water Splitting. *Advanced Science*. 2020.

(9) Singh, A. K.; Montoya, J. H.; Gregoire, J. M.; Persson, K. A. Robust and Synthesizable Photocatalysts for CO2 Reduction: A Data-Driven Materials Discovery. *Nature Communications*, 2019, *10*.

(10) Li, H.; Tsai, C.; Koh, A. L.; Cai, L.; Contryman, A. W.; Fragapane, A. H.; Zhao, J.; Han, H. S.; Manoharan, H. C.; Abild-Pedersen, F.; Nørskov, J. K.; Zheng, X. Activating and Optimizing MoS2 Basal Planes for Hydrogen Evolution through the Formation of Strained Sulphur Vacancies (Nature Materials (2016) 15 (48-53)). *Nature Materials*. Nature Publishing Group 2016, p 364.

(11) Ye, G.; Gong, Y.; Lin, J.; Li, B.; He, Y.; Pantelides, S. T.; Zhou, W.; Vajtai, R.; Ajayan, P. M. Defects Engineered Monolayer MoS2 for Improved Hydrogen Evolution Reaction. *Nano Letters*, 2016, *16*, 1097–1103.

(12) Su, J.; Wei, Y.; Vayssieres, L. Stability and Performance of Sulfide-, Nitride-, and Phosphide-Based Electrodes for Photocatalytic Solar Water Splitting. *Journal of Physical Chemistry Letters*, 2017, *8*, 5228–5238.

(13) Zhuang, G.; Yan, J.; Wen, Y.; Zhuang, Z.; Yu, Y. Two-Dimensional Transition Metal Oxides and Chalcogenides for Advanced Photocatalysis: Progress, Challenges, and Opportunities. *Solar RRL*, 2021, *5*, 1–50.

(14) Shin, D.; Saparov, B.; Mitzi, D. B. Defect Engineering in Multinary Earth-Abundant Chalcogenide Photovoltaic Materials. *Advanced Energy Materials*, 2017, *7*.

(15) He, Z.; Zhao, R.; Chen, X.; Chen, H.; Zhu, Y.; Su, H.; Huang, S.; Xue, J.; Dai, J.; Cheng, S.; Liu, M.; Wang, X.; Chen, Y. Defect Engineering in Single-Layer MoS 2 Using Heavy Ion Irradiation. *ACS Applied Materials and Interfaces*, 2018, *10*, 42524–42533.

(16) Medford, A. J.; Vojvodic, A.; Hummelshøj, J. S.; Voss, J.; Abild-Pedersen, F.; Studt, F.; Bligaard, T.; Nilsson, A.; Nørskov, J. K. From the Sabatier Principle to a Predictive Theory of Transition-Metal Heterogeneous Catalysis. *Journal of Catalysis*, 2015, *328*, 36–42.

(17) Hong, X.; Chan, K.; Tsai, C.; Nørskov, J. K. How Doped MoS2 Breaks Transition-Metal Scaling Relations for CO2 Electrochemical Reduction. *ACS Catalysis*, 2016, *6*, 4428–4437.

(18) Dai, S.; Wang, L.; Cao, M.; Zhong, Z.; Shen, Y.; Wang, M. Design Strategies in Metal Chalcogenides Anode Materials for High-Performance Sodium-Ion Battery. *Materials Today Energy*, 2019, *12*, 114–128.

(19) Tan, H.; Feng, Y.; Rui, X.; Yu, Y.; Huang, S. Metal Chalcogenides: Paving the Way for High-Performance Sodium/Potassium-Ion Batteries. *Small Methods*, 2020, *4*, 1–46.

(20) Mitelman, A.; Levi, M. D.; Lancry, E.; Levi, E.; Aurbach, D. New Cathode Materials for Rechargeable Mg Batteries: Fast Mg Ion Transport and Reversible Copper Extrusion in CuyMo6S8 Compounds. *Chemical Communications*, 2007, 4212–4214.

(21) Geng, L.; Lv, G.; Xing, X.; Guo, J. Reversible Electrochemical Intercalation of Aluminum in Mo6S8. *Chemistry of Materials*, 2015, *27*, 4926–4929.

(22) Wang, Q. H.; Kalantar-Zadeh, K.; Kis, A.; Coleman, J. N.; Strano, M. S. Electronics and Optoelectronics of Two-Dimensional Transition Metal Dichalcogenides. *Nature Nanotechnology*, 2012, *7*, 699–712.

(23) Tu, Z.; Wu, M. 2D Diluted Multiferroic Semiconductors upon Intercalation. *Advanced Electronic Materials*, 2019, *5*, 1–7.

(24) Guguchia, Z.; Kerelsky, A.; Edelberg, D.; Banerjee, S.; Von Rohr, F.; Scullion, D.; Augustin, M.; Scully, M.; Rhodes, D. A.; Shermadini, Z.; Luetkens, H.; Shengelaya, A.; Baines, C.; Morenzoni, E.; Amato, A.; Hone, J. C.; Khasanov, R.; Billinge, S. J. L.; Santos, E.; Pasupathy, A. N.; Uemura, Y. J. Magnetism in Semiconducting Molybdenum Dichalcogenides. *Science Advances*, 2018, *4*, 1–9.

(25) Parija, A.; Choi, Y. H.; Liu, Z.; Andrews, J. L.; De Jesus, L. R.; Fakra, S. C.; Al-Hashimi, M.; Batteas, J. D.; Prendergast, D.; Banerjee, S. Mapping Catalytically Relevant Edge Electronic States of MoS2. *ACS Central Science*, 2018, *4*, 493–503.

(26) Francis, S. A.; Velazquez, J. M.; Ferrer, I. M.; Torelli, D. A.; Guevarra, D.; McDowell, M. T.; Sun, K.; Zhou, X.; Saadi, F. H.; John, J.; Richter, M. H.; Hyler, F. P.; Papadantonakis, K. M.; Brunschwig, B. S.; Lewis, N. S. Reduction of Aqueous CO2 to 1-Propanol at MoS2 Electrodes. *Chemistry of Materials*, 2018, *30*, 4902–4908.

(27) Wiensch, J. D.; John, J.; Velazquez, J. M.; Torelli, D. A.; Pieterick, A. P.; McDowell, M. T.; Sun, K.; Zhao, X.; Brunschwig, B. S.; Lewis, N. S. Comparative Study in Acidic and Alkaline Media of the Effects of PH and Crystallinity on the Hydrogen-Evolution Reaction on MoS2 and MoSe2. *ACS Energy Letters*, 2017, *2*, 2234–2238.

(28) Fischer, Ø. Chevrel Phases: Superconducting and Normal State Properties. *Applied Physics*, 1978, *16*, 1–28.

(29) Delk, F. S.; Sienko, M. J. Relationship between Superconductivity, Magnetic Susceptibility, and Crystal Structure in the Pseudobinary System Lead Molybdenum Sulfide-Lead Molybdenum Selenide (PbMo6S8-PbMo6Se8). *Inorganic Chemistry*, 1980, *19*, 1352–1356.

(30) Xia, F.; Li, B.; Liu, Y.; Liu, Y.; Gao, S.; Lu, K.; Kaelin, J.; Wang, R.; Marks, T. J.; Cheng, Y. Carbon Free and Noble Metal Free Ni2Mo6S8 Electrocatalyst for Selective Electrosynthesis of H2O2. *Advanced Functional Materials*, 2021, *31*.

(31) Alonso-Vante, N.; Malakhov, I. V.; Nikitenko, S. G.; Savinova, E. R.; Kochubey, D. I. The Structure Analysis of the Active Centers of Ru-Containing Electrocatalysts for the Oxygen Reduction. An in Situ EXAFS Study. *Electrochimica Acta*, 2002, *47*, 3807–3814.

(32) Naik, K. M.; Sampath, S. Cubic Mo6S8-Efficient Electrocatalyst Towards Hydrogen Evolution Over Wide PH Range. *Electrochimica Acta*, 2017, *252*, 408–415.

(33) Ortiz-Rodríguez, J. C.; Singstock, N. R.; Perryman, J. T.; Hyler, F. P.; Jones, S. J.; Holder, A. M.; Musgrave, C. B.; Velázquez, J. M. Stabilizing Hydrogen Adsorption through Theory-Guided Chalcogen Substitution in Chevrel-Phase Mo6X8(X=S, Se, Te) Electrocatalysts. *ACS Applied Materials and Interfaces*, 2020, *12*, 35995–36003.

(34) Perryman, J. T.; Ortiz-Rodríguez, J. C.; Jude, J. W.; Hyler, F. P.; Davis, R. C.; Mehta, A.; Kulkarni, A. R.; Patridge, C. J.; Velázquez, J. M. Metal-Promoted Mo6S8 Clusters: A

Platform for Probing Ensemble Effects on the Electrochemical Conversion of CO2 and CO to Methanol. *Materials Horizons*, 2020, *7*, 193–202.

(35) Liu, C.; Liu, P. Mechanistic Study of Methanol Synthesis from CO2 and H2 on a Modified Model Mo6S8 Cluster. *ACS Catalysis*, 2015, *5*, 1004–1012.

(36) Wan, L. F.; Wright, J.; Perdue, B. R.; Fister, T. T.; Kim, S.; Apblett, C. A.; Prendergast, D. Revealing Electronic Structure Changes in Chevrel Phase Cathodes upon Mg Insertion Using X-Ray Absorption Spectroscopy. *Physical Chemistry Chemical Physics*, 2016, *18*, 17326–17329.

(37) Muthuraj, D.; Mitra, S. Reversible Mg Insertion into Chevrel Phase Mo6S8 Cathode: Preparation, Electrochemistry and X-Ray Photoelectron Spectroscopy Study. *Materials Research Bulletin*, 2018, *101*, 167–174.

(38) Agiorgousis, M. L.; Sun, Y.-Y.; West, D. J.; Zhang, S. Intercalated Chevrel Phase Mo6S8 as a Janus Material for Energy Generation and Storage. *ACS Applied Energy Materials*, 2018, acsaem.7b00092.

(39) Burdett, J. K.; Lin, J. H. Structures of Chevrel Phases. *Inorganic Chemistry*, 1982, *21*, 5–10.

(40) Andersen, O. K.; Klose, W.; Nohl, H. Electronic Structure of Chevrel-Phase High-Critical-Field Superconductors. *Physical Review B*, 1978, *17*, 1209–1237.

(41) Thöle, F.; Wan, L. F.; Prendergast, D. Re-Examining the Chevrel Phase Mo6S8 Cathode for Mg Intercalation from an Electronic Structure Perspective. *Physical Chemistry Chemical Physics*, 2015, *17*, 22548–22551.

(42) Dedyulin, S.; Ahmed, Z.; Machin, G. Emerging Technologies in the Field of Thermometry. *Measurement Science and Technology*, 2022, *33*.

(43) Dramićanin, M. D. Trends in Luminescence Thermometry. *Journal of Applied Physics*, 2020, *128*.

(44) Bünzli, J. C. G. Benefiting from the Unique Properties of Lanthanide Ions. *Accounts of Chemical Research*, 2006, *39*, 53–61.

(45) Jana, S.; Mondal, A.; Manam, J.; Das, S. Pr3+ Doped BaNb2O6 Reddish Orange Emitting Phosphor for Solid State Lighting and Optical Thermometry Applications. *Journal of Alloys and Compounds*, 2020, *821*, 153342.

(46) Runowski, M.; Wozny, P.; Stopikowska, N.; Martín, I. R.; Lavín, V.; Lis, S. Luminescent Nanothermometer Operating at Very High Temperature-Sensing up to 1000 K with Upconverting Nanoparticles (Yb3+/Tm3+). *ACS Applied Materials and Interfaces*, 2020, *12*, 43933–43941.

(47) Stich, M. I. J.; Nagl, S.; Wolfbeis, O. S.; Henne, U.; Schaeferling, M. A Dual Luminescent Sensor Material for Simultaneous Imaging of Pressure and Temperature on Surfaces. *Advanced Functional Materials*, 2008, *18*, 1399–1406.

(48) Liu, H.; Qi, H.; Yuan, L.; Wang, B.; Hou, C.; Feng, S. Design Principles for 3d Electron Transfer in a Ga-Based Garnet to Enable High-Performance Reversible Thermochromic Material Color Maps. *Chemistry of Materials*, 2019, *31*, 1048–1056.

(49) Liu, H.; Yuan, L.; Wang, S.; Fang, H.; Zhang, Y.; Hou, C.; Feng, S. Structure, Optical Spectroscopy Properties and Thermochromism of Sm3Fe5O12 Garnets. *Journal of Materials Chemistry C*, 2016, *4*, 10529–10537.

(50) Liu, H.; Yuan, L.; Qi, H.; Wang, S.; Du, Y.; Zhang, Y.; Hou, C.; Feng, S. In-Situ Optical and Structural Insight of Reversible Thermochromic Materials of Sm3-XBixFe5O12 (X= 0, 0.1, 0.3, 0.5). *Dyes and Pigments*, 2017, *145*, 418–426.

(51) Baker, M. L.; Mara, M. W.; Yan, J. J.; Hodgson, K. O.; Hedman, B.; Solomon, E. I. K- and L-Edge X-Ray Absorption Spectroscopy (XAS) and Resonant Inelastic X-Ray Scattering (RIXS) Determination of Differential Orbital Covalency (DOC) of Transition Metal Sites. *Coordination Chemistry Reviews*, 2017, *345*, 182–208.

(52) Altman, A. B.; Pacold, J. I.; Wang, J.; Lukens, W. W.; Minasian, S. G. Evidence for 5d-σ and 5d-π Covalency in Lanthanide Sesquioxides from Oxygen K-Edge X-Ray Absorption Spectroscopy. *Dalton Transactions*, 2016, *45*, 9948–9961.

(53) De Groot, F.; Vankó, G.; Glatzel, P. The 1s X-Ray Absorption Pre-Edge Structures in Transition Metal Oxides. *Journal of Physics Condensed Matter*, 2009, *21*.

(54) Liang, Y.; Vinson, J.; Pemmaraju, S.; Drisdell, W. S.; Shirley, E. L.; Prendergast, D. Accurate X-Ray Spectral Predictions: An Advanced Self-Consistent-Field Approach Inspired by Many-Body Perturbation Theory. *Physical Review Letters*, 2017, *118*, 1–7.

(55) Liang, Y.; Prendergast, D. Quantum Many-Body Effects in x-Ray Spectra Efficiently Computed Using a Basic Graph Algorithm. *Physical Review B*, 2018, *97*, 1–25.

(56) Ravel, B.; Newville, M. ATHENA, ARTEMIS, HEPHAESTUS: Data Analysis for X-Ray Absorption Spectroscopy Using IFEFFIT. *Journal of Synchrotron Radiation*, 2005, *12*, 537–541.

(57) Kronik, L.; Shapira, Y. Surface Photovoltage Spectroscopy of Semiconductor Structures: At the Crossroads of Physics, Chemistry and Electrical Engineering. *Surface and Interface Analysis*, 2001, *31*, 954–965.

(58) Melo, M. A.; Osterloh, F. E. Defect States Control Effective Band Gap and Photochemistry of Graphene Quantum Dots. *ACS Applied Materials and Interfaces*, 2018, *10*, 27195–27204.

2. Chapter 2

X-ray Absorption Spectroscopy Insights on the Structure Anisotropy and Charge Transfer in Chevrel Phase Chalcogenides

Abstract

The electronic structure and local coordination of binary (Mo_6T_8) and ternary Chevrel Phases ($M_xMo_6T_8$) are investigated for a range of metal intercalant and chalcogen compositions. We evaluate differences in the Mo L_3-edge and K-edge X-ray absorption near edge structure across the suite of chalcogenides$M_xMo_6T_8$ (M = Cu, Ni, x = 1–2, T = S, Se, Te), quantifying the effect of compositional and structural modification on electronic structure. Furthermore, we highlight the expansion, contraction, and anisotropy of Mo_6 clusters within these Chevrel Phase frameworks through extended X-ray absorption fine structure analysis. Our results show that metal-to-cluster charge transfer upon intercalation is dominated by the chalcogen acceptors, evidenced by significant changes in their respective X-ray absorption spectra in comparison to relatively unaffected Mo cations. These results explain the effects of metal intercalation on the electronic and local structure of Chevrel Phases across various chalcogen compositions, and aid in rationalizing electron distribution within the structure.

Introduction

Since their first synthesis in 1971,[1] Chevrel Phases (CPs), $M_xMo_6T_8$ (M = metal; T = S, Se, Te), have demonstrated remarkable properties. Most notably, these properties lend themselves toward the use of CPs as high-temperature superconductors,[2,3] thermoelectrics,[4] multivalent cathodematerials,[5–8] and catalysts.[9–11] Indeed, its unique pseudomolecular structure endows CPs with a high degree of tunability of its electronic structure, including its valence and conduction band positions, band gaps, and orbital interactions with participating species in surface reactions.

Hence, the electronic properties of these materials are sensitive to the identity and stoichiometry of the metal ion intercalant, M, as well as by the chalcogen identity, T.[12] However, while numerous studies have been performed by our group[10,11,13–15] and by the larger community exploring the electronic structure of sulfide binary and ternary CPs, comparatively less is known about their selenide and telluride analogs.[4,13,15–17]

The structure of CPs can be described as a network of cubic chalcogen cages that enclose a distorted octahedron of Mo atoms. As a result of their arrangement, the cage and octahedron that form each $M_xMo_6T_8$ cluster share a 3-fold rotational axis, rendering two chalcogen ions (T_2) of each cluster along this axis of symmetry as chemically distinguishable from the remaining six chalcogen ions due to their unique coordination environment (as seen in Figure 2.1).[18]

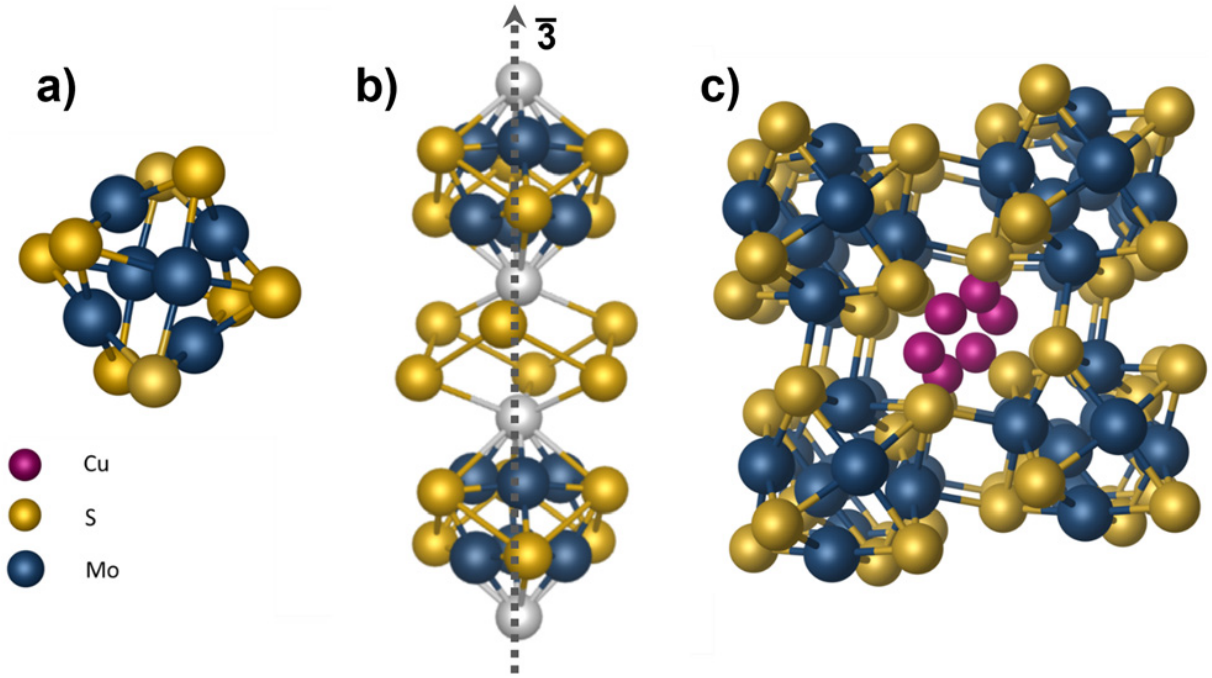


Figure 2.1. Crystal structure of the rhombohedral (R-3) CPs studied herein ($Cu_2Mo_6T_8$ T = S, Se) depicting (a) an individual Mo_6T_8 cluster where the Mo atoms are represented in blue, and chalcogen atoms in gold, (b)adjacent Mo_6T_8 clusters detailing a 3-fold rotational axis where cluster-linking undercoordinated chalcogens (T_2) are represented in white, and an intercluster cavity into which metals can be intercalated, and (c) the $M_xMo_6T_8$ framework where intercalant metal atom sites are represented by magenta.

In the extended CP structure, clusters are linked together by their chalcogen cages, which enable strong intercluster Mo–T and T–T interactions to yield a framework with voids that can host a range of metal cation stoichiometries.

In the binary CPs, the Mo_6 cluster is better described as a trigonal antiprism, which decreases in anisotropy as intercalant ions are inserted into the frameworks. This symmetry change has been previously explained as being the result of the electron density distribution within the Mo_6 octahedra (electronic factor)[19] as well as intercluster chalcogen repulsion that affects intracluster Mo–Mo bonding (geometric factor).[20] These electronic and geometric factor hypotheses agree with the observed contraction of the Mo_6 cluster upon intercalation of metal ions, which derives from the filling of Mo–Mo bonding states and the weakening of intercluster Mo–Mo and Mo–T bonds, respectively. A more detailed bond valence study that explored the nature of Mo_6-cluster anisotropy and its evolution upon cation insertion identified non-uniformity in anion charge distribution as the primary driver of intrinsic electronic instability of the binary sulfide phases, as well as the decrease in nonuniformity upon intercalation of small ions.[21] To provide additional insight regarding the aforementioned electronic structure and bonding formalisms for CPs, we present a detailed X-ray spectroscopic analysis of the interplay between electronic structure and local Mo–Mo and Mo–T coordination across an entire suite of binary and ternary CP chalcogenides.

X-ray absorption spectroscopy (XAS) is a uniquely well-suited technique for the study of these complex multinary systems, owing to its high elemental specificity and ability to provide valuable structural and electronic information. By means of X-ray absorption near-edge structure (XANES) analysis, exciton transitions are observed that can reveal critical information regarding the coordination environment of an absorbing species, as well as its oxidation and density of unoccupied electronicstates.[22–24] Although intensity of the L_1 quadrupole transition edge (2s - 4d) is low, the more intense $L_{2,3}$ (2p -4d) electric dipole transitions can instead be used to probe the oxidation state and electronic density around absorbing Mo ions in CPs without convolution from

p–d mixing, and can thereby serve as a direct probe of covalency of transition metals regardless of their crystal field.[25] Furthermore, lattice geometry can be determined through extended X-ray absorption fine structure (EXAFS) analysis that reveals structural distortions and bond distance information. This is accomplished through excitation by photons of energy greater than the absorption edge, which produces photoemitted electrons. Interference between outgoing wave components of the photoemitted electron from the X-ray excited atom and backscattered components from neighboring atoms provides information related to the interatomic distances between the absorber atom and those in its surrounding coordination shells. The combination of analyses in both regions of the XAS spectrum helps explain the charge transfer phenomena and differences in the structural properties of intercalated and binary Mo_6T_8 frameworks.

Herein, we report the analyses of XANES and EXAFS experiments that corroborate arguments regarding how metal intercalation into the CP sulfide, selenide, and telluride frameworks control cluster anisotropy, cavity deformation, and charge transfer. This work highlights the intricate effects of ternary intercalation on structure and electronic properties for a highly versatile material family, and thereby provides valuable insights that may inform and accelerate the design of new compositions with a variety of applications.

Results and Discussion

Synthesis and structural characterization Pure-phase binary and metal-intercalated CPs with the Mo_6S_8, Mo_6Se_8, Mo_6Te_8, $Cu_2Mo_6S_8$, $Cu_2Mo_6Se_8$, and $NiMo_6Te_8$ compositions were obtained through a rapid microwave-assisted solid-state synthesis approach described in our previous work,[10,11,13–15] with this being the first expansion of the synthesis approach to produce metal-intercalated CP selenides. Scanning electron microscopy (SEM) images reveal the faceted, polycrystalline morphology of these phases (Figure 2.2(a)–(c) and Figure S2.1a–c). A slight decrease in crystallinity was observed for the telluride phase, which agrees with the broader and less intense diffraction peaks for $NiMo_6Te_8$ compared to $Cu_2Mo_6S_8$ and $Cu_2Mo_6Se_8$. The powder

X-ray diffraction (PXRD) patterns for each CP are in close agreement with literature and indicate a rhombohedral crystal phase for $Cu_2Mo_6Se_8$, $Cu_2Mo_6S_8$, Mo_6S_8, Mo_6Se_8 and Mo_6Te_8 (Figure 2.2(d), (e) and Figure S2.1d–f). Additional diffraction peaks associated with a triclinic distortion are observed for $NiMo_6Te_8$, which agrees with results reported for the similar $Ni_{0.85}Mo_6Te_8$ composition (Figure 2.2(f)).[26]

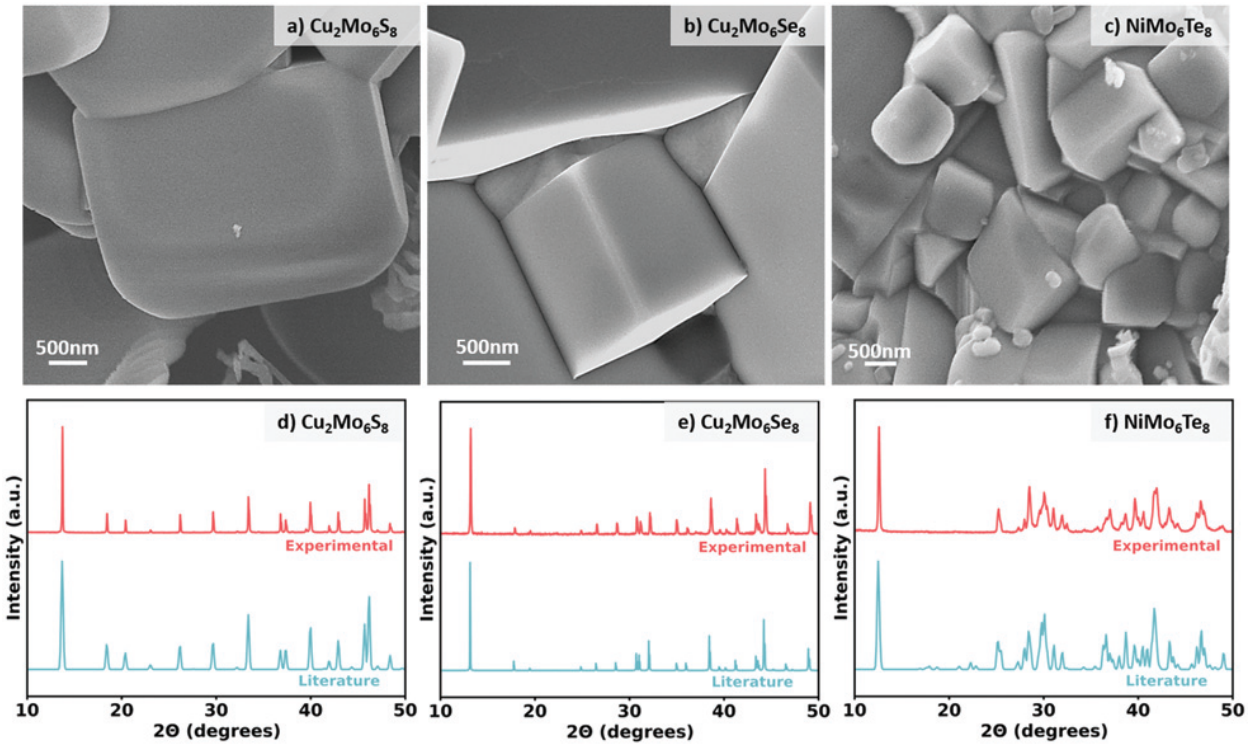


Figure 2.2. (a) SEM micrographs of (a) $Cu_2Mo_6S_8$, (b) $Cu_2Mo_6Se_8$ and (c) $NiMo_6Te_8$ along with their corresponding PXRD diffractograms (d)–(f).

All the phases synthesized in this work share a diffraction peak at $2\theta \approx 12°$, which is characteristic of CPs and corresponds to diffraction from the (101) and (010) planes for the rhombohedral and triclinic phases, respectively. A noticeable shift of this peak to lower 2θ values (Te < Se < S) was observed as the ionic radius of the chalcogen increases (S < Se < Te), agreeing with the increase in the unit cell volume (Figure S2.2). Additionally, a slight shift in 2θ to lower values for the rhombohedral structures was observed upon metal intercalation—a feature that is noticeably

more pronounced for CP selenides (Mo_6Se_8 << $Cu_2Mo_6Se_8$) than sulfides (Mo_6S_8 < $Cu_2Mo_6S_8$) (Figure S2.2). This appears to be the result of reduced chalcogen-intercalant attraction in $Cu_2Mo_6Se_8$ relative to $Cu_2Mo_6S_8$, which arises due to the decreased chalcogen electronegativity and resultant lack of electrostatic attraction between the Mo_6Se_8 cluster and the interstitial cation species linking them together.[15]

Local structure distortion upon intercalation

As previously mentioned, metal intercalation has a marked effect on the electronic and geometric structures of CPs. More specifically, insertion of metal ions into the cavities between Mo_6T_8 clusters induces alterations not only to the intercluster Mo–Mo, Mo–T, and T–T distances, but also to the intracluster Mo–Mo distances of the Mo6 trigonal antiprism. Thus, to understand the extent to which the host structure is modified by the ternary intercalant species, Mo K-edge EXAFS analysis was performed for Mo_6S_8, $Cu_2Mo_6S_8$, Mo_6Se_8, $Cu_2Mo_6Se_8$, Mo_6Te_8, and $NiMo_6Te_8$ CPs. Fourier-transformed EXAFS data, including magnitudes and real components, and corresponding fitted plots for the binary and intercalated sulfides, selenides, and tellurides are showcased for comparison in Figure 2.3.

Upon X-ray irradiation above the Mo K-edge energy (20 keV), generated photoelectrons scatter from the neighboring atoms surrounding the absorbing element. Due to the overlapping edges of the sulfur K-edge and molybdenum L_3-edge, the Mo K-edge was chosen for EXAFS fitting due to the non-interferent nature of the photoelectrons produced at the energy utilized, as well as the wealth of structural information extractable for the intercluster and intracluster Mo–Mo and Mo–T bonding landscape. Contributing scattering paths to the EXAFS signal are represented in Figure 2.4 and extracted distances from fitted data are detailed in Table S2.1. $Cu_2Mo_6Se_8$ and especially $Cu_2Mo_6S_8$ demonstrate appreciable increases in their intercluster Mo–T distances relative to their binary analogues of 0.1 and 0.03 Å, respectively. This increase in path length is consistent with the incorporation of multiple ions per cavity.

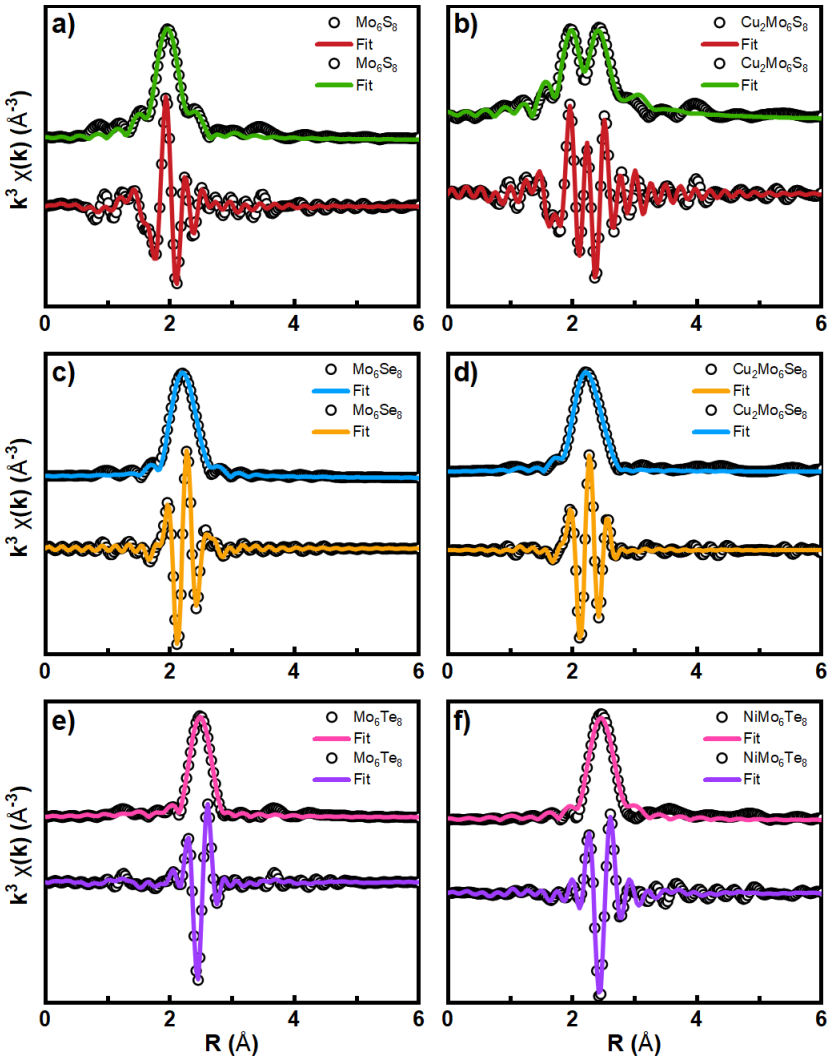


Figure 2.3. Mo K-edge FT-EXAFS data (circles) and fits (solid lines) showing the non-phase-corrected magnitude (top lines) and real (bottom lines) components of the Fourier transform of $k^3\chi(k)$ in radial space for the sulfide, selenide, and telluride binary CPs (a), (c), and (e), and the Cu intercalated sulfide and selenide (b), (d), and Ni intercalated telluride CPs (f).

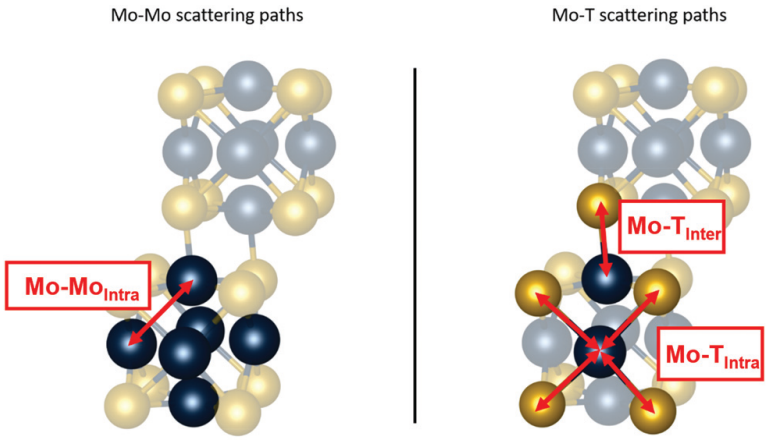
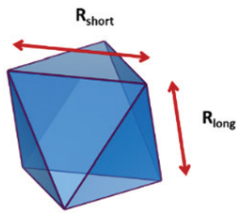


Figure 2.4. Graphic representation of the intracluster and intercluster scattering paths observed in Figure 2.3 for 1s photoelectrons between an absorbing Mo and its neighboring Mo and T ions in the CP framework. Information for each path is detailed in Table S2.1.

The introduction of intercalant metal ions causes structural transformations in both the chalcogen cage and the Mo_6 cluster. To quantify this structural shift, we monitored cluster anisotropy. The cluster anisotropy is defined here as the quotient between the longest and shortest Mo–Mo bond distances in the trigonal antiprism (Table 2.1). In conjunction with the elongation of intercluster Mo–T bonds, our results indicate a reduction in cluster anisotropy between the binary CPs and their respective ternary analogues, in good agreement with previous reports (Table 2.1).[21] In binary CPs, the two chalcogen ions located along the 3-fold rotation axis have a lower coordination number than the remaining 6 of the Mo_6T_8 cluster (Figure 1(b)). Thus, the lack of dative interactions from the chalcogen to neighboring clusters induces the undercoordinated chalcogens to bare a more negative charge, as demonstrated by Hughbanks and Hoffmann.[27] Upon intercalation, the occupation of intercluster cavities mitigates the undercoordination of these chalcogen sites and distributes their valency more evenly amongst the other chalcogen atoms.

Table 2.1. Cluster anisotropy relationship to the cluster valence electron count (VEC). The anisotropy was calculated following ref. 21, as $(R_{long} - R_{short}) \times 100/R_{long}$, where R depicts the interatomic distance between intracluster Mo atoms as obtained from Mo K edge EXAFS data (distances can be visualized in the blue polyhedron with each vertex representing a Mo atom). VEC was calculated according to ref. 21

Chevrel Phase	Cluster e-count	Cluster anisotropy (%)	
Mo_6S_8	20	8.85 ± 1.63	
$Cu_2Mo_6S_8$	22	4.44 ± 1.64	
Mo_6Se_8	20	5.55 ± 2.15	
$Cu_2Mo_6Se_8$	22	3.70 ± 1.52	
Mo_6Te8	20	4.73 ± 0.50	
$NiMo_6Te_8$	22	11.04 ± 0.43	

In the case of the intercalated telluride phase ($NiMo_6Te_8$), the cluster anisotropy shows a remarkable increase in comparison to the binary. This could be rooted in the lower electronegativity of the Te ions, thus leading to a lower degree of charge transfer with the intercalant cations, as well as in the distinct space groups between the binary and ternary telluride CPs. The triclinic crystal structure of $NiMo_6Te_8$, which lacks the 3-fold rotation axis of symmetry present in Mo_6Te_8, may impose a lower symmetry on the entire chalcogen cage, thus resulting in an inherently asymmetric Mo_6 cluster. To attain a clear understanding of the structural symmetry of the intercalated CP tellurides, additional EXAFS studies over a large composition spectrum are required.

Charge transfer in Chevrel Phases

Mo L_3-, S K-, Se K-, and Te L_3-edge excitations were probed to evaluate metal–chalcogen interactions and electron density distribution in each CP. It is known that Mo 4d orbitals play a critical role in previously observed S pre-edge features due to hybridization between Mo 4d and S 3p orbitals.[6,19] Vacant hybrid orbitals enhance the pre-edge region observed in the S K-edge. The addition of electron density to these hybridized orbitals from a ternary intercalant acting as an

electron donor results in a depressed pre-edge peak, as observed in Figure 2.5(b). Additionally, interactions between Mo and T have a substantial effect on the Mo L_3-edge absorption edge position and can provide additional electronic information for the Se and Te congeners, allowing for further analysis of the role that chalcogen electronegativity has on electron distribution within the cluster.

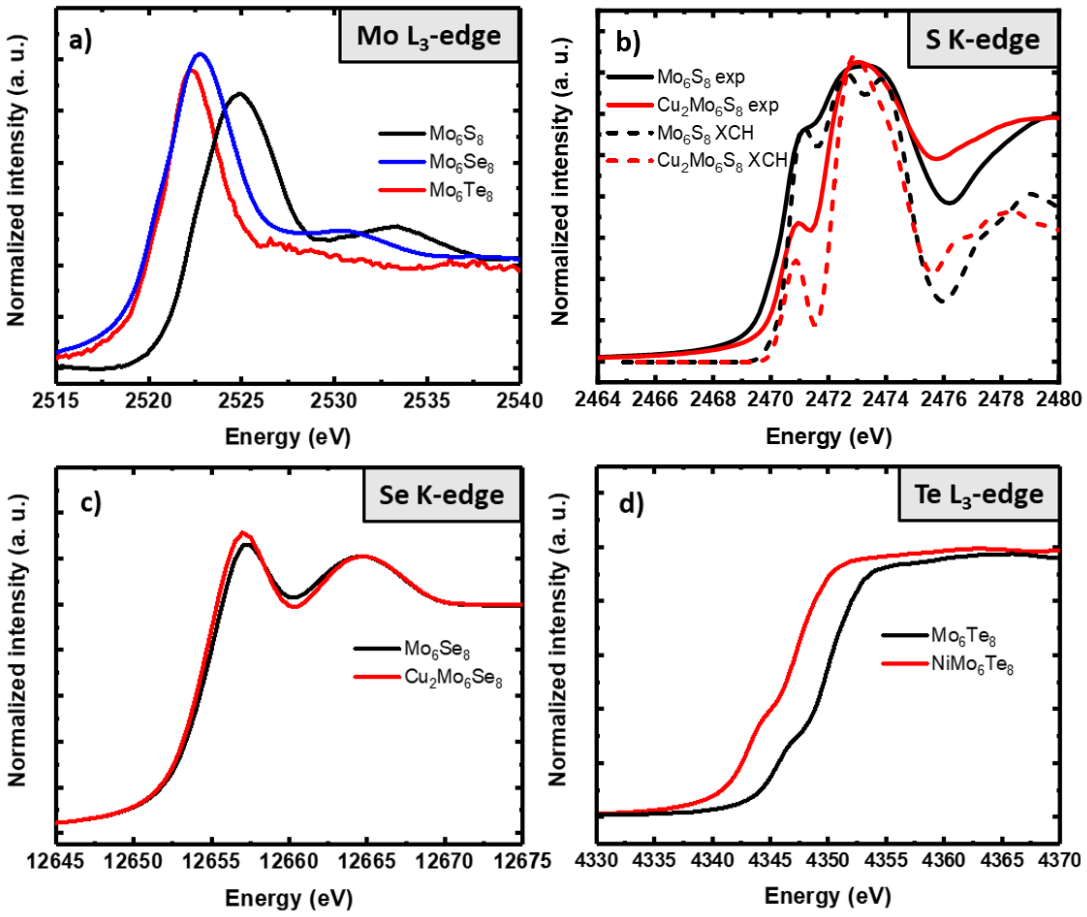


Figure 2.5. Molybdenum and chalcogen XANES spectra for binary and ternary Chevrel phases. (a) Mo L_3-edge of sulfide, selenide and telluride CPs, (b) S K-edge of Mo_6S_8 and $Cu_2Mo_6S_8$, the calculated spectra are shown with dashed lines (c) Se K-edge of Mo_6Se_8 and $Cu_2Mo_6Se_8$, and (d) Te L_3- edge of Mo_6Te_8 and $NiMo_6Te_8$.

Inspection of the Mo L_3-edge position shown in Figure S2.4 reveals the effect of ion intercalation on the valency of the Mo_6 host. Both sulfide and selenide CPs exhibit a redshifted Mo L_3-edge after 2 equivalents of Cu have been intercalated into the cavities. This lower absorption energy indicates a more reduced Mo species following electron donation from the intercalant into the cluster, subsequent redistribution of chalcogen valency, and resultant contraction of the clusters (Figure 2.3). Conversely, the telluride CP displays an opposite trend, with a small blue shift in the Mo L_3-edge following Ni intercalation. This observation is in good agreement with the previously described expansion of the Mo_6Te_8 cluster after intercalation (*vide supra* and detailed in Table S2.1). Bond lengthening upon metal intercalation of Mo_6Te_8 clusters develops a lower overall electron density of the molybdenum atoms. While perceptible, these energy shifts are small in magnitude, which is consistent with the general low redox activity of the Mo centers upon intercalation.[17,28] It is noteworthy that the effect of chalcogen composition and—more importantly—chalcogen electronegativity manifests itself in the electronic structure of the Mo_6 trigonal antiprism, as seen in the progressively blue shifted Mo L_3-edge centroids in Figure 2.5(a) along the series Mo_6Te_8 < Mo_6Se_8 < Mo_6S_8. Specifically, and perhaps intuitively, a more oxidized molybdenum species predominates as the chalcogen electronegativity increases. This result is of high importance, as Mo atoms are known to be the adsorption site of small molecules in catalytic applications,[9,13] hence selectively engendering programmable valency to these sites may afford a fine level of control over reactivity for a suite of applications. As a result of this promise for tuning Mo reactivity based upon chalcogen electronegativity, additional in situ and operando Mo XANES measurements are warranted that may elucidate the nature of Mo–adsorbate interactions during relevant reactions such as the CO_2 reduction and C–C coupling reactions.

Much like the Mo edges, chalcogen absorption edges provide valuable insight into the charge transfer phenomenon that occurs during ternary intercalation into CPs. Among these edges, the S K-edge illustrates the pronounced effect of intercalant-to-chalcogen charge transfer.

As can be seen in Figure 2.5(b), a modest red shift of the white line position is detected upon intercalation, although a rather abrupt decrease in the pre-edge (located around 2470.5 eV) intensity is observed, indicating significant population of previously unoccupied hybridized S 3p/Mo 4d states that are responsible for the pre-edge feature intensity. This population of 3p states by Cu donated electron density effectively depresses the pre-edge feature in the intercalated $Cu_2Mo_6S_8$ structure relative to the binary Mo_6S_8 that retains its unoccupied S 3p states that can accept excited electrons during the S 1s - S 3p/Mo 4d transition. This effect is more clearly visible from the analysis of the second derivatives of the corresponding spectra shown in Figure S2.6a where the binary sulfide CP exhibits two well-resolved peaks centered around 2470 eV. These peaks merge into a single signal upon intercalation of two copper equivalents and subsequent introduction of the intercalant electron density. Small metal cations such as Cu+ are known to occupy the cavity in a perpendicular fashion to the 3-fold rotation axis of the CP framework highlighted in Figure 1(b) and (c),[17] in closest proximity to undercoordinated S sites. Upon intercalation, electron density from the ternary cation is transferred to empty (4d hybridized) S 3p orbitals that are responsible for the pre-edge feature. As a result of orbital occupation from intercalant induced electron transfer, the spectra show a reduced intensity in the absorption pre-edge signal in the S K-edge XANES. The two resolved peaks at 2470 eV for the S-K 2nd derivative are merged to a single broad feature and this can be interpreted as a more uniform S valency distribution and coordination environment and, consequently, a less anisotropic Mo_6 trigonal antiprism.[18,19]

The S K-edge spectra of Mo_6S_8 an $Cu_2Mo_6S_8$ (Figure 2.5(b), dashed lines) were calculated using the many-body X-ray absorption spectroscopy method (MBXAS),[29–31] a density functional theory-based methodology that computes the absorption cross-section by approximating each electronic state (i.e., the initial state and each of the final states) as a Slater determinant (see Computational details in the supporting information). The anisotropy of the simulated structural models is, respectively, 5.76% and 3.31%, in excellent agreement with experiment (Table 2.1), as

are the spectra. Bader charge analysis of the Mo_6S_8 and $Cu_2Mo_6S_8$ structures confirms that the intercalant-induced electron transfer is mostly to the previously undercoordinated S2 sites (see Table S2.9), which are reduced by 0.16 e^-. On the other hand, the Mo and the tetracoordinated S1 sites are reduced by less than 0.08 e^-. The charge on S_1 and S_2 sites equalizes to ~ -0.80 e^- in the intercalated phase, reflecting the reduced cluster anisotropy of $Cu_2Mo_6S_8$ and their corresponding atomic contributions to the overall spectrum bear closer resemblance to one another (Figure S2.8), leading to the disappearance of the pre-edge. The strong-blue shift in the S_2 spectra is mainly due to the presence of the Cu, rather than the geometric changes associated with it. Counterintuitively, the steepness of the pDOS near the Fermi level indicates a decrease in charge carriers when Cu is added, and the Fermi level raised. This results in decreased screening, hence the blue-shift (see supporting information section *Effect of geometric changes and charge transfer on spectra*). We note that, in contrast to the expected greater negativity of the undercoordinated S_2 atom, Bader charges indicate less negative charge on these sites. However, the associated atomic volume for these atoms is quite large, due to the open structure of the lattice, and a more localized charge estimate (Löwdin charge) does indeed indicate that S_2 is slightly more reduced than S_1 (Table S2.8). In the case of the Se K-edge, there is no appreciable pre-edge feature and no change in intensity of the edge is noticeable upon intercalation. This may be rooted in a lower degree of Mo d–T p orbital hybridization as a result of a larger orbital energy mismatch between the elements. In addition, the lack of well-defined pre-edge absorption peaks in the heavier chalcogens is consistent with the decrease in the core-hole lifetime of their corresponding high energy edges compared to sulfur. Cu-intercalated selenide and Ni-intercalated telluride CPs both demonstrate a decrease in absorption onset energies in their respective chalcogen XANES spectra, in good agreement with more reduced Se and Te species. In comparing the Mo L_3-edge spectra for the CPs studied here (Figure S2.4), the electronic structure changes as evidenced by shifting chalcogen absorption edges indicate that charge transfer occurs primarily from the intercalant to the chalcogen cages, rather than directly to the Mo_6 core, despite the redistribution

of Mo valency upon intercalation. However, this M-to-T electron transfer shows good agreement with previous results published by Prendergast et al.[32] These changes in absorption edge positions and intensities highlight the significance of identifying useful sites within the CP structure that are amenable to selectively accepting electron density during intercalation by a ternary species.

Conclusions

We have presented an extensive XAS study on the atomistic and electronic structure of Chevrel Phases and on their evolution upon intercalation by a ternary species. Results extracted from Mo K-edge EXAFS confirm the reduction of Mo_6 cluster anisotropy after metal insertion, which we attribute to a more evenly distributed chalcogen valency. Modulated charge density of the Mo_6 cluster as a function of chalcogen electronegativity was also evidenced by a red shift in the Mo L_3-edge absorption edge centroid for the binary series Mo_6T_8 with a decrease in energy as the electronegativity of the chalcogen decreases. Additionally, by comparing the Mo L_3- and chalcogen K- and L_3-edge XANES of binary and metal-intercalated CPs, it was concluded that charge transfer is mediated by the chalcogen, with the most noticeable effects observed for the S K pre-edge feature and Te L_3-edge red-shift after metal intercalation. The results of this work provide a detailed view of the effect of intercalation on the atomic structure and anisotropy of Chevrel Phase sulfide, selenide and tellurides. Furthermore, the effect of the chalcogen identity on the Mo cluster electronic structure and its change after interaction with the ternary cation in $M_xMo_6T_8$ phases suggest how the ternary CPs may be rationally tuned for their applications of interest.

Acknowledgements

We thank the University of California, Davis for start-up funding. JMV also acknowledges support from the Cottrell Scholars program supported by the Research Corporation for Science Advancement (RCSA 26780), as well as support from the National Science Foundation through the Faculty Early Career Development Program (DMR-2044403). JOR was funded by the

National Science Foundation Graduate Research Fellowship (NSF 1650042). Part of this study was carried out at the UC Davis Center for Nano and Micro Manufacturing (CNM2). Use of the Stanford Synchrotron Radiation Lightsource, SLAC National Accelerator Laboratory, is supported by the U.S. Department of Energy, Office of Science, Office of Basic Energy Sciences under Contract No. DE-AC02-76SF00515. This research used resources of the National Synchrotron Light Source, a U. S. Department of Energy (DOE) Office of Science User Facility operated for the DOE Office of Science by Brookhaven National Laboratory under Contract No. DE-AC02- 98CH10886. DFT calculations and X-ray spectral analysis were performed by ASM, SR, and DP using resources of the National Energy Research Scientific Computing Center (NERSC), a U. S. Department of Energy Office of Science User Facility located at Lawrence Berkeley National Laboratory, operated under Contract No. DE-AC02-05CH11231. Work by ASM was supported by the Joint Center for Energy Storage Research (JCESR), an Energy Innovation Hub funded by the U.S. Department of Energy, Office of Science, Basic Energy Sciences. Spectral analysis was facilitated through a user project at the Molecular Foundry at Lawrence Berkeley National Laboratory, which is supported by the Office of Science, Office of Basic Energy Sciences, of the U. S. Department of Energy under Contract No. DE-AC02-05CH11231. NRS and CBM acknowledge support by the National Science Foundation (CBET-2016225).

Publication Information, Copyright, and Author Acknowledgements

This chapter forms the basis for the following publication:

Hyler, F. P.*; **Wuille Bille, B. A.***; Ortiz-Rodriguez, J. C.; Sanz Matías, A.; Roychoudhury, S.; Perryman, J. T.; Patridge, C. J.; Singstock, N. R.; Musgrave, C. B.; Prendergast, D. G.; Velázquez, J. M. "X-ray absorption spectroscopy insights on the structure anisotropy and charge transfer in Chevrel phase chalcogenides", *Phys. Chem. Chem. Phys.* **2022**, 24, 17289-17294, DOI: 10.1039/D1CP04851A

* Joint first author

This chapter was adapted with permission from Hyler, F. P.*; Wuille Bille, B. A.*; Ortiz-Rodriguez, J. C.; Sanz Matías, A.; Roychoudhury, S.; Perryman, J. T.; Patridge, C. J.; Singstock, N. R.; Musgrave, C. B.; Prendergast, D. G.; Velázquez, J. M. "X-ray absorption spectroscopy insights on the structure anisotropy and charge transfer in Chevrel phase chalcogenides", *Phys. Chem. Chem. Phys.* **2022**, 24, 17289-17294. © Copyright 2022 Royal Society of Chemistry

References

(1) R. Chevrel, M. Sergent and J. Prigent, *J. Solid State Chem.*, **1971**, 3, 515–519.

(2) G. V. Subba Rao and G. Balakrishnan, *Bull. Mater. Sci.*, **1984**, 6, 283–316.

(3) Ø. Fischer, *Appl. Phys.*, **1978**, 16, 1–28.

(4) X. Ya Shi, L. Wang, L. D. Chen and X. H. Chen, *Trans. Nonferrous Met. Soc. China,* **2009**, 19, 642–645.

(5) A. Mitelman, M. D. Levi, E. Lancry, E. Levi and D. Aurbach, *Chem. Commun.*, **2007**, 4212–4214.

(6) D. Muthuraj and S. Mitra, *Mater. Res. Bull.*, **2018**, 101, 167–174.

(7) E. Lancry, E. Levi, Y. Gofer, M. Levi, G. Salitra and D. Aurbach, *Chem. Mater.*, **2004**, 16, 2832–2838.

(8) P. Yu, X. Long,N. Zhang, X. Feng, J. Fu, S. Zheng,G. Ren, Z. Liu, C. Wang and X. Liu, *J. Phys. Chem. Lett.*, **2019**, 10, 1159–1166.

(9) K. M. Kadiev, S. N. Khadzhiev, M. K. Kadieva and E. S. Dogova, *Pet. Chem.*, **2017**, 57, 608–617.

(10) J. T. Perryman, F. P. Hyler, J. C. Ortiz-Rodríguez, A. Mehta, A. R. Kulkarni and J. M. Velázquez, *J. Coord. Chem.*, **2019**, 72, 1322–1335.

(11) J. T. Perryman, J. C. Ortiz-Rodríguez, J. W. Jude, F. P. Hyler, R. C. Davis, A. Mehta, A. R. Kulkarni, C. J. Patridge and J. M. Velázquez, *Mater. Horiz.*, **2020**, 7, 193–202.

(12) O. K. Andersen, W. Klose and H. Nohl, *Phys. Rev. B: Condens. Matter Mater. Phys.*, **1978**, 17, 1209–1237.

(13) J. C. Ortiz-Rodríguez, N. R. Singstock, J. T. Perryman, F. P.Hyler, S. J. Jones, A. M. Holder, C. B. Musgrave and J. M. Velázquez, *ACS Appl. Mater. Interfaces*, **2020**, 12, 35995–36003.

(14) K. Lilova, J. T. Perryman, N. R. Singstock, M. Abramchuk, T. Subramani, A. Lam, R. Yoo, J. C. Ortiz-Rodríguez, C. B. Musgrave, A. Navrotsky and J. M. Velázquez, *Chem. Mater.*, **2020**, 32, 7044–7051.

(15) N. R. Singstock, J. C. Ortiz-Rodríguez, J. T. Perryman, C. Sutton, J. M. Velázquez and C. B. Musgrave, *J. Am. Chem. Soc.*, **2021**, 143, 9113–9122.

(16) F. J. Berry, E. M. Forgan and C. D. Gibbs, *Solid State Commun.*, **1988**, 66, 667–670.

(17) F. J. Berry and C. D. Gibbs, *Solid State Commun.*, **1992**, 83, 517–520.

(18) J. K. Burdett and J. H. Lin, *Inorg. Chem.*, **1982**, 21, 5–10.

(19) F. Kubel and K. Yvon, *J. Solid State Chem.*, **1988**, 73, 188–191.

(20) J. D. Corbett, *J. Solid State Chem.*, **1981**, 39, 56–74.

(21) E. Levi and D. Aurbach, *Chem. Mater.*, **2010**, 22, 3678–3692.

(22) T. K. Sham, Phys. Rev. B: Condens. *Matter Mater. Phys.*, **1985**, 31, 1888–1902.

(23) F. Farges and G. E. Brown, *Phys. Rev. B: Condens. Matter Mater. Phys.*, **1997**, 56, 1809–1819.

(24) M. Tromp, J. Moulin, G. Reid and J. Evans, *AIP Conf. Proc.*, **2007**, 882, 699–701.

(25) M. L. Baker,M. W. Mara, J. J. Yan, K. O. Hodgson, B. Hedman and E. I. Solomon, *Coord. Chem. Rev.*, **2017**, 345, 182–208.

(26) K. Hönle and W. Yvon, *J. Solid State Chem.*, **1987**, 240, 235–240.

(27) T. Hughbanks and R. Hoffmann, *J. Am. Chem. Soc.*, **1983**, 105, 1150–1162.

(28) K. Asokan, O. Peña, L. Le Polles, J. C. Jan, J. W. Chiou and W. F. Pong, *J. Cluster Sci.*, **2009**, 20, 205–211.

(29) Y. Liang, J. Vinson, S. Pemmaraju, W. S. Drisdell, E. L. Shirley and D. Prendergast, *Phys. Rev. Lett.*, **2017**, 118, 1–7.

(30) Y. Liang and D. Prendergast, *Phys. Rev. B: Condens. Matter Mater. Phys.*, **2019**, 100, 1–12.

(31) Y. Liang and D. Prendergast, *Phys. Rev. B: Condens. Matter Mater. Phys.*, **2018**, 97, 1–25.

(32) L. F. Wan, J. Wright, B. R. Perdue, T. T. Fister, S. Kim, C. A. Apblett and D. Prendergast, *Phys. Chem. Chem. Phys.*, **2016**, 18, 17326–17329.

Supporting information

- **Materials**

MoS_2 powder (99%, ~325 mesh), Cu powder (99.995%, ~100 mesh), $MoSe_2$ powder (99.999%, ~200 mesh) and Ni powder (99.8%, ~325 mesh) were used as purchased from Alfa Aesar. Mo powder (99.99%, ~100 mesh) and Te powder (99.8%, ~200 mesh) were used as purchased from Sigma Aldrich. Fused quartz tubes (2 mm thick) were purchased from AdValue Technology and made into round-bottom tubes with an in-house oxy-hydrogen torch.

- **Synthesis and characterization**

$Cu_2Mo_6S_8$, Mo_6Se_8, $Cu_2Mo_6Se_8$, Mo_6Te_8 and $NiMo_6Te_8$ were all synthesized through a microwave-assisted solid-state synthesis approach described in detail in our previous work.[1–3] In short, precursors powders were stoichiometrically mixed in an N_2 filled glovebox (e.g., for 3 g of $Cu_2Mo_6S_8$, 0.7949 g of Cu, 2.0025 g of MoS_2, and 0.2000 g of Mo are mixed) and ball milled overnight. The mixed powders were pressed into a pellet disk of 20 mm^2 of surface area, packed in a quartz tube under inert atmosphere and heated inside a graphite (powder, < 20 μm) bath in a conventional microwave oven for up to 10 minutes. CP sulfides and selenides were obtained after 10 min of heating at a power of up to 1000 W, reaching temperatures between 1000-1200°C. The power level was adjusted accordingly to maintain a temperature between 900 and 1000°C for the telluride phase to avoid synthesizing a mixture of CP telluride and metallic Mo that is observed at higher temperatures due to Te loss. Owing to the metastability of Mo_6S_8 at high temperatures, this phase was obtained by de-intercalating Cu from $Cu_2Mo_6S_8$ through chemically etching in O_2-bubbled 6.0 M HCl according to literature methods.[4] Phase purity of each CP was confirmed through PXRD using a Bruker D8 Advance diffractometer with Cu K-alpha radiation (1.5406 Å), while morphology was evaluated using a FEI (Hillsboro, OR) 430 Nano Scanning Electron Microscope (SEM).

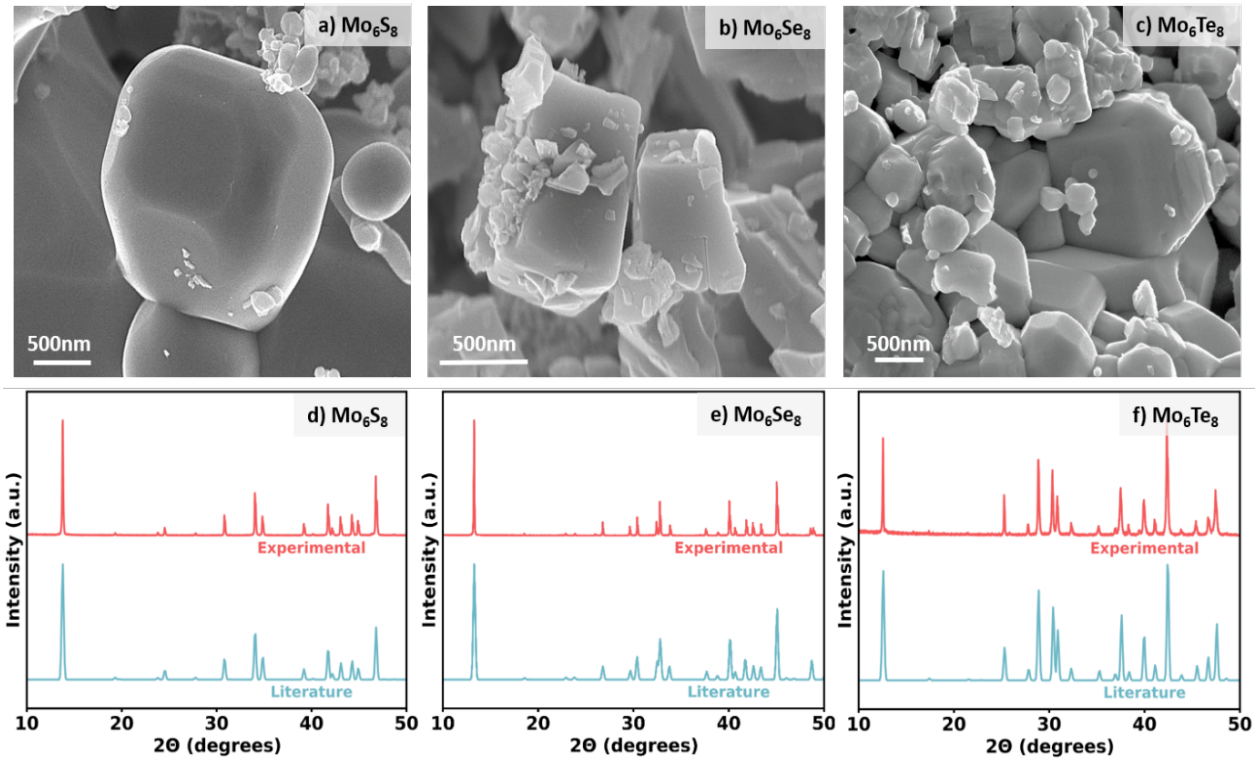


Figure S2.1. SEM Micrographs of a) Mo_6S_8, b) Mo_6Se_8 and c) Mo_6Te_8 along their corresponding PXRD diffractograms d) - f).

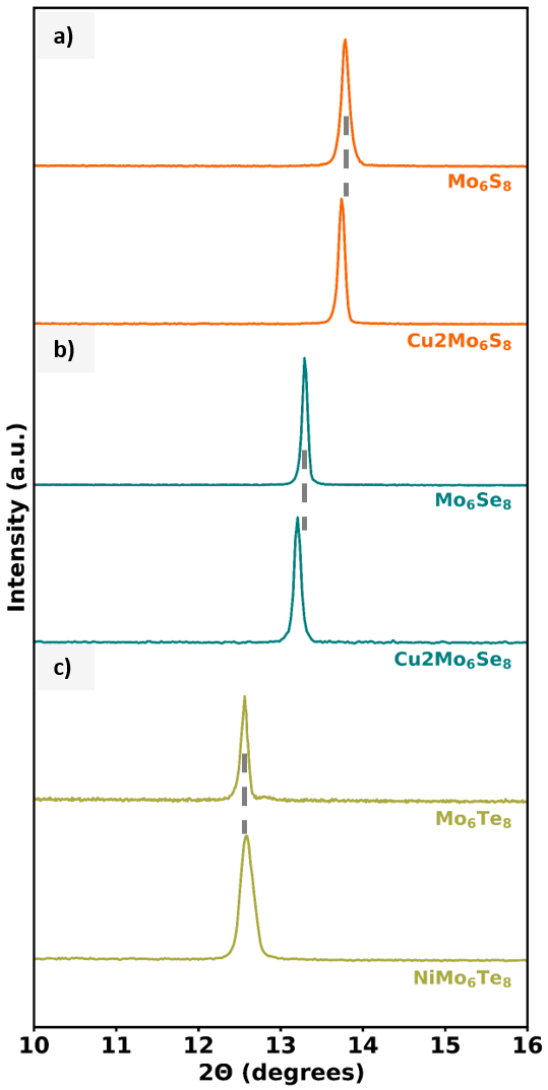


Figure S2.2. Changes in 2θ values for the diffraction peak in the (101) plane upon metal intercalation in CP sulfides **a)** and selenides **b)**. Metal intercalation in CP tellurides results in a triclinic distortion, in which the diffraction peak ~2θ = 12.5° corresponds to diffraction in the (101) and (010) for binary CP telluride and metal intercalated CP telluride, respectively **c)**.

- **XAS data analysis of Chevrel-phases**

To ensure the resulting amplitude within the k-space is accurate, samples were first ground down into fine powder using a mortar and pestle. Subsequently, acetone was added to the resulting powder to create a suspension of the smaller particles. The suspension was then drop cast onto a glass slide and allowed to dry. Once dried, the powder was scrapped onto Kapton tape used as a transparent film for X-ray analysis. Mo_6S_8, $Cu_2Mo_6S_8$, Mo_6Se_8, $Cu_2Mo_6Se_8$, Mo_6Te_8, $NiMo_6Te_8$ were all screened at their respective Mo K-edge, corresponding chalcogen edges: Te L_{III}-edge, S K-edge, Se K-edge, and their metal promoter K-edge (Cu and Ni). CPs were screened at Mo, T, and M K- and L- edges at SSRL beamline 4-1 (Mo K-edge, Cu K-edge, Ni K-edge, Se K-edge, and Te L-edge), SSRL beamline 4-3 (S K-edge, Mo L-edge), and NSLS 6-BM (Mo K-edge). For each analysis, a reference foil of the corresponding element edge was placed downstream from the sample chamber in transmission data acquisition mode and fluorescence signal was taken simultaneously to allow for post-analysis calibration of the beam energy. For S K-edge scans, $Na_2S_2O_3$ powder was used as a standard where the position of the white line peak was set to 2472.04 eV.[5–7] It is to be noted that multiple standards have been used in previous studies (such as the peak position of the elemental sulfur S K-edge[8] and molybdenum foil L_3-edge[9]).

Each edge scan <5000 eV was performed under He to mitigate beam interactions with O_2/N_2 which can diminish the fluorescence signal intensity, while edge scans >5000 eV were performed under ambient atmospheric conditions. Spectra were acquired in triplicate and averaged prior to data analysis to improve signal-to-noise ratio. All reported results correspond to fluorescence data collected with a Lytle detector.

- **EXAFS analysis**

Full X-ray absorption (including XANES and EXAFS regions) spectra for each of the elements in the six Chevrel-phases that were investigated were first averaged in *SixPack*. Post-processing of data was performed in *Athena*[10] version 0.9.26 including normalization of spectra

resulting from the pre- and post-edge regions of each respective edge. Mo K-edge X-ray absorption spectra were used fully after averaging. In cases where there was edge overlap, for example in Mo_6S_8 where the Mo L_3-edge is located 50 eV past the S K-edge, data was truncated to properly delimit each edge region. The processed data was then imported into *Artemis,* version 0.9.26, where the corresponding real-space data was fit with theoretical models that were established using structural information from the International Crystallographic Structure Database using IFEFFIT model for numerical calculations.[10,11]

Amplitude reduction factors (S_0^2) which account for multiple-electron excitations of an absorbing atom were treated as empirical parameters in the EXAFS analysis, and were calculated using the appropriate metal reference.[12] Debye-Waller factors (σ^2) which relate to the thermal motion of a system, specifically thermal disorder of crystalline solids were defined as being identical for any species that had similar bonding environments (e.g. Mo – S_1 and Mo – S_2 paths were treated with the same Debye-Waller factor). ΔE_0 is the relative difference between the edge position of a metal reference against the data's edge position. This parameter has a strong correlation with Δr for various paths. Identification of each ΔE_0 was ascribed to the first derivative of the Mo K-edge plot shown in **Figure S2.3**. **Table S2.1** showcases the scattering element, scattering pathway with the corresponding path label associated with **Figure 2.3**, and the distance that was calculated for the scattering paths, all of which show good agreement with previously reported crystallographic data.[13]

Path length information from the EXAFS region of the Mo-K edge was acquired for all Chevrel-phase samples. The values obtained through this analysis were used to calculate the % anisotropy of the materials which is shown in **Table 2.1**.

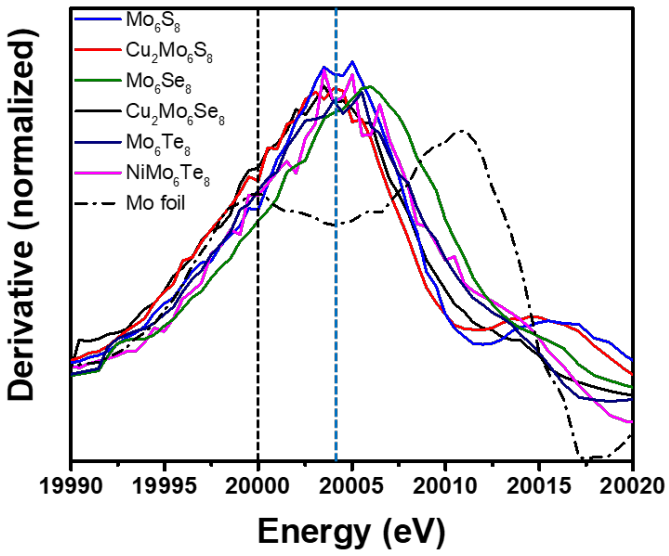


Figure S2.3. First derivative of the Mo K-edge

Table S2.1. Scattering path distances obtained through Mo K-edge EXAFS data fitting for the sulfide, selenide and telluride CPs. Path labels correspond to those represented graphically in Figure 2.4.

Chevrel-Phase	Scattering Path	Distance (Å)
Mo_6S_8	Mo-Mo_{intra}	2.78, 3.05
	Mo-S_{inter}	2.52
	Mo-S_{intra}	2.40
$Cu_2Mo_6S_8$	Mo-Mo_{intra}	2.58, 2.70
	Mo-S_{inter}	2.28
	Mo-S_{intra}	2.42
Mo_6Se_8	Mo-Mo_{intra}	2.72, 2.88
	Mo-Se_{inter}	2.65
	Mo-Se_{intra}	2.65, 2.54
$Cu_2Mo_6Se_8$	Mo-Mo_{intra}	2.60, 2.70
	Mo-Se_{inter}	2.56
	Mo-Se_{intra}	2.51, 2.52
Mo_6Te_8	Mo-Mo_{intra}	2.62, 2.75
	Mo-Te_{inter}	----
	Mo-Te_{intra}	2.79, 2.97
$NiMo_6Te_8$	Mo-Mo_{intra}	2.74, 3.08
	Mo-Te_{inter}	---
	Mo-Te_{intra}	2.79

Cluster anisotropy calculation

The Mo_6 cluster anisotropy was determined as the difference between the longest and shortest Mo-Mo interatomic distances (obtained from EXAFS analysis and detailed in **Table S2.1**) following Levi and Aurbach,[13] equation S2.1:

$$\%Anisotropy = \frac{R_{long} - R_{short}}{R_{long}} 100\% \quad \text{(S2.1)}$$

The uncertainty in the anisotropy values shown in Table 2.1 of the manuscript was obtained through the error propagation detailed in equation S2.2:

$$\Delta Anisotropy = \sqrt{\left(\frac{R_{short}}{{R_{long}}^2} x\ 100\ x\ \Delta R_{long}\right)^2 + \left(-\frac{100}{R_{long}} x\ \ \Delta R_{short}\right)^2} \quad \text{(S2.2)}$$

- **XANES analysis**

Interpretation of edge position can give insight into oxidation state changes, or the effect of polarization of the ions. **Figure S2.4a and b** identify the red shift observed in cases of metal intercalation for CP sulfides and selenides. In contrast, the tellurides experience a blue shift upon intercalation of Ni (**Figure S2.4c**).

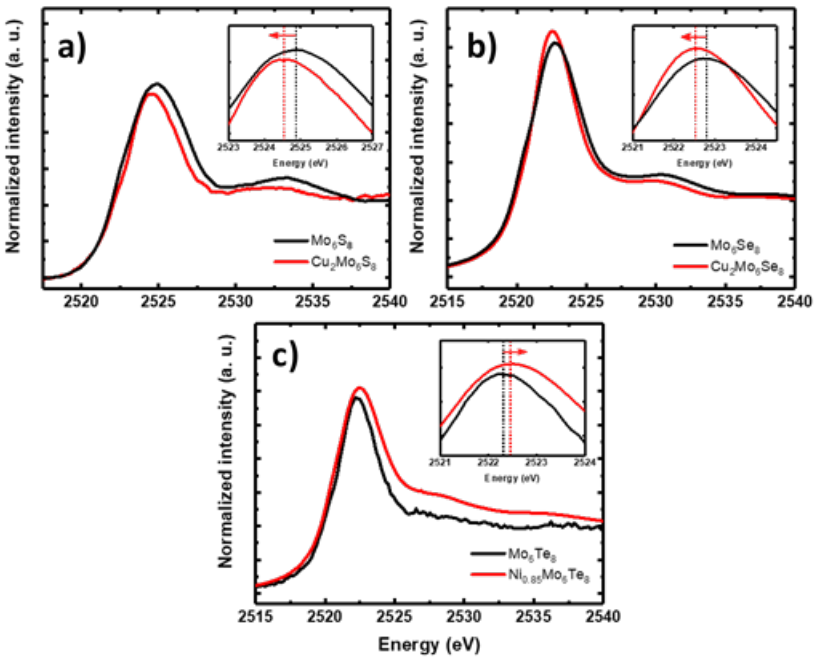


Figure S2.4. Mo L_3-edge XANES spectra corresponding to the binary and ternary $M_XMo_6T_8$ Chevrel phases demonstrating the effect of intercalation. Comparison between: **a)** Mo_6S_8 and $Cu_2Mo_6S_8$, **b)** Mo_6Se_8 and $Cu_2Mo_6Se_8$, **c)** Mo_6Te_8 and $NiMo_6Te_8$, and insets highlight the observed energy shifts with dotted lines through peak maxima.

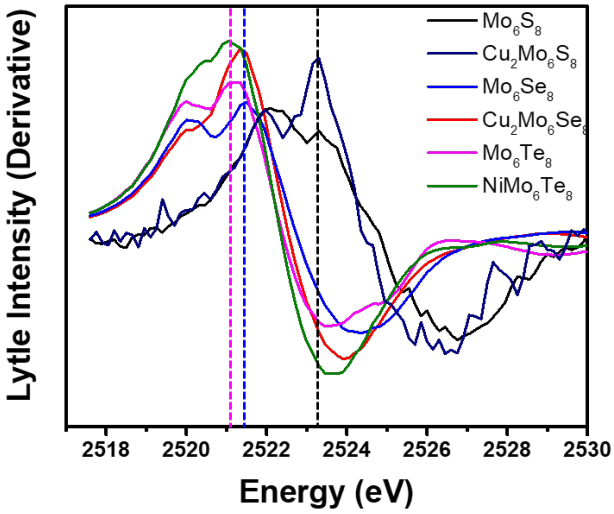


Figure S2.5. First derivative plots of the normalized Mo L_3-edge containing insets detailing the maxima for each binary Chevrel-phase.

As detailed in Figure S2.5, there is a relative shift in the white-line position that agrees with relative shifts observed in the first derivative analysis of the Mo L_3-edge. Specifically, the peak maxima detailed in Figure S2.5 are listed in Table S2.2.

Table S2.2. Peak maximum of the first derivative of the Mo L_3-edge.

Material	First Derivative Peak Maxima (eV)
Mo_6S_8	2522.1
$Cu_2Mo_6S_8$	2521.95
$Cu_2Mo_6Se_8$	2121.5
Mo_6Se_8	2121.35
$Cu_2Mo_6Te_8$	2521.2
$NiMo_6Te_8$	2521.35

To further interpret the edge-position, the second derivative of each edge scan was analyzed. **Figure S2.3a** highlights the unique observation of a pre-edge feature in the sulfur K-edge which arises due to the empty orbitals of predominant chalcogen character present in the binary CPs.[14] Upon metal intercalation, the S is fully coordinated which results in a more degenerate species and a lessened or lack of pre-edge feature dependent upon the number of ions inserted in the framework.[14]

The selenides and tellurides were also analyzed using the same second derivative method to understand pre-edge features that may arise but difficult to discern from the absorption edges alone. While no pre-edge features were present, both selenide and telluride CPs show a substantial shift in their respective chalcogen edge. **Figure S2.6b** identifies the second derivative of the XANES for the selenide CP before and after intercalation, where a subtle difference in the inflection point is observed. This inflection point can be defined as the true edge position, and present in both selenide and telluride data.

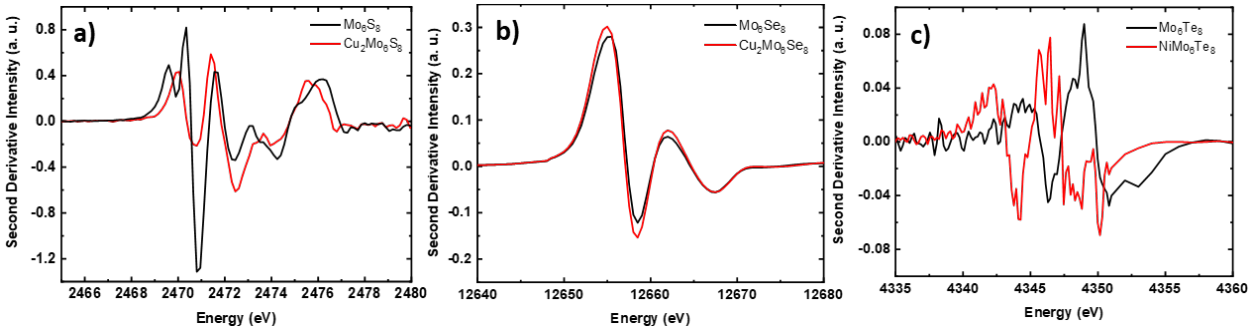


Figure S2.6. Second derivative of the respective chalcogen K- (S and Se) and L-edge (Te) spectra in **a)** Mo_6S_8 and $Cu_2Mo_6S_8$, **b)** Mo_6Se_8 and $Cu_2Mo_6Se_8$ and **c)** Mo_6Te_8 and $NiMo_6Te_8$. **a)** the twin peaks located at 2470 which unify into a single signal upon copper intercalation and the sulfur atoms along the threefold rotation are fully coordinated. **b)** focuses on the slight Se K-edge shift which occurs upon metal intercalation.

Table S2.3. Fitting parameters for the Mo K-edge of Mo_6Se_8. S_0^2 is the amplitude reduction factor, E_0 is the energy of the white line, σ^2 is the Debye-Waller factor, N is the scattering path degeneracy. The distances obtained from the EXAFS analysis are listed as Absorber-Scatterer pairs.

Chevrel-phase	Parameter	Value		R-factor
Mo_6Se_8	S_0^2	0.8	Set	0.00166193
	E_0	5.9	Set	
	σ^2_{Mo}	0.009	+/- 0.007	
	σ^2_{Se}	0.001	+/- 0.001	
	Mo-Se1	2.54 Å	+/- 0.01	
	Mo-Se2	2.65 Å	+/- 0.02	
	Mo-Mo1	2.72 Å	+/- 0.04	
	Mo-Mo2	2.88 Å	+/- 0.05	
	N (Mo-Se1)	3	Set	
	N (Mo-Se2)	2	Set	
	N (Mo-Mo1)	2	Set	
	N (Mo-Mo2)	2	Set	
	R-range	1.6 – 3.2 Å	Set	
	k-range	3 – 14.6 $Å^{-1}$	Set	

Table S2.4. Fitting parameters for the Mo K-edge of Mo_6S_8

Chevrel-phase	**Parameter**	**Value**		**R-factor**
Mo_6S_8	S_0^2	0.8	set	0.0084271
	E_0	5	set	
	σ^2_{Mo}	0.001	+/- 0.0004	
	σ^2_S	0.016	+/- 0.002	
	Mo-S1	2.52 Å	+/- 0.02	
	Mo-S2	2.40 Å	+/- 0.00	
	Mo-Mo1	2.78 Å	+/- 0.02	
	Mo-Mo2	3.05 Å	+/- 0.05	
	N (Mo-S1)	1	Set	
	N (Mo-S2)	4	Set	
	N (Mo-Mo1)	4	Set	
	R-range	1.5 – 3.5 Å	Set	
	k-range	3 – 13.2 $Å^{-1}$	Set	

Table S2.5. Fitting parameters for the Mo K-edge of Mo_6Te_8

Chevrel-phase	**Parameter**	**Value**		**R-factor**
Mo_6Te_8	S_0^2	0.85	set	0.0018176
	E_0	5.0	set	
	σ^2_{Mo}	0.023	+/- 0.001	
	σ^2_{Te}	0.024	+/- 0.002	
	Mo-Te1	2.79 Å	+/- 0.01	
	Mo-Te2	2.97 Å	+/- 0.02	
	Mo-Mo1	2.62 Å	+/- 0.01	
	Mo-Mo2	2.75 Å	+/- 0.01	
	N (Mo-Te1)	2	Set	
	N (Mo-Te2)	2	Set	
	N (Mo-Mo1)	2	Set	
	N (Mo-Mo2)	2	Set	
	R-range	1 – 3.5 Å	Set	
	k-range	3 – 14.6 $Å^{-1}$	Set	

Table S2.6. Fitting parameters for the Mo K-edge of $Cu_2Mo_6S_8$

Chevrel-phase	Parameter	Value		R-factor
$Cu_2Mo_6S_8$	S_0^2	0.85	set	0.024248
	E_0	4.5	set	
	σ^2_{Mo}	0.001	+/- 0.001	
	σ^2_{S}	0.001	+/- 0.003	
	σ^2_{Cu}	0.008	+/- 0.008	
	Mo-S1	2.28 Å	+/- 0.05	
	Mo-S2	2.42 Å	+/- 0.02	
	Mo-S3	2.42 Å	+/- 0.02	
	Mo-Mo1	2.58 Å	+/- 0.04	
	Mo-Mo2	2.70 Å	+/- 0.02	
	Mo-Cu1	3.27 Å	+/- 0.07	
	N (Mo-S1)	1	Set	
	N (Mo-S2)	2	Set	
	N (Mo-S3)	2	Set	
	N (Mo-Mo1)	2	Set	
	N (Mo-Mo2)	2	Set	
	N (Mo-Cu1)	2	Set	
	R-range	1 – 3.2 Å	Set	
	k-range	3 – 13.2 $Å^{-1}$	Set	

Table S2.6. Fitting parameters for the Mo K-edge of $CuMo_6Se_8$

Chevrel-phase	**Parameter**	**Value**		**R-factor**
$Cu_2Mo_6Se_8$	S_0^2	0.8	set	0.0089445
	E_0	4.2	set	
	σ^2_{Mo}	0.005	+/- 0.002	
	σ^2_{Se}	0.007	+/- 0.006	
	Mo-Se1	2.56 Å	+/- 2.22	
	Mo-Se2	2.51 Å	+/- 1.07	
	Mo-Se3	2.52 Å	+/- 0.02	
	Mo-Mo1	2.60 Å	+/- 0.04	
	Mo-Mo2	2.70 Å	+/- 0.01	
	N (Mo-Se1)	1	Set	
	N (Mo-Se2)	2	Set	
	N (Mo-Se3)	2	Set	
	N (Mo-Mo1)	2	Set	
	N (Mo-Mo2)	2	Set	
	R-range	1.5 – 3.5 Å	Set	
	k-range	3 – 14.9 $Å^{-1}$	Set	

Table S2.7. Fitting parameters for the Mo K-edge of $NiMo_6Te_8$

Chevrel-phase	**Parameter**	**Value**		**R-factor**
$NiMo_6Te_8$	S_0^2	0.8	set	0.0323450
	E_0	4.6	set	
	σ^2_{Mo}	0.001	+/- 0.001	
	σ^2_{Te}	0.003	+/- 0.007	
	Mo-Te1	2.79 Å	+/- 0.01	
	Mo-Mo1	2.74 Å	+/- 0.01	
	Mo-Mo2	3.08 Å	+/- 0.01	
	N (Mo-Te1)	4	Set	
	N (Mo-Mo1)	3	Set	
	N (Mo-Mo2)	1	Set	
	R-range	1.55 – 4 Å	Set	
	k-range	3 – 13.2 $Å^{-1}$	Set	

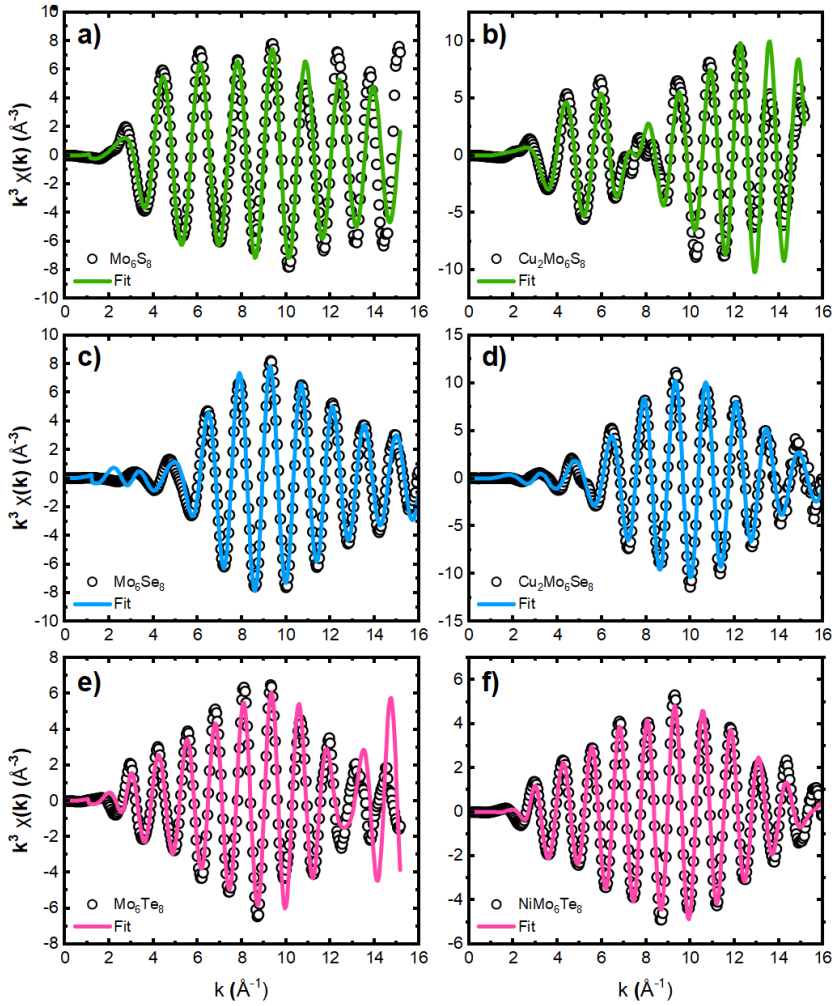


Figure S2.7. Molybdenum K-edge fits in k-space corresponding to a) Mo_6S_8, b) $Cu_2Mo_6S_8$, c) Mo_6Se_8, d) $Cu_2Mo_6S_8$, e) Mo_6Te_8, and f) $NiMo_6Te_8$.

- **Computational Details:**

We calculated the spectra and the Bader charges of Mo_6S_8 and $Cu_2Mo_6S_8$ using Kohn-Sham Density Functional Theory (DFT). Spectral calculations were carried out using the many-body X-ray absorption spectroscopy (MBXAS) formalism[15–17] which computes the transition dipole moment by approximating the final (initial) state as a Slater determinant composed of KS orbitals obtained in absence (presence) of the relevant core electron. This is accomplished with the help of a transformation matrix connecting the spectrum of orbitals from the initial and final state self-consistent fields. The final-state Slater determinant is constructed from frozen orbitals obtained using the eXcited-electron and Core-Hole (XCH) approach which essentially computes the lowest-energy neutral KS state compatible with the presence of the relevant core-hole. In our calculations, the effects of the core-hole are incorporated by employing a modified pseudopotential.

The atomic model for Mo_6S_8 was obtained from the Materials Project: mp-2164; while the structure for $Cu_2Mo_6S_8$ was calculated with DFT, as described in Ref. 18. In order to reduce the impact of spurious interactions among periodic images of the core-excited atoms, we ensure that the supercells used in our calculations have a dimension at least of 1 nm in each direction. The Perdew-Burke-Ernzerhoff (PBE) exchange-correlation functional,[19] in conjunction with ultrasoft pseudopotentials[20] was used in all calculations. In order to account for strong on-site Coulomb interactions and associated electron-localization in the d-orbitals, Hubbard U values of 4.0 eV[21] and 3.16 eV[8,22–25] were used for Cu and Mo, respectively. Plane-wave kinetic energy cut-offs of 35 and 280 Ry were found necessary for KS orbitals and charge density, respectively, to obtain converged spectra, together with first Brillouin zone sampling using a 3x3x3 k-point grid. Finally, a rigid empirical energy-shift of 2468 eV (dependent on the pseudopotential, functional, cut-offs, etc.) is added to all spectra.

The Bader charges were calculated with the Bader Charge Analysis Code[26] using the ground state charge density obtained from the spectral simulations, and recover 100% of the valence electrons. The charge in each atom is calculated as the difference between the valence charge in the pseudopotential for each element and their Bader valence charge.

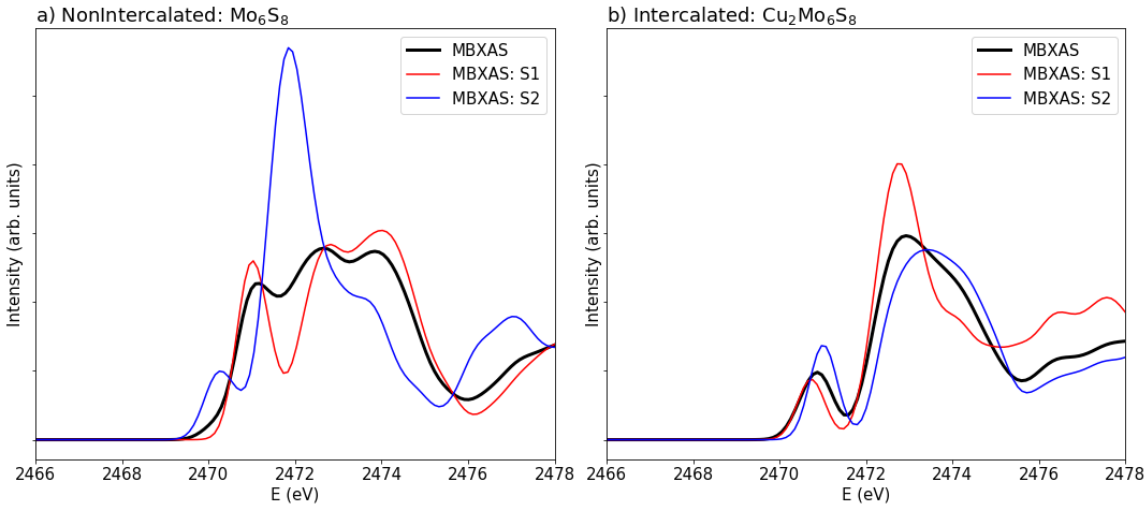


Figure S2.8. Spectra of the S_1 and S_2 atoms in Mo_6S_8 and $Cu_2Mo_6S_8$; note that the starkly different pre-edge in S_1 and S_2 spectra (red and blue, respectively) in Mo_6S_8 become more similar in $Cu_2Mo_6S_8$.

Table S2.8. Calculated Bader charges (Lowdin charges in parentheses) on Mo-tetracoordinated (S_1) and Mo-tricoordinated (S_2) sulfur atoms and Mo atoms in Mo_6S_8 and $Cu_2Mo_6S_8$.

Type	Mo_6S_8	$Cu_2Mo_6S_8$	Difference
S_1	−0.73 (0.42)	−0.75 / −0.80 (0.45 / 0.42)	−0.02 / −0.07 (0.03 / 0.00)
S_2	−0.63 (0.26)	−0.79 (0.34)	−0.16 (0.08)
Mo	0.94 (−0.41)	0.86 / 0.87 (−0.36 / −0.40)	−0.08 / −0.09 (0.05 / 0.01)

- **Effect of geometric changes and charge transfer on spectra**

Spectral differences that result from intercalation could be attributed to the presence of the intercalant, as well as the geometric changes associated with it. Here, we discuss the case of copper intercalation in the S K-edge spectra of Mo_6S_8. As mentioned in the main text, the key difference between the S K-edge spectra of the Non-Intercalated structure and the Intercalated one (Figure 2.5 in the main text) is the decrease in pre-peak intensity. Comparing the individual spectra of the four-fold and three-fold coordinated (Type 1 and 2) sulfur atoms, we see that overall pre-peak intensity decrease results from a *decrease in the pre-peak* intensity of the S_1 spectrum and an overall *blue-shift* in the S_2 spectrum (Figure S2.8).

In order to separate the effects of geometry changes and charge transfer due to presence of the intercalant in the spectra of S_1 and S_2, we have investigated the following structures:

1. Non-Intercalated Mo_6S_8;
2. Intercalated $Cu_2Mo_6S_8$;
3. Artificial intermediate: Non-Intercalated structure **1** with added copper (Mo_6S_8 +2Cu) in which only the positions of the Cu atoms have been optimized;
4. Artificial intermediate: Intercalated structure **2** with all the copper atoms removed.

It should be noted that in **3**, due to the structural constraints in this artificial series, the S2 atom is coordinated with one copper atom and not two, as in the Intercalated phase (**2**). Here, we consider a coordination cutoff of 2.7 Å. This series of structures facilitates investigating structural effects by comparing **1** and **4**, or **2** and **3**. On the other hand, charge-transfer effects can be investigated by comparing **1** and **3**; or **2** and **4**.

The atomic Bader charges for each structure are shown in Figure S2.9. The Non-Intercalated structure (**1**) and the Intercalated structure with removed Cu atoms (**4**) have a similar charge distribution, with a clear difference in charge on the S atoms, depending on their four-fold (Type 1) or three-fold (Type 2) coordination with the surrounding Mo atoms (Figure S2.9 a and c). In contrast, Type 2 sulfur atoms get reduced in the structures with copper (**2** and **3**, Figure S2.9 b and c). In the Intercalated phase, their charges become similar to those of Type 1 sulfur atoms. That is, most of the **Cu charge redistributes in the S_2 atoms** rather than in the Mo, **independently of the changes in the geometry** of the Mo_6S_8 lattice when Cu is added. When copper is removed, the charges on the sulfur atoms return to values closer to those in the Non-Intercalated structure (**4**).

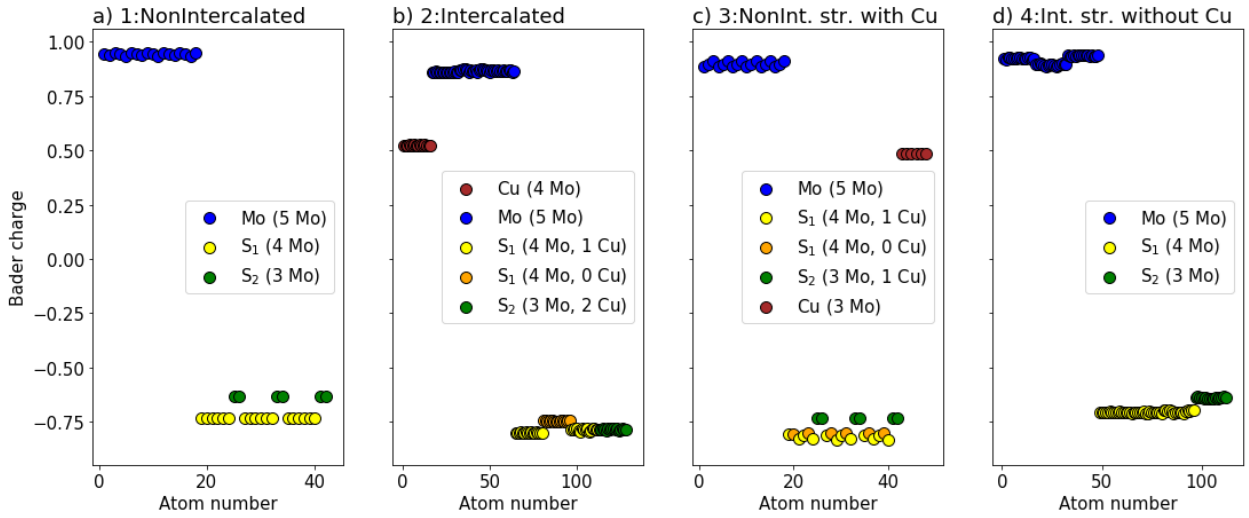


Figure S2.9. Change in Bader charge with respect to the neutral atom in structures **1-4**, colored according to the element and coordination around the given atom.

Next, we compare the spectra of structures **1-4**. Let us look separately at S_1 and S_2 spectra to understand the above-mentioned *decrease in the pre-peak* of the S_1 spectrum and an overall *blue-shift* in the S_2 spectrum.

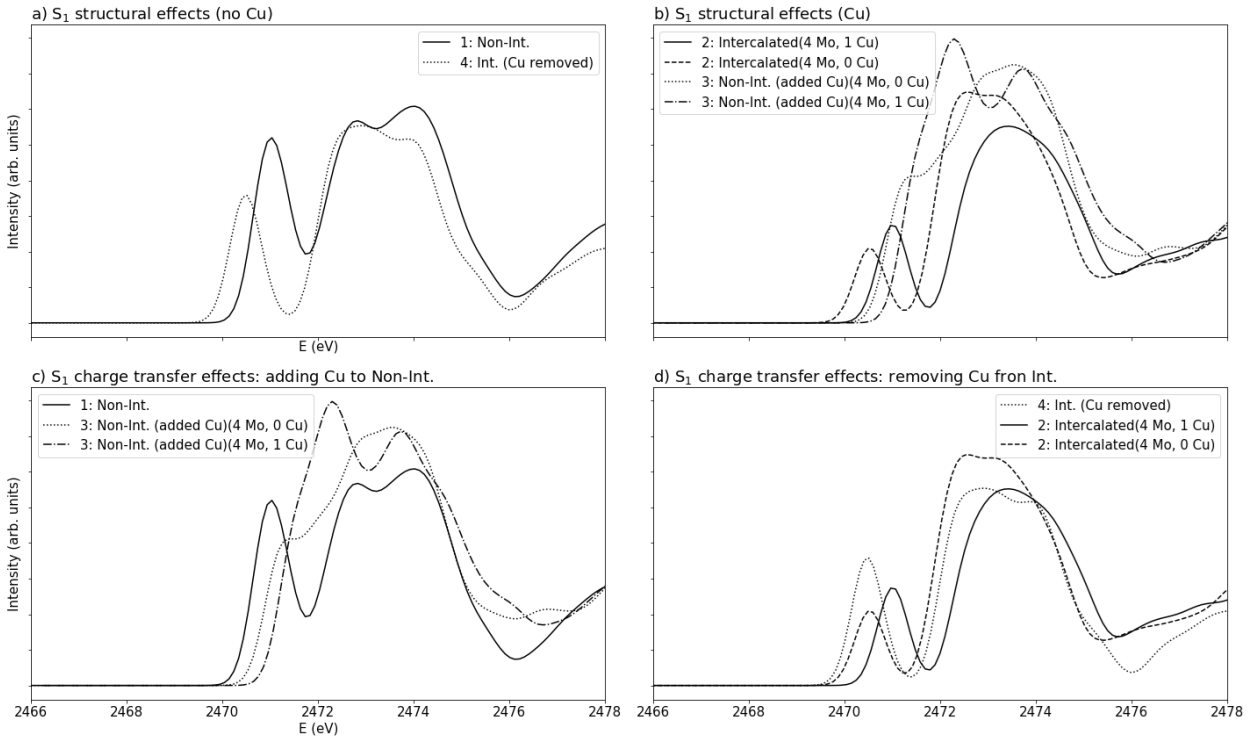


Figure S2.10. Structural and charge transfer effects in the spectra of S_1 for structures **1-4**.

In Figure S2.10, the S_1 spectra of structures **1-4** are shown in pairs to ease the comparison of the effects that result from geometry changes (a and b) and from the presence of Cu (c and d). Now, we can carry out a thought experiment of the step-wise spectral changes between **1** and **2**: starting from the Non-Intercalated phase (**1**), let us change the geometry of the Mo_6S_8 lattice to match that of the Intercalated phase (**4**). This results in a red-shift and intensity decrease of the pre-peak (Figure S2.10 a), due to the Mo-S_1 distances changing from 2.44-2.45 to 2.40, 2.45, 2.47 and 2.51 A. This is consistent with a tight-binding picture in which longer Mo-S bonds lead to red-shifted peaks due to reduced orbital repulsion. Then, we introduce the Cu atoms to produce the Intercalated phase (**2**). The pre-peak intensity decreases again, but strongly blue-shifts (Figure S2.10 d). These changes in the spectra are due to Pauli exclusion – filling of previously unoccupied orbitals that contributed to the pre-peak due to the rising the Fermi level. An alternative pathway from the same starting point (**1**) can be taken by adding Cu first to produce **3**. This leads to a blue-

shift and intensity decrease of the pre-peak (Figure S2.10c). Once **3** is "expanded" to the Intercalated phase (**2**), a slight red-shift and further intensity decrease are observed (Figure S2.10b). In conclusion, the **pre-peak intensity decrease in S_1** results from **cooperation of structural effects and electronic effects**, while they mostly cancel each other out in terms of energy shift.

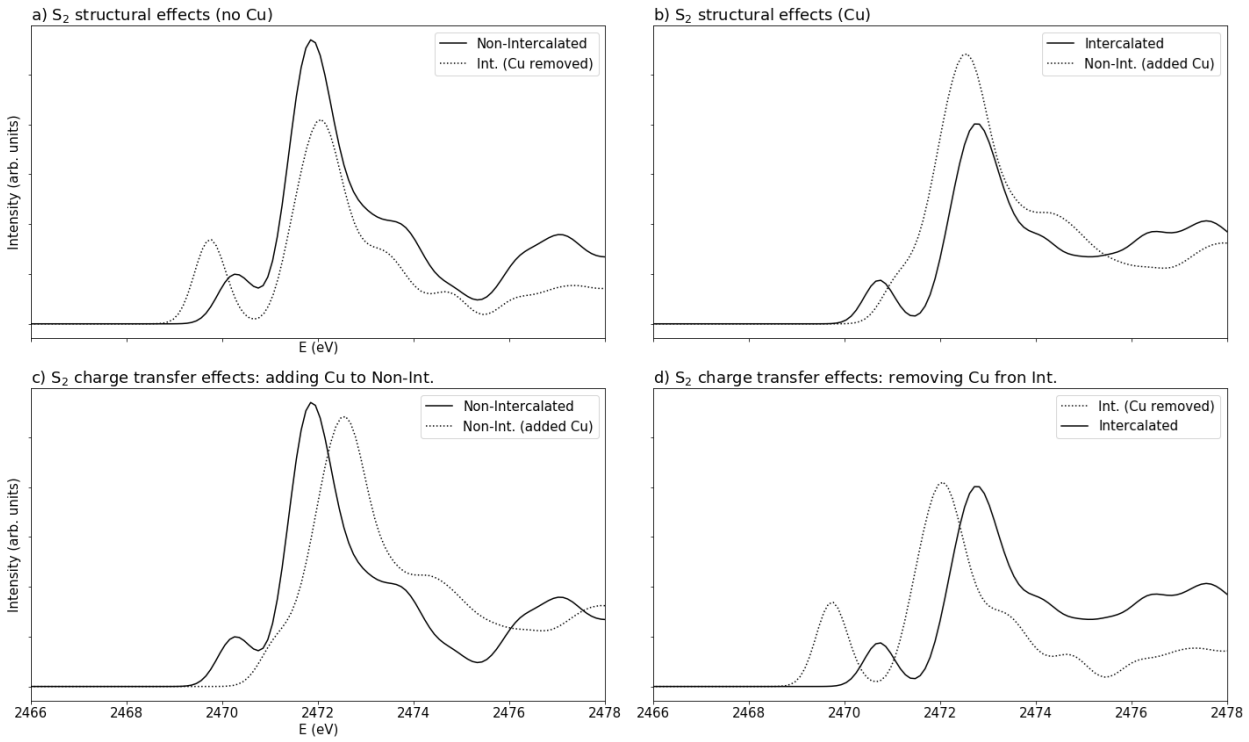


Figure S2.11. Structural and charge transfer effects in the spectra of S_2 for structures **1-4.**

A similar set of plots for the Type 2 S is shown in Figure S2.11. Let us repeat the thought experiment: this time, changing the Non-intercalated structure (**1**) to match the Intercalated Mo_6S_8 lattice (**4**) leads to red-shift and intensity increase in the pre-peak (Figure S2.11a), again due to the elongation of Mo-S_2 distances (2.43 to 2.45, 2.49, 2.51 A). Once Cu atoms are added to produce the Intercalated phase (**2**), an overall blue-shift and strong intensity decrease in the pre-peak follow (Figure S2.11c). If we take the alternative route, adding Cu to **1** first leads to an overall

blue-shift and strong intensity decrease in the pre-peak of **3** (Figure S2.11c). From here, "expanding" the geometry to match the intercalated phase **2** results in a slight red-shift of the pre-peak. Hence, for Type 2 S, pre-peak intensity results from the canceled out effects of change in geometry and charge transfer. The strongest change, that is, the overall **blue shift**, is entirely due to the **presence of the Cu**.

It is important to note here that the blue-shift in the S_2 spectra contradicts the typical expectation that the spectrum of a reduced species (with lower oxidation state) is red-shifted due to the increased screening of the core electrons provided by the extra valence electrons. The reason for this relates to the interesting electron-deficient band structure of Mo_6S_8. In Mo_6S_8, adding electrons raises the Fermi level, bringing it closer to the pseudo-gap (Figure S2.12). The downward slope in the electronic density of states (DOS) implies a decrease in the number of free carriers near the Fermi level as it rises, and, therefore, a decrease in electronic screening. This is consistent with the increases in (pseudo) band gap upon intercalation (Figure S2.12). The reduced screening will also increase the binding energy of the S 1*s* core electrons and shift the unoccupied S_2 orbitals with p character higher in energy, resulting in the blue-shift of the S_2 spectra.

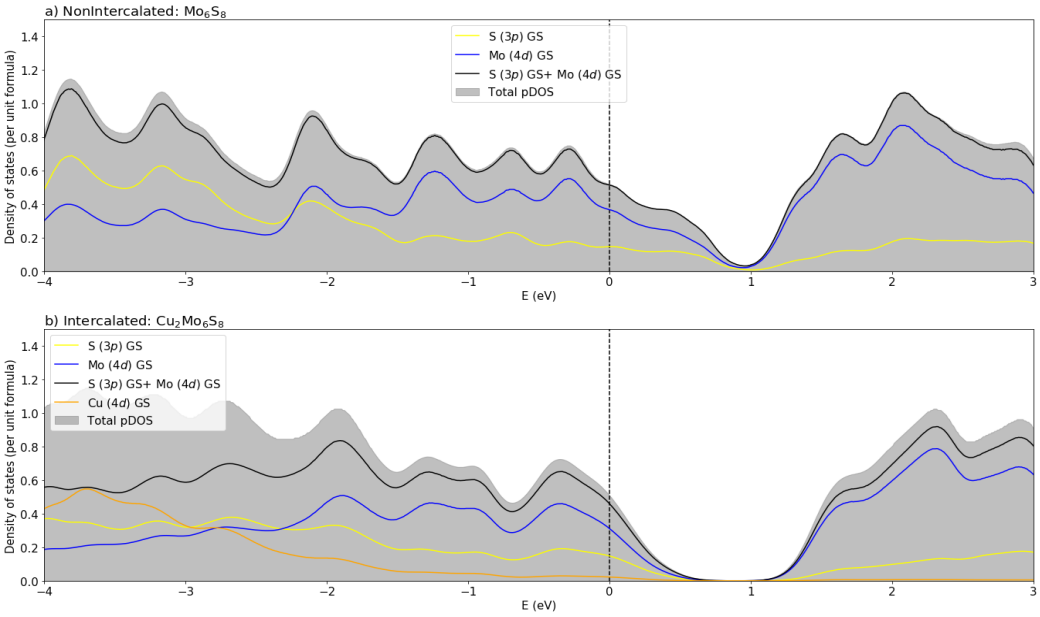


Figure S2.12. Projected density of states for the Non-Intercalated (a) and Intercalated (b) phases, aligned with reference to each's Fermi level - marked by a vertical line.

In summary, while pre-peak intensity decrease in S_1 is due to cooperative structural and charge transfer effects, the blue-shift in S_2 is solely due to charge transfer.

Atomic structures used in the calculations (POSCAR format):

Mo18 S24

1.0

9.288858 0.000000 0.000000

-4.644429 8.044387 0.000000

0.000000 0.000000 10.984105

Mo S

18 24

direct

0.016027 0.177204 0.389330 Mo

0.822796 0.838822 0.389330 Mo

0.161178 0.983973 0.389330 Mo

0.983973 0.822796 0.610670 Mo

0.177204 0.161178 0.610670 Mo

0.838822 0.016027 0.610670 Mo

0.682693 0.510538 0.722664 Mo

0.489462 0.172156 0.722664 Mo

0.827844 0.317307 0.722664 Mo

0.650640 0.156129 0.944003 Mo

0.843871 0.494511 0.944003 Mo

0.505489 0.349360 0.944003 Mo

0.349360 0.843871 0.055997 Mo

0.156129 0.505489 0.055997 Mo

0.494511 0.650640 0.055997 Mo

0.317307 0.489462 0.277336 Mo

0.510538 0.827844 0.277336 Mo

0.172156 0.682693 0.277336 Mo

0.714999 0.029741 0.418033 S

0.970259 0.685257 0.418033 S

0.314743 0.285001 0.418033 S

0.285001 0.970259 0.581967 S

0.029741 0.314743 0.581967 S

0.685257 0.714999 0.581967 S

0.000000 0.000000 0.221041 S

0.000000 0.000000 0.778959 S

0.381665 0.363075 0.751367 S

0.636925 0.018591 0.751367 S

0.981409 0.618335 0.751367 S

0.951668 0.303592 0.915300 S

0.696408 0.648076 0.915300 S

0.351924 0.048332 0.915300 S

0.666667 0.333333 0.554374 S

0.666667 0.333333 0.112292 S

0.048332 0.696408 0.084700 S

0.303592 0.351924 0.084700 S

0.648076 0.951668 0.084700 S

0.618335 0.636925 0.248633 S

0.363075 0.981409 0.248633 S

0.018591 0.381665 0.248633 S

0.333333 0.666667 0.887708 S

0.333333 0.666667 0.445626 S

Cu2 Mo6 S8

1.0

6.543083 -0.306105 -0.119756

-0.453054 6.405233 0.234909

-0.756782 -0.570508 6.479792

Cu Mo S

2 6 8

direct

0.939188 0.161709 0.905066 Cu

0.060808 0.838287 0.094920 Cu

0.219229 0.544697 0.399739 Mo

0.780776 0.455307 0.600269 Mo

0.408031 0.226173 0.543638 Mo

0.591985 0.773820 0.456356 Mo

0.534632 0.406577 0.222425 Mo

0.465370 0.593419 0.777571 Mo

0.140730 0.371154 0.715454 S

0.859255 0.628857 0.284548 S

0.715263 0.138399 0.384125 S

0.284734 0.861601 0.615879 S

0.381325 0.729891 0.122170 S

0.618678 0.270116 0.877835 S

0.190204 0.204510 0.196348 S

0.809792 0.795484 0.803656 S

References

(1) Perryman, J. T.; Hyler, F. P.; Ortiz-Rodríguez, J. C.; Mehta, A.; Kulkarni, A. R.; Velázquez, J. M. X-Ray Absorption Spectroscopy Study of the Electronic Structure and Local Coordination of 1st Row Transition Metal-Promoted Chevrel-Phase Sulfides. *Journal of Coordination Chemistry*, 2019, *72*, 1322–1335.

(2) Perryman, J. T.; Ortiz-Rodríguez, J. C.; Jude, J. W.; Hyler, F. P.; Davis, R. C.; Mehta, A.; Kulkarni, A. R.; Patridge, C. J.; Velázquez, J. M. Metal-Promoted Mo6S8 Clusters: A Platform for Probing Ensemble Effects on the Electrochemical Conversion of CO2 and CO to Methanol. *Materials Horizons*, 2020, *7*, 193–202.

(3) Ortiz-Rodríguez, J. C.; Singstock, N. R.; Perryman, J. T.; Hyler, F. P.; Jones, S. J.; Holder, A. M.; Musgrave, C. B.; Velázquez, J. M. Stabilizing Hydrogen Adsorption through Theory-Guided Chalcogen Substitution in Chevrel-Phase Mo6X8(X=S, Se, Te) Electrocatalysts. *ACS Applied Materials and Interfaces*, 2020, *12*, 35995–36003.

(4) Lancry, E.; Levi, E.; Gofer, Y.; Levi, M.; Salitra, G.; Aurbach, D. Leaching Chemistry and the Performance of the Mo6S8 Cathodes in Rechargeable Mg Batteries. *Chemistry of Materials*, 2004, *16*, 2832–2838.

(5) Morra, M. J.; Fendorf, S. E.; Brown, P. D. Speciation of Sulfur in Humic and Fulvic Acids Using X-Ray Absorption. *Geochemica et Cosmochimica Acta*, 1997, *61*, 683–688.

(6) Prietzel, J.; Botzaki, A.; Tyufekchieva, N.; Brettholle, M.; Thieme, J.; Klysubun, W. Sulfur Speciation in Soil by S K -Edge XANES Spectroscopy: Comparison of Spectral Deconvolution and Linear Combination Fitting. *Environmental Science and Technology*, 2011, *45*, 2878–2886.

(7) Gambardella, A. A.; Schmidt Patterson, C. M.; Webb, S. M.; Walton, M. S. Sulfur K-Edge XANES of Lazurite: Toward Determining the Provenance of Lapis Lazuli. *Microchemical*

Journal, 2016, *125*, 299–307.

(8) Thöle, F.; Wan, L. F.; Prendergast, D. Re-Examining the Chevrel Phase Mo6S8 Cathode for Mg Intercalation from an Electronic Structure Perspective. *Physical Chemistry Chemical Physics*, 2015, *17*, 22548–22551.

(9) Yu, P.; Long, X.; Zhang, N.; Feng, X.; Fu, J.; Zheng, S.; Ren, G.; Liu, Z.; Wang, C.; Liu, X. Charge Distribution on S and Intercluster Bond Evolution in Mo 6 S 8 during the Electrochemical Insertion of Small Cations Studied by X-Ray Absorption Spectroscopy. *Journal of Physical Chemistry Letters*, 2019, *10*, 1159–1166.

(10) Ravel, B.; Newville, M. ATHENA, ARTEMIS, HEPHAESTUS: Data Analysis for X-Ray Absorption Spectroscopy Using IFEFFIT. *Journal of Synchrotron Radiation*, 2005, *12*, 537–541.

(11) Newville, M. IFEFFIT: Interactive XAFS Analysis and FEFF Fitting. *Journal of Synchrotron Radiation*, 2001, *8*, 322–324.

(12) Roy, M.; Gurman, S. J. Amplitude Reduction in EXAFS. *Journal of Synchrotron Radiation*, 1999, *6*, 228–230.

(13) Levi, E.; Aurbach, D. Chevrel Phases, MxMo6T8 (M = Metals, T = S, Se, Te) as a Structural Chameleon: Changes in the Rhombohedral Framework and Triclinic Distortion. *Chemistry of Materials*, 2010, *22*, 3678–3692.

(14) Wan, L. F.; Wright, J.; Perdue, B. R.; Fister, T. T.; Kim, S.; Apblett, C. A.; Prendergast, D. Revealing Electronic Structure Changes in Chevrel Phase Cathodes upon Mg Insertion Using X-Ray Absorption Spectroscopy. *Physical Chemistry Chemical Physics*, 2016, *18*, 17326–17329.

(15) Liang, Y.; Vinson, J.; Pemmaraju, S.; Drisdell, W. S.; Shirley, E. L.; Prendergast, D.

Accurate X-Ray Spectral Predictions: An Advanced Self-Consistent-Field Approach Inspired by Many-Body Perturbation Theory. *Physical Review Letters*, 2017, *118*, 1–7.

(16) Liang, Y.; Prendergast, D. Quantum Many-Body Effects in x-Ray Spectra Efficiently Computed Using a Basic Graph Algorithm. *Physical Review B*, 2018, *97*, 1–25.

(17) Liang, Y.; Prendergast, D. Taming Convergence in the Determinant Approach for X-Ray Excitation Spectra. *Physical Review B*, 2019, *100*, 1–12.

(18) Singstock, N. R.; Ortiz-Rodríguez, J. C.; Perryman, J. T.; Sutton, C.; Velázquez, J. M.; Musgrave, C. B. Machine Learning Guided Synthesis of Multinary Chevrel Phase Chalcogenides. *Journal of the American Chemical Society*, 2021, *143*, 9113–9122.

(19) Perdew, J. P.; Burke, K.; Ernzerhof, M. Generalized Gradient Approximation Made Simple. *Physical Review Letters*, 1996, *77*, 3865–3868.

(20) Vanderbilt, D. Soft Self-Consistent Pseudopotentials in a Generalized Eigenvalue Formalism. *Physical Review B*, 1990, *41*, 7892–7895.

(21) Wang, L.; Maxisch, T.; Ceder, G. Oxidation Energies of Transition Metal Oxides within the GGA+U Framework. *Physical Review B - Condensed Matter and Materials Physics*, 2006, *73*, 1–6.

(22) Guguchia, Z.; Kerelsky, A.; Edelberg, D.; Banerjee, S.; Von Rohr, F.; Scullion, D.; Augustin, M.; Scully, M.; Rhodes, D. A.; Shermadini, Z.; Luetkens, H.; Shengelaya, A.; Baines, C.; Morenzoni, E.; Amato, A.; Hone, J. C.; Khasanov, R.; Billinge, S. J. L.; Santos, E.; Pasupathy, A. N.; Uemura, Y. J. Magnetism in Semiconducting Molybdenum Dichalcogenides. *Science Advances*, 2018, *4*, 1–9.

(23) Kirchner-Hall, N. E.; Zhao, W.; Xiong, Y.; Timrov, I.; Dabo, I. Extensive Benchmarking of DFT+U Calculations for Predicting Band Gaps. *Applied Sciences*, 2021, *11*.

(24) Jain, A.; Hautier, G.; Ong, S. P.; Moore, C. J.; Fischer, C. C.; Persson, K. A.; Ceder, G. Formation Enthalpies by Mixing GGA and GGA + U Calculations. *Physical Review B - Condensed Matter and Materials Physics*, 2011, *84*, 1–10.

(25) Lan, G.; Song, J.; Yang, Z. A Linear Response Approach to Determine Hubbard U and Its Application to Evaluate Properties of Y2B2O7, B = transition Metals 3d, 4d and 5d. *Journal of Alloys and Compounds*, 2018, *749*, 909–925.

(26) Henkelman, G.; Arnaldsson, A.; Jónsson, H. A Fast and Robust Algorithm for Bader Decomposition of Charge Density. *Computational Materials Science*, 2006, *36*, 354–360.

3. Chapter 3

$Ln_{10}S_{14}O$ (Ln = La, Pr, Nd, Sm) Oxysulfides: A Series of Direct n-Type Semiconductors

Abstract

Lanthanoid oxysulfides are promising materials for technological applications owing to their magnetic, photoluminescent, catalytic, and optoelectronic properties. Herein, we report the solid-state synthesis and structural characterization of $Ln_{10}S_{14}O$ (Ln = La, Ce, Pr, Nd, Sm) oxysulfides. Then, we present a thorough discussion on their electronic and photophysical properties. Through Tauc plot analysis and the derivation of the absorption spectrum fitting method (DASF), we determine that all oxysulfides have direct band gaps with energies of 2.84 eV (La), 2.02 eV (Ce), 2.56 eV (Pr), 2.64 eV (Nd), and 2.41 eV (Sm). Furthermore, surface photovoltage spectroscopy (SPS) shows photovoltage (ΔCPD) values of −0.4 to −1.1 V for La-, Pr-, Nd-, and Sm-containing compounds when illuminated near the optical band gap, indicating that these oxysulfides are n-type semiconductors, which is consistent with Mott–Schottky analysis. Photovoltages under sub-band gap illumination energy and photovoltage decay data suggest mid-band gap states possibly arising from the lanthanoid 4f orbitals and/or defects within the crystal structure or at the particle surfaces. These photophysical properties suggest possible applications of the oxysulfides in photoelectrochemical and photovoltaic energy conversion.

Introduction

The not-so-rare earths, i.e., lanthanoids,[1] impart numerous electronic, magnetic, and optical properties to the compounds they form owing to their multiplicity of electronic energy levels, the presence of 4f orbitals, and high spin–orbit coupling.[2,3] In the solid state, lanthanoid oxides have been the most widely studied materials, given their ease of synthesis, and industrial uses as

supports for methane reforming,[4] thermochemical fuel production,[5] and photocatalysis.[6] Sulfur substitution results in the narrowing of their band gaps to the visible region of the electromagnetic spectrum, relevant to applications as thermoelectrics,[7] in solar energy conversion,[8] and as nontoxic pigments.[9,10] Nevertheless, the band structure and optical absorption behavior of lanthanoid (oxy)sulfides are not yet well understood. Initially misidentified as a lanthanoid sesquisulfide polymorph, β-Ln_2S_3, $Ln_{10}S_{14}O$ represents a distinct tetragonal phase in which the oxygen atoms occupy the center of Ln(III) tetrahedra, surrounded by an intricate system of lanthanoid sulfide.[11] In comparison to the oxysulfides of formula Ln_2O_2S, which have been studied for their optical properties as phosphors,[12] imaging agents,[13] and sulfur-tolerant catalysts,[14,15] comparatively less information is known of their higher sulfur content congeners, $Ln_{10}S_{14}O$.[16−20] Having narrower band gaps as a result of the presence of quasi-stoichiometric sulfur, these oxysulfides have shown interesting photoluminescence[16] and light absorption properties in catalytic systems.[17] However, much is yet unknown about their electronic structure, band gap energy, majority carrier type, and charge dynamics under illumination factors relevant to optoelectronic applications of these compounds.

In this work, we study the structural and photophysical properties of $Ln_{10}S_{14}O$ for the early lanthanoid ions La, Ce, Pr, Nd, and Sm. Specifically, diffuse reflectance UV−vis spectroscopy demonstrates that all oxysulfides possess band gap energies in the visible region of the electromagnetic spectrum. Moreover, through Tauc and derivation of the absorption spectrum fitting (DASF) analysis, it can be determined for the first time that the nature of the transition is direct. Finally, surface photovoltage spectroscopy (SPS) and Mott−Schottky plots show electrons to be the majority carriers in $La_{10}S_{14}O$, $Pr1_0S_{14}O$, $Nd_{10}S_{14}O$, and $Sm_{10}S_{14}O$, allowing classification of these light absorbers as n-type semiconductors. Significant surface photovoltage generation under sub-band gap energy illumination suggests that defect states may be present in these compounds in addition to the participation of the Ln 4f electrons. To the best of our knowledge,

this work presents the first comprehensive study of the electronic and photophysical properties of these lanthanoid oxysulfides.

Results and Discussion

Crystal Structure

Powder X-ray diffractograms of the series of light lanthanoid oxysulfides are presented in Figure 3.1c. In a clear demonstration of the lanthanide contraction, a progressive shift to higher 2θ (or smaller d-spacing) of the characteristic reflections from their tetragonal unit cell ($I41/acd$ space group) can be observed with the increase in the atomic number. Following this trend, both the a and c lattice parameters show a decrease, as well as the anomalous c/a increase, in agreement with previous reports (Table S3.3.1).[11,19,20] From the Rietveld refinements (Figure S3.1), the presence of secondary impurity phases can be identified. Such low levels of sulfide and oxysulfide phases tend to be present owing to the small region of stability known for the $Ln_{10}S_{14}O$ β structure in the Ln–O–S compositional phase diagram.[21] Specifically, the $Ln_{10}S_{14}O_xS_{1-x}$ structure destabilizes compared to Ln_2O_2S at high O contents.

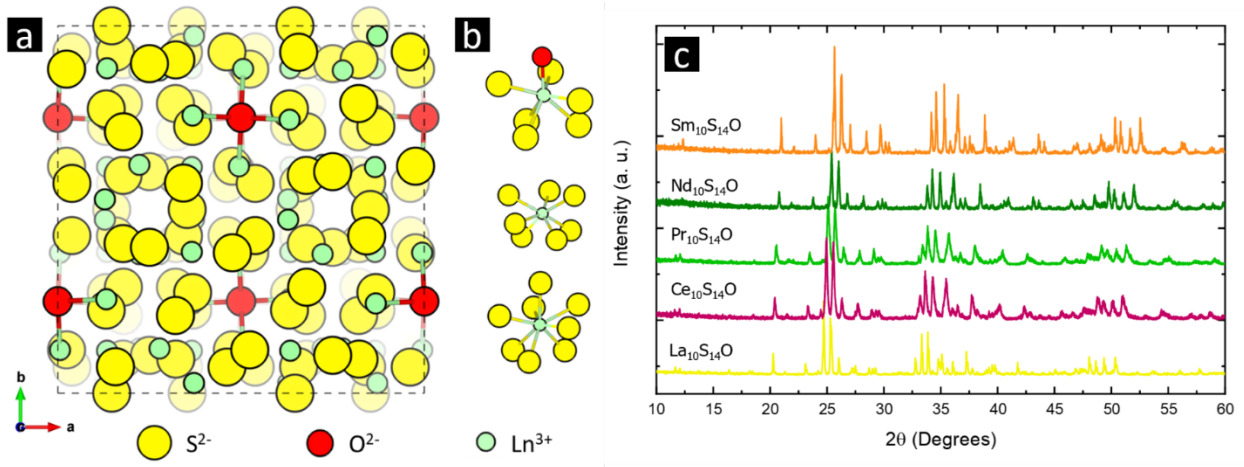


Figure 3.1. (a) Unit cell of $Ln_{10}S_{14}O$ oxysulfides viewed along the c axis, represented using the corresponding ionic radii in which the yellow, red, and green circles represent S^{2-}, O^{2-}, and Ln^{3+}. (b) Structures highlighting the multiple 7- and 8-fold coordination environments surrounding the Ln(III) ions. (c) Powder X-ray diffractograms of the corresponding lanthanoid oxysulfides.

The $Ln_{10}S_{14}O$ unit cell is shown in Figure 3.1a,b. Therein, Ln^{3+} ions occupy three distinct crystallographic sites: two sites of Wyckoff positions 32g and one 16f, exhibiting 7- and 8-fold coordination environments; the S^{2-} anions, sites 32g and 16e; and the O^{2-} the Wyckoff position 8a, in a tetrahedral configuration. Consistent with the crystal structure, Ln L_3-edge EXAFS results demonstrated a first coordination shell surrounding the Ln absorbers dominated by S^{2-} scatterers (Figure 3.2).

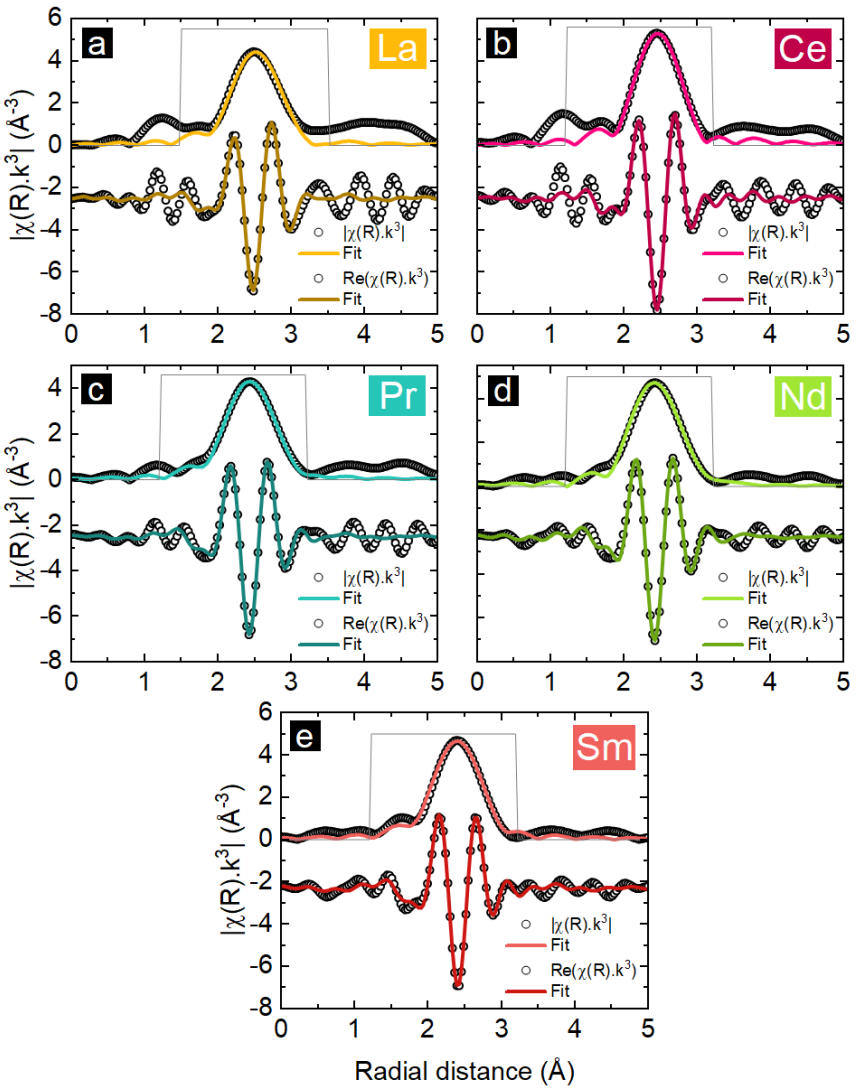


Figure 3.2. Non-phase-corrected lanthanoid L_3-edge FT-EXAFS fits for (a) $La_{10}S_{14}O$, (b) $Ce_{10}S_{14}O$, (c) $Pr_{10}S_{14}O$, (d) $Nd_{10}S_{14}O$, and (e) $Sm_{10}S_{14}O$. The top trace represents the magnitude of $\chi(R) \cdot k^3$, whereas the bottom constitutes its real component.

At first, the lack of contribution of Ln–O scattering paths to the nearest-neighbors seemed peculiar, given its close distance (ca. 2.4 Å) in the coordination environment of the lanthanoid ions occupying one of the two 32g crystallographic sites. However, O^{2-} is only present in the immediacy of a single lanthanoid ion site and merely represents 1/7th of its neighboring ions. Thus, in the averaged data obtained for each sample, its contribution is significantly lower in

comparison to that of the S^{2-} anions. EXAFS analysis shows good agreement with crystallographic data and highlights the variety of Ln–S distances present surrounding each distinct lanthanoid crystallographic site (Tables S3.2 and S3.3) with a range of 2.919–3.027 Å for La, 2.839–2.967 Å for Ce, 2.838–2.983 Å for Pr, 2.746–3.053 Å for Nd, and 2.698–2.925 Å for Sm. Both Ln(III) ions occupying 32g sites, Ln1 and Ln2 (Figure S3.3), possess multiple nondegenerate S single scattering paths amounting to coordination numbers of 7, while the Ln(III) in 16f sites, Ln3, are characterized by multiple degenerate single scattering paths totaling an 8-fold coordination environment, which is more regular compared to the Ln1 and Ln2 sites. Considering a weighted average from the crystallographic data, the number of S atoms surrounding the lanthanoids corresponds to 6.8, which is consistent with the coordination number of 7 derived from the EXAFS fit. Interestingly, both Ln1 and Ln2 possess nearby second shell S^{2-} ions (ca. ~3.4 Å) that contribute to the scattering signal observed. Further structural information on these oxysulfides can be extracted through Raman spectroscopy. This technique is particularly useful given that in addition to band wavenumber position, the line shapes can inform on the degree of electronic or structural disorder.[22] As seen in Figure S3.4a, the spectra for all lanthanoids show narrow bands indicative of an ordered structure amounting to fewer than 10 of the 93 predicted active modes for the point group D_{4h}.[21] In principle, an increase in the ionic radius would be expected to lead to a decrease in the wavenumber, due to longer bonds and smaller force constants, as observed in some Ln_2S_3 polymorphs.[23] This is the case for the vibrations in the range of 90–130 cm^{-1}. However, there is also the presence of bands that decrease their Raman shift with higher atomic number (ca. 82 and 140 cm^{-1}, Figure S3.4b). It is likely that the combination of increasing atomic weight and ionic character in going from La(III) to Sm(III) plays a role in the observed decrease of wavenumber.

Electronic Structure

The background-subtracted and normalized L_3-edge X-ray absorption spectroscopy (XAS) spectra for all lanthanoids studied are provided in Figure S3.6. These transitions correspond to the dipole-allowed excitation of an electron from a core $2p_{3/2}$ orbital to empty states of 5d character (i.e., $2p^6 4f^q 5d^0 \rightarrow 2p^5 4f^q 5d^1$, where q corresponds to the number of f electrons in the ground state). Such spectra exhibit a characteristic sharp absorption. All Ln L_3-edge energies are consistent with previous reports.[24,25] Furthermore, the absence of multipeak white line features, caused by multiconfigurational ground states,[3] indicates the absence of the Ln(IV) oxidation state in oxysulfides.[25–27] Due to the $2p_{3/2}$ core–hole lifetime broadening, pre-edge features corresponding to the quadrupole transitions, 2p → 4f, were not detected in our XANES spectroscopy experiments and would require higher-resolution detection methods for their study.[27]

Nevertheless, insight from the interaction of Ln 4f orbitals with those from the ligands can be gained from Ln 3d X-ray photoelectron spectroscopy (XPS) signals. As a result of spin– orbit coupling, emitted 3d photoelectrons show two distinctive binding energy (BE) regions: $3d_{5/2}$ at a lower binding energy and $3d_{3/2}$ at a higher binding energy. Interestingly, all lanthanoids show an additional satellite signal of appreciable intensity. This has been attributed to the charge transfer from ligand valence orbitals to the core-ionized lanthanoid 4f.[28,29] In $La_{10}S_{14}O$, the higher binding energy peaks in both $3d_{5/2}$ and $3d_{3/2}$ regions correspond to the electron transfer satellite (Figure 3.3a). Unique to this close shell system (La^{3+}), the satellite-to-3d signal ratio is greater than unity ($R_{sat}/3d = 1.33$). In the oxysulfide crystal structure, the coordination environment of the lanthanoid ions is dominated by S^{2-} anions; thus, this value is consistent with comparable soft ligands reported by Berthou and Jorgensen.[30] Conversely, in all of the remaining lanthanoids (Ce, Pr, Nd, and Sm), the charge transfer satellites appear at lower binding energies than the corresponding 3d signals (Figure 3.3b–e). This observation has been ascribed to an increase in stability of Ln^{3+} ($3d^9 4f^{q+1}$, after ligand charge transfer) relative to Ln^{4+} ($3d^9 4f^q$).[31] Consequently,

R_{sat}/3d decreases with the increase in the effective nuclear charge along the period (Figure 3.3f), consistent with a decrease in the bond covalent character between the harder Ln^{3+} and the soft S^{2-} ligand.[30,31] Importantly, the interpretation of the spectra for lanthanoids with multiple 4f electrons demands careful attention given the potential superposition of $3d^94f^q$ configurations with those corresponding to electron transfer final states $3d^94f^{q+1}$. An expression of this multiplicity of states can be seen as the high binding energy $3d_{3/2}$ shoulders observed for $Ce_{10}S_{14}O$, $Pr_{10}S_{14}O$, $Nd_{10}S_{14}O$, and $Sm_{10}S_{14}O$.

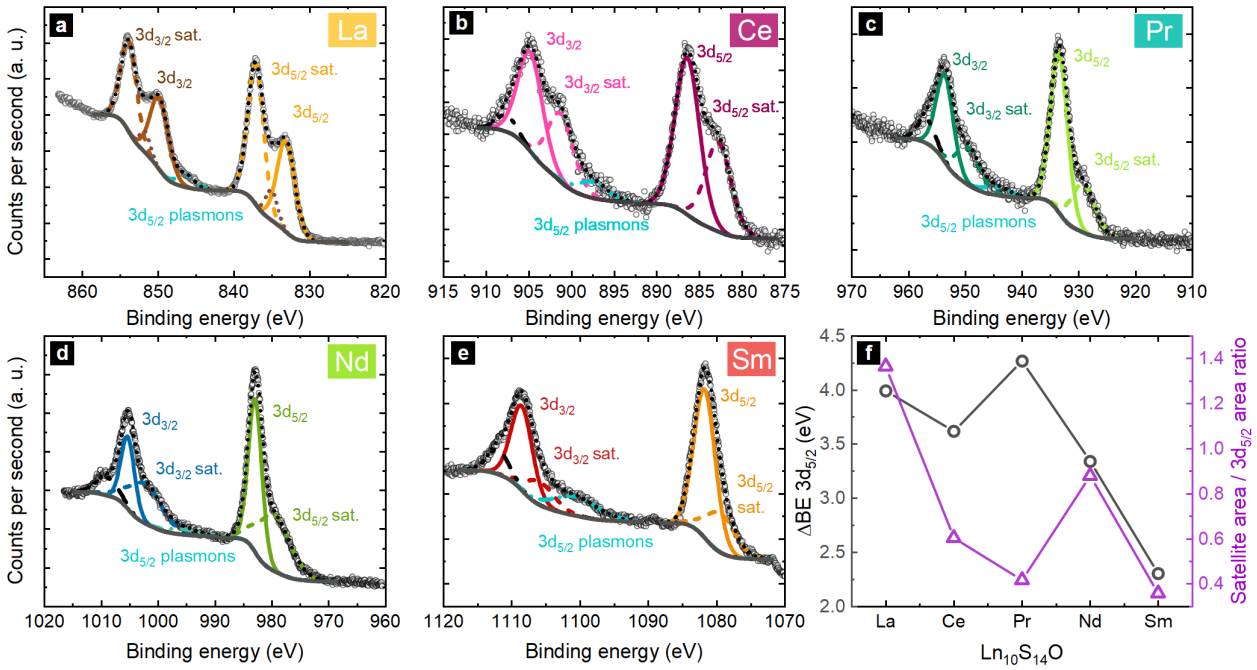


Figure 3.3. X-ray photoelectron spectroscopy of the Ln 3d region for (a) $La_{10}S_{14}O$, (b) $Ce_{10}S_{14}O$, (c) $Pr_{10}S_{14}O$, (d) $Nd_{10}S_{14}O$, and (e) $Sm_{10}S_{14}O$. (f) Comparison between the binding energy difference and area ratio of the satellite-to-$3d_{5/2}$ signal as a function of the lanthanoid ion.

Band Gap Determination

All $Ln_{10}S_{14}O$ display band gaps in the visible region of the electromagnetic spectrum as seen with the naked eye (Figure 3.4a). Upon sulfurization of the oxide precursors, the valence band becomes predominantly of S character, with its higher lying 3p orbitals, leading to narrower band gaps.[17] Diffuse reflectance UV–vis spectroscopy was used to probe the size (E_g), as well as the type of band gap present, and the results are displayed in Figure 3.4. There is no direct monotonic trend in the E_g across the lanthanoid oxysulfide series. That is, Ce demonstrates a much narrower band gap than its predecessor, La; and Nd exhibits a wider band gap than Pr.

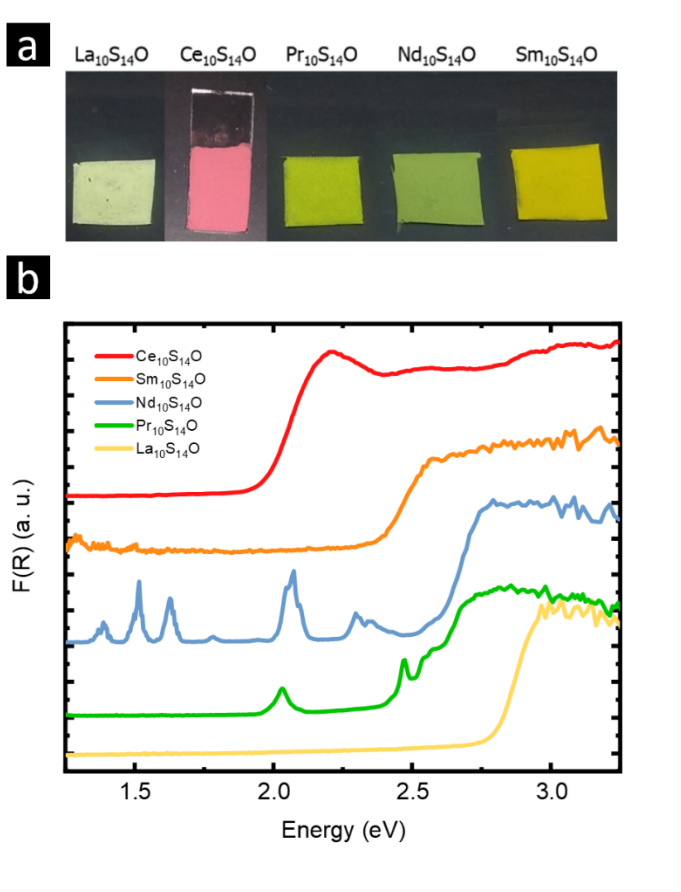


Figure 3.4. (a) Digital photographs of lanthanoid oxysulfide films on ITO substrates, and their (b) diffuse reflectance UV–vis spectra (shown offset for clarity). $F(R)$ is proportional to the absorption coefficient. $F(R) = 2R/(1-R)^2$ (Kubelka–Munk function).

In addition, Ln(III) f–f transitions are notable for Pr, Nd, and Sm. These are narrow absorption signals, which are largely unaffected by the chemical environment[2] but represent an additional challenge in the analysis of band gap type (*vide infra*) due to their overlap with the absorption edge. The most widely used method for the determination of semiconductor band gaps is the Tauc plot analysis.[32] This is based on the assumption that the absorption coefficient can be expressed as

$$(\alpha \cdot h\nu) = B(h\nu - E_g)^n \tag{3.1}$$

where h is the Planck constant, υ is the photon frequency, Eg is the band gap energy, B is a constant, and n represents the nature of the transition. That is, n = 2 for an indirect band gap, whereas n = 1/2 for a direct transition. In diffuse reflectance measurements, the absorption coefficient α is approximated by the Kubelka–Munk function, F(R).[33] By plotting $[F(R) \cdot h\upsilon]^{1/n}$ vs energy and extrapolating the linear absorption onset region to the abscissa, the band gap energy, E_g, can be estimated. The use of the Tauc method inherently requires information on the nature of the transition, or an assumption of it *a priori*. Furthermore, it has been shown that its application to semiconductors with intraband gap absorption (caused by defects, doping, or surface/bulk modifications) can lead to inaccurate *E*g estimations.[34] Thus, to aid in the distinction of the type of band gap, an orthogonal method for the analysis of reflectance spectra, known as the derivation of absorption spectrum fitting method (DASF),[35] was used. Through the calculation of the derivative of $\ln[F(R)/\lambda]$ with respect to $1/\lambda$, eq. 3.2 is obtained.

$$\frac{d\left\{ln\left[\frac{F(R)}{\lambda}\right]\right\}}{d\left(\frac{1}{\lambda}\right)} = \frac{n}{\left(\frac{1}{\lambda}-\frac{1}{\lambda_g}\right)} \tag{3.2}$$

Plotting the left side of eq. 3.2 vs $1/\lambda$, the energy associated with the band gap can be determined from the peak maxima. The application of this method was especially important for the $Ln_{10}S_{14}O$ oxysulfides studied given that both the indirect and direct band gap energies derived from Tauc analysis yield physically plausible values as shown in Table 3.1 and Figure 3.6.

DASF and Tauc results show good agreement with a direct band gap for all oxysulfides. $La_{10}S_{14}O$, $Ce_{10}S_{14}O$, and $Sm_{10}S_{14}O$, exhibit sharp absorption onsets, leading to unequivocal DASF analysis (Figure 3.5c,f,o). On the other hand, both $Pr_{10}S_{14}O$ and $Nd_{10}S_{14}O$ spectra present a more challenging scenario due to the overlap with f–f transitions. In the $Pr_{10}S_{14}O$ spectrum, three absorption bands corresponding to the excitations from the ground state $^3H_4$ to the excited states $^3P_2$ (2.57 eV, 482 nm), $^3P_1$ (2.54 eV, 488 nm), and $^3P_0$ (2.47 eV, 501 nm) can be clearly detected over the band gap absorption edge.[36] Thus, the region used for the Tauc plot analyses corresponded to $E > 2.57$ eV (Figures 3.5g,h and 3.6).

Table 3.1. Band Gap Energies Obtained through Tauc and DASF Analysis and from SPS

	Band gap (eV)			
Material	**Tauc Indirect**	**Tauc Direct**	**DASF**	**SPS**
$La_{10}S_{14}O$	2.71 ± 0.05	2.84 ± 0.05	2.839 ± 0.002	2.507
$Ce_{10}S_{14}O$	1.88 ± 0.02	2.02 ± 0.02	1.996 ± 0.001	-
$Pr_{10}S_{14}O$	2.36 ± 0.14	2.56 ± 0.11	2.566 ± 0.002	2.372
$Nd_{10}S_{14}O$	2.51 ± 0.08	2.64 ± 0.17	2.641 ± 0.003	2.424
$Sm_{10}S_{14}O$	2.23 ± 0.04	2.41 ± 0.04	2.442 ± 0.004	2.189

The convolution of the f–f transitions with the band gap energy is further translated into the DASF analysis. Instead of a single peak, multiple maxima are present (Figure 3.5i,l). While this can certainly limit the value of this method, by increasing the user input in the process, if a judicious and consistent criterion is applied, we believe that useful information can be obtained and contrasted with that gained through the Tauc method. In our DASF analysis, we consider the highest energy maxima to be the band gap energies. Similar to the overlap observed in $Pr_{10}S_{14}O$, the $Nd_{10}S_{14}O$ reflectance spectrum shows a small shoulder, or Urbach tail, ca. 2.58 eV, which is

likely caused by two f–f transitions: $^4I_{9/2} \rightarrow {}^4G_{11/2}$ (2.58 eV, 479.9 nm) and $^4I_{9/2} \rightarrow {}^2D_{3/2}$ (2.56 eV, 483.9 nm).[36] Photophysical Characterization. To probe the ability of the materials to generate mobile charge carriers under illumination, surface photovoltage spectroscopy (SPS) was employed. In SPS, a semitransparent vibrating Kelvin probe is used for the measurement of photoinduced charge transfer in particle films upon exposure to light of variable wavelength.[37,38] The spectra of the particle films on fluorine doped tin oxide (FTO) are presented in Figure S3.8 and are plotted alongside the optical absorption spectra in Figure 3.7. La, Pr, Nd, and Sm oxysulfides exhibit negative photovoltage (ΔCPD), indicating the transfer of electrons away from the Kelvin probe and toward the FTO substrate. This confirms electrons as majority carriers and identifies the compounds as n-type semiconductors. This also agrees with the Mott–Schottky analysis of the semiconductor films in 0.1 M Na2SO4 (Figure S3.11). The photovoltage spectra resemble the optical spectra in that the major photovoltage signal occurs near the optical band gaps of the materials. This photovoltage is due to the separation of photogenerated charge carriers in the valence and conduction bands as shown in Figure 3.8c. As Table 3.1 shows, the effective band gaps from the spectra compare reasonably well with the direct band gaps from the DASF analysis.

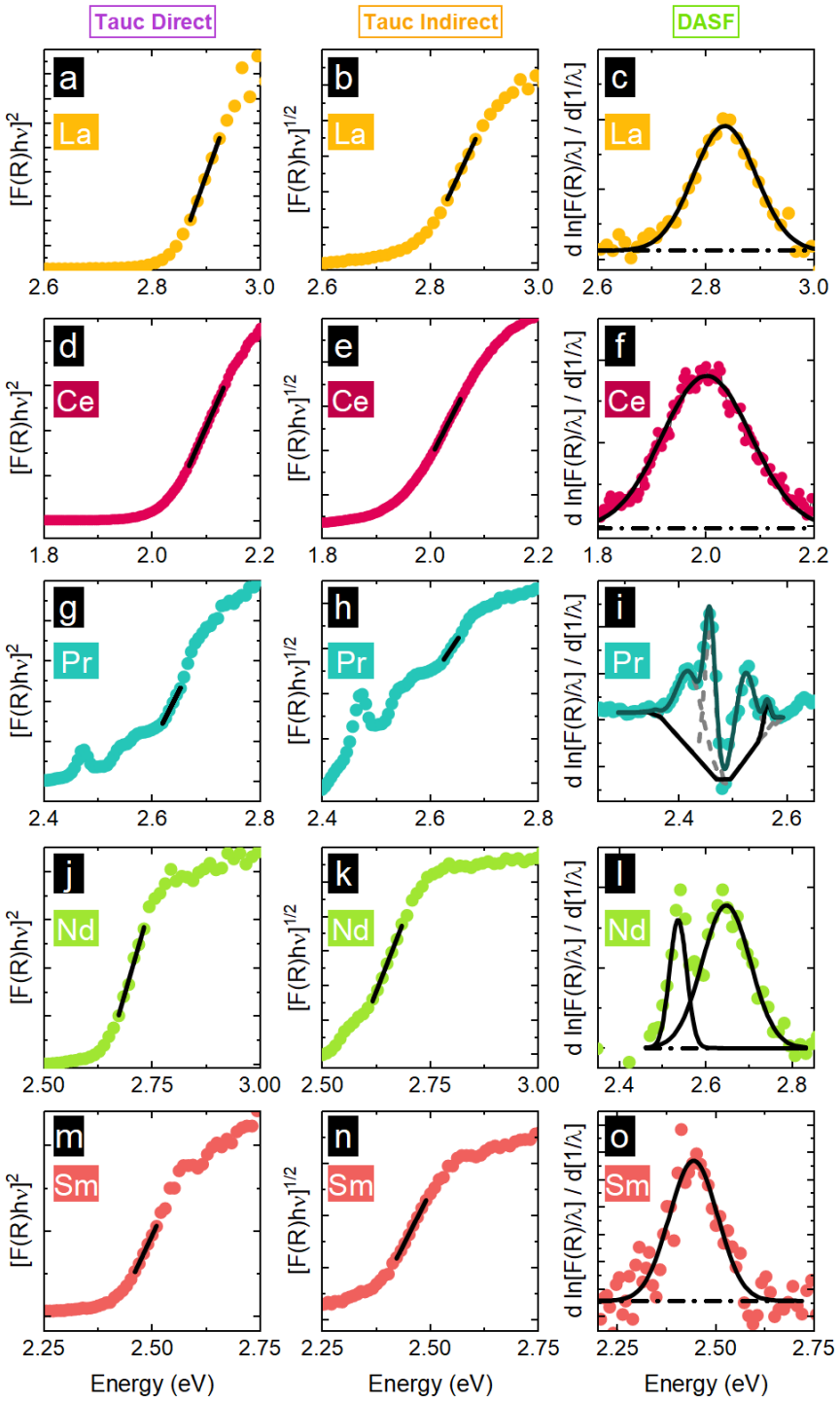


Figure 3.5. Comparison between Tauc direct, indirect, and DASF analyses for the determination of the optical band gap. The solid and dashed black lines represent linear regressions for Tauc analyses (left and middle columns) and Gaussian peak fittings for DASF analysis (right column).

Additionally, all SPS spectra contain strong photovoltage signals at photon energies below the band gap. This is attributed to excitation and transfer of charge carriers in sub-band gap states (Figure 3.8c). Sub-band gap photovoltage signals from lattice defects are commonly found in SPS data due to the high sensitivity of the technique.[39–41] In chalcogenides, defects arise from cation vacancies, antisites, and chalcogen vacancies.[42–44] In oxysulfides, the defects are most likely sulfur vacancies that are caused by post-synthetic surface oxidation. Alternatively, it is possible that defect states are generated by cation disorder,[43] induced by the high heating and cooling rates (44 °C/min and 50 °C/min, respectively) during preparation. Lastly, lanthanoid 4f orbitals in conjunction with oxygen vacancies may create mid-band gap donor states.[45] This would explain the comparatively weaker "pre-edge" photovoltage observed for $La_{10}S_{14}O$, which is lacking 4f electrons. In this case, any sub-band gap photovoltage would have to arise from antisite defects or anion vacancies. Impurities may also play a role in the observed sub-band gap photovoltage; however, the Ln_2O_2S impurity seen in Figure S3.1 possesses wider band gaps than the $Ln_{10}S_{14}O$ phases.[46]

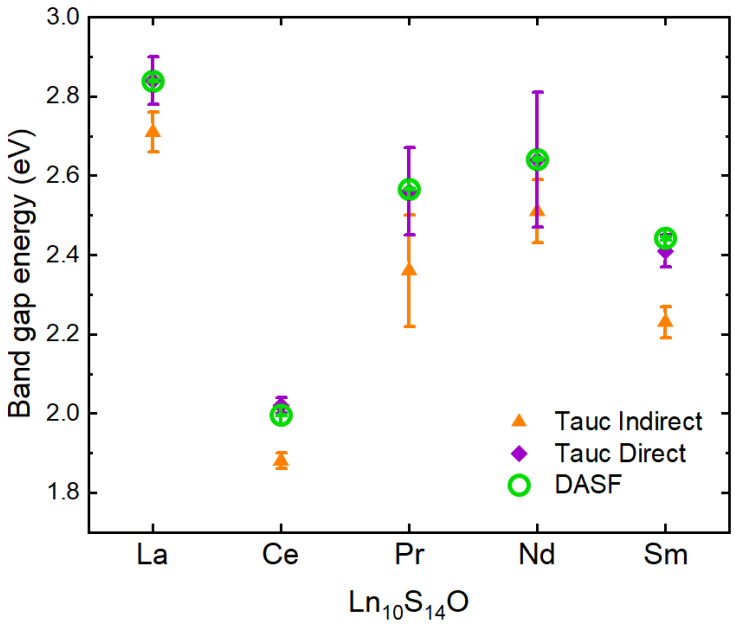


Figure 3.6. Comparison of band gap energy values obtained through Tauc plot and DASF analysis.

To further characterize the photophysical properties of lanthanoid oxysulfides, surface photovoltage decay data following 400 nm (12.5 mW $cm^{-2)}$ illumination was recorded (Figure 3.8a). This provides information about the dynamics of charge carrier separation and recombination.[47–49] For all tested oxysulfides, photovoltage signals form on the 10–20 s timescale (Figure 3.8a), reaching a final value comparable to that seen in the spectra in Figure 3.7. When the light is switched off, the photovoltage decays asymptotically but does not quite reach zero over the duration of the experiment. $La_{10}S_{14}O$ and $Sm_{10}S_{14}O$ exhibit faster relaxation dynamics, with only 5.37 and 8.07% of the ΔCPD_{max} remaining after 27 min in the dark, while $Pr_{10}S_{14}O$ and $Nd_{10}S_{14}O$ retain 19.0 and 26.2% of their ΔCPD_{max} values (Table S3.5). The long timescale of the photovoltage decay suggests that recombination occurs by a thermally activated process. Here, electrons need to overcome an energy barrier before they can combine with a trapped photohole at the semiconductor surface. Peter et al. previously used the exponential function (eq. 3.3) to model transient recombination photocurrents in photoelectrodes.[50,51] The model assumes that majority carrier transfer into surface states is limited by a potential barrier at the photoelectrode surface as shown in Figure 3.8d.[52] By plotting $\ln[\Delta CPD(t)/\Delta CPD(t = 0)]$ versus time (eq. 3.4), the lifetime τ of the trapped minority carriers can be obtained from the slope of the linear graph.

$$\frac{\Delta CPD(t)}{\Delta CPD(t=0)} = e^{-\frac{t}{\tau}} \tag{3.3}$$

$$\ln\left[\frac{\Delta CPD}{\Delta CPD(t=0)}\right] = -\frac{t}{\tau} \tag{3.4}$$

From Figure 3.8b, it can be seen that this model captures the recombination kinetics of the $Ln_{10}S_{14}O$ phases at long times (t > 800 s) based on the linearity of the plots. This suggests that carrier recombination in $Ln_{10}S_{14}O$ films is indeed limited by processes at the particle surfaces. At shorter times, additional, faster recombination pathways are active, possibly involving the mid-band gap states discussed above. Based on the linear fits in Figure 3.8b, minority carrier lifetimes in surface states range from 934.6 s ($La_{10}S_{14}O$) to 4098 s ($Nd_{10}S_{14}O$) with the remaining two phases

having intermediate τ values (Table S3.6 and Figure S3.10). This variation in times may be due to differences in surface states across the series, differences in specific surface areas, or differences in Fermi energies. We hope to gain further insight into these parameters in future investigations.

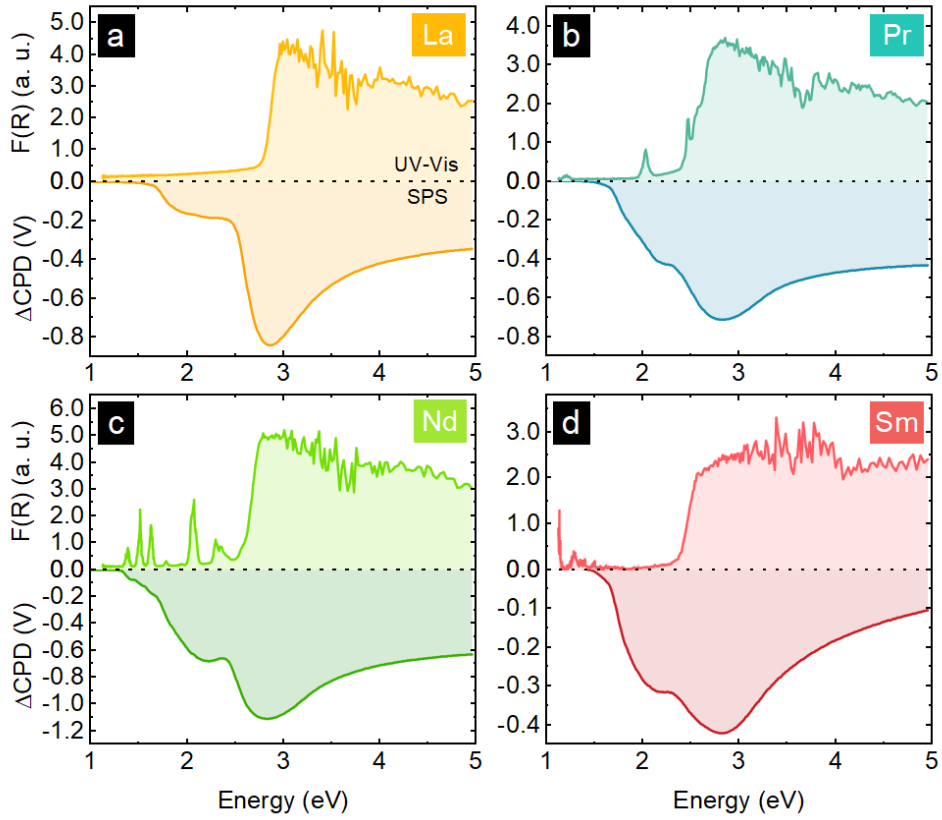


Figure 3.7. Comparison between DR UV–vis (top) and surface photovoltage spectra (bottom) of (a) $La_{10}S_{14}O$, (b) $Pr_{10}S_{14}O$, (c) $Nd_{10}S_{14}O$, and (d) $Sm_{10}S_{14}O$ films on fluorine-doped tin oxide (FTO)-coated glass slides in vacuum. ΔCPD is the contact potential difference versus the dark CPD value. For details, see the Experimental Section. Films of $Ce_{10}S_{14}O$ did not produce any photovoltage signal (Figure S3.9).

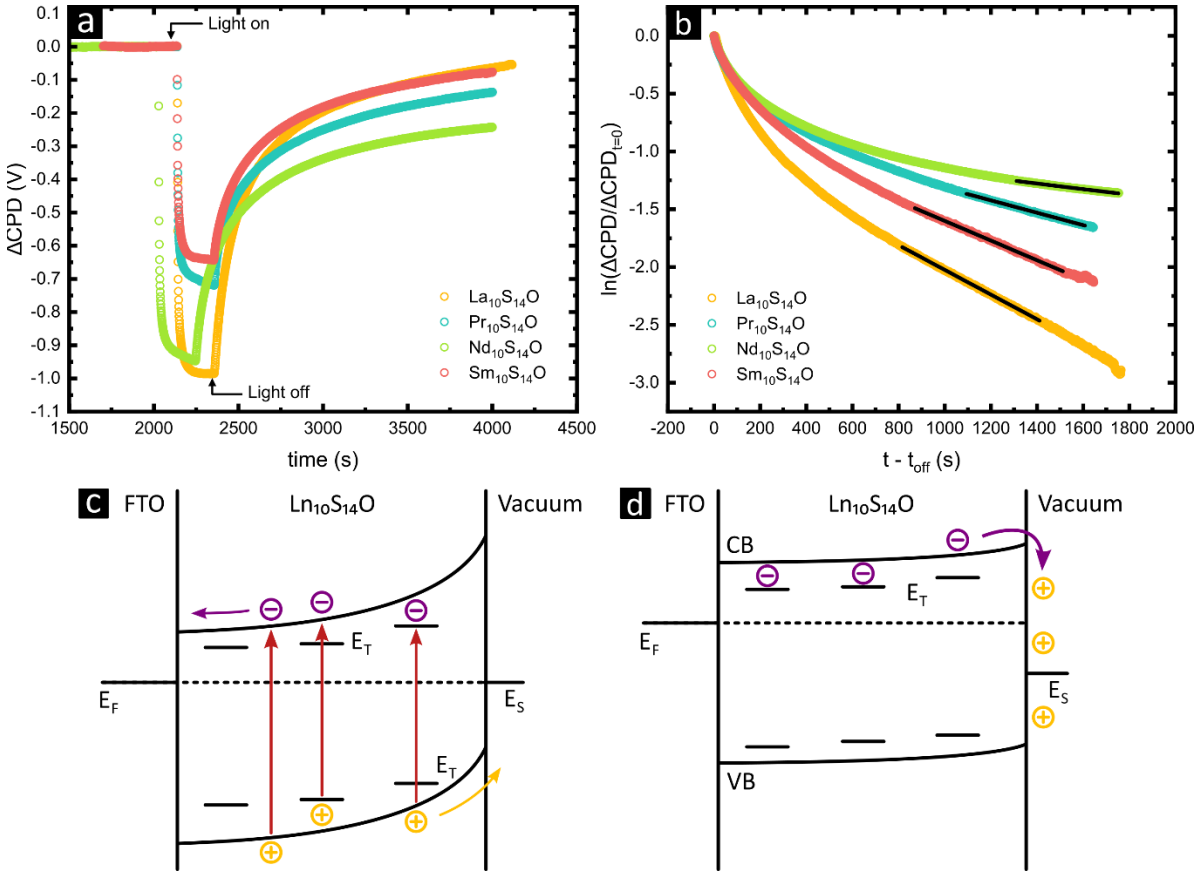


Figure 3.8. Photovoltage decay data of $La_{10}S_{14}O$, $Pr_{10}S_{14}O$, $Nd_{10}S_{14}O$, and $Sm_{10}S_{14}O$. (a) ΔCPD as a function of time, indicating the illumination period; (b) logarithmic plot of the normalized ΔCPD decay, and straight lines indicate linear regressions; (c) excitation and charge transfer pathways from both band gap and sub-band gap states *E*T contribute to the surface photovoltage signal; and (d) electron transfer into surface states *E*S limits the recombination rate at $t > 800$ s.

Much like Ce_2O_2S,[53] $Ce_{10}S_{14}O$ presents interesting optoelectronic properties. In stark contrast with the remaining light lanthanoid oxysulfides, $Ce_{10}S_{14}O$ exhibits a considerably narrower band gap, which endows it with a bright red color (Figure 3.4a) and no observable charge separation upon illumination (Figure S3.9). Previous studies on Ce_2O_2S have shown that oxidation can generate homogeneously disperse Ce(IV) ions with trapped electrons, which can lead to valence band → excitonic-type level transitions.[54,55] However, there is no evidence of the existence of Ce(IV) in $Ce_{10}S_{14}O$ due to the absence of its characteristic XPS and XAS signals

(Figures 3.3 and S3.6). Ce(III) presents intense orbitally allowed 4f → 5d transitions in the 650–500 nm range,[54,56] which may explain the lack of photovoltage signal through fast exciton recombination. Further transient absorption and photoluminescence studies may shed light into the distinct optical properties of this oxysulfide.

Conclusions

$Ln_{10}S_{14}O$ are a series of complex oxysulfides with large unit cells that demonstrate semiconducting properties. Based on diffuse reflectance UV–vis spectroscopy, all $Ln_{10}S_{14}O$ studied show band gap energies in the visible region of the electromagnetic spectrum, exhibiting colors from white-yellow for La to bright red for Ce. Furthermore, through Tauc plot and DASF analysis, we determined for the first time that these oxysulfides are direct semiconductors.

Surface photovoltage spectroscopy showed that the majority carriers in $La_{10}S_{14}O$, $Pr_{10}S_{14}O$, $Nd_{10}S_{14}O$, and $Sm_{10}S_{14}O$ are electrons, classifying them as n-type semiconductors. La, Pr, Nd, and Sm oxysulfides exhibit appreciable surface photovoltage signals at energies below their corresponding optical band gaps, which may be rooted in sulfide vacancies and lanthanoid 4f orbitals forming mid-gap donor states. Moreover, photovoltage decay spectroscopy experiments revealed that carrier recombination at long timescales (t > 800 s) is limited by electron transfer into surface states. The observation of long-lived photogenerated charge carriers in lanthanoid oxysulfides may be of interest for their utilization as potential photocatalysts or light absorbers in solar energy conversion applications. On the other hand, the intensely red colored $Ce_{10}S_{14}O$ (band gap 2 eV) shows no surface photovoltage, the cause of which is a target of ongoing studies.

Experimental Method

Synthesis.

All lanthanoid oxysulfides were synthesized through a high-temperature solid-state sulfurization method in a tube furnace, using H_2S (Matheson Tri Gas) as sulfur source and Ar or

forming gas (96% Ar, 4% H2) as carrier gases. $La_{10}S_{14}O$, $Nd_{10}S_{14}O$, and $Sm_{10}S_{14}O$ were synthesized starting from their corresponding oxides, Ln_2O_3 (99.5%, Sigma-Aldrich). The synthesis of $Pr_{10}S_{14}O$ comprised a two-step method. First, 1 g of $Pr(NO_3)_3 \cdot 6H_2O$ (99.9%, Sigma-Aldrich) was dissolved in 20 mL of Nanopure water (18 MΩ resistivity). Amorphous $Pr(OH)_3$ was then precipitated by slow addition of stoichiometric amounts of 1 M NaOH, and the obtained solid was vacuum filtered. The solid was washed with Nanopure water and dried under air. $Ce_{10}S_{14}O$ synthesis used CeO_2 (Sigma-Aldrich) as the precursor and forming gas to perform the reduction of Ce(IV) to Ce(III). In a typical synthesis, 100 mg of the lanthanide precursor is evenly distributed in an alumina boat such that the surface area is maximized, introduced into an open quartz tube and placed in the center of a tube furnace (Lindberg Blue M, Thermo Fisher). The air contained within the tube is removed by application of vacuum for 5 min, followed by back filling with Ar to atmospheric pressure, and opening to a bubbler placed downstream, thus ensuring that the flowing reaction medium is inert. Afterward, the sample is heated to 1100 °C (44 °C/min ramp rate) under 100 sccm of carrier gas. When the target temperature is reached, 10 sccm of H_2S is added to the reaction mixture and sulfurization is carried out for ~1 h (time will depend upon the exact mass of the precursor used). Subsequently, the flow of H_2S is stopped and the sample cooled under the carrier gas flow (50 °C/min ramp rate).

Characterization.

Powder X-ray Diffraction (PXRD). Diffractograms from each solid were obtained using a Bruker Eco-Advance diffractometer equipped with a Cu K_α source (1.5406 Å). Rietveld refinements were performed using the Topas software (Bruker).

Diffuse Reflectance UV–vis. Sample powders were suspended (20 mg/mL) in isopropanol (IPA) by sonication for at least 20 min and drop casted onto glass slides. The reflectance spectra

of the dry films were measured in a Thermo Fisher Evolution 220 spectrophotometer in which an Al_2O_3 standard (Labsphere) was used for background subtraction.

Scanning Electron Microscopy (SEM). Micrographs of different oxysulfides were obtained with a Scios scanning electron microscope (FEI), equipped with an energy dispersive X-ray spectroscope (Oxford Instruments). Due to their large band gaps, samples were sputtered with gold using a Quorum Tech Q150RES sputter coater before imaging. Typically, 5 nm of Au was sputtered onto powders.

Surface Photovoltage Spectroscopy (SPS). Measurements of $Ln_{10}S_{14}O$ particle films were conducted under vacuum (<2 x 10^{-4} mbar). A gold Kelvin probe (Delta PHI Besocke) served as the reference electrode. Samples were illuminated with monochromatic light from a 300 W halogen lamp filtered through an Oriel Cornerstone 130 monochromator (0.001–0.86 mW cm^{-2}; Newport Corporation, Irvine, CA) in the 3390–40,000 cm^{-1} regime. Transient surface photovoltage measurements were performed using a 400 nm LED at 12.5 mW cm^{-2} that was turned on and off after reaching a steady value. One data point was taken per second. The contact potential difference (CPD) spectra and decay scans were corrected for drift effects by subtracting a fitted logarithmic curve of a dark scan from the light scan. Sample films were deposited on FTO substrates (sonicated twice in acetone, rinsed with Nanopure water, sonicated in Nanopure water, and dried in air at 70 °C before use). Approximately 5 mg of $Ln_{10}S_{14}O$ was dispersed in 500 μL of pure ethanol by sonicating for 30 min. Particle suspension (20 μL) was dropped on the FTO substrate with a circle mask of 7 mm diameter. Films were allowed to dry in air at room temperature. Additional layers of 20 μL of the particle suspension were applied if the film appeared highly transparent.

X-ray Absorption Spectroscopy (XAS). Ln L-edge X-ray absorption spectroscopy was performed at the Stanford Synchrotron Radiation Lightsource (SSRL, BL 4–3) and analyzed with the Demeter software package (see Supporting Information).[57,58] Samples were loaded under air, into a well equipped with Kapton windows. Measurements were performed in fluorescence mode,

using a Lytle detector; appropriate metal reference foils were concomitantly measured in transmission mode for energy calibration. The beamline was equipped with three ionization chambers through which N_2 gas was flown.

X-ray Photoelectron Spectroscopy (XPS). Photoelectron spectroscopy was carried out in a Kratos Supra Axis Spectrometer (Shimadzu corporation) with a monochromatic Al K_α source (1486.6 eV). Data was processed with the ESCApe software. Charge correction was applied using adventitious C 1s (284.4 eV) as reference; high resolution scans were fitted with a static Shirley background function,59 and peaks were modeled using a Gaussian*Lorentzian 0.3 mixture (where 1 is full Lorentzian).

Mott–Schottky Analysis. Electrodes were prepared by drop casting a suspension of each lanthanoid oxysulfide in isopropanol (20 mg/ mL) onto indium tin oxide (ITO)-coated glass slides. Front electrical contacts were made with conductive silver paint, and epoxy resin was used to mask the electrical contact and delimit the electrode area (~1 cm in diameter). Staircase potentio-electrochemical impedance spectroscopy (SPEIS) was performed with a bipotentiostat (Biologic S.A.) with a sinusoidal amplitude of 10 mV in the potential range of –1 to 0 V vs Ag/AgCl, in a 0.1 M Na_2SO_4 electrolyte purged with argon for 10 min, with graphite as a counter electrode.

Supporting Information

Rietveld refinements; EXAFS fitting parameters; Raman spectra; SEM images; Tauc plot fitting parameters; extended range DASF analyses fits; and additional SPS data

Notes

SAFETY: H_2S is an acutely toxic gas that must be placed in a properly ventilated location with adequate engineering controls. In our setup, the cylinder is located inside a fume hood, and a detector (Honeywell) is used to alert of any potential leaks. Furthermore, it is advisable to place a suitable scrubber downstream to trap unreacted H2S (e.g., NaOH + H_2O_2).

Acknowledgements

J.M.V. thanks the University of California, Davis, for start-up funding. J.M.V. also acknowledges support from the Cottrell Scholars program supported by the Research Corporation for Science Advancement (RCSA 26780), as well as support from the National Science Foundation through the Faculty Early Career Development Program (DMR-2044403) and the Camille Dreyfus Teacher-Scholar Awards Program (TC-22- 096-0). Use of the Stanford Synchrotron Radiation Lightsource, SLAC National Accelerator Laboratory, is supported by the U.S. Department of Energy, Office of Science, Office of Basic Energy Sciences under Contract No. DE-AC02-76SF00515. XPS characterization was performed at the Advanced Materials Characterization and Testing Laboratory (AMCaT), funded through the National Science Foundation (DMR-1828238). Part of this study was carried out at the UC Davis Center for Nano and Micro Manufacturing (CNM2). Support for surface photovoltage spectroscopy measurements was provided by the U.S. Department of Energy, Office of Science, Office of Basic Energy Sciences under Award Number DOE-SC0015329.

Publication Information, Copyright, and Author Acknowledgements

This chapter forms the basis for the following publication:

Wuille Bille, B. A.; Kundman A. C.; Osterloh, F. E.; Velázquez, J. M. "$Ln_{10}S_{14}O$ (Ln = La, Pr, Nd, Sm) Oxysulfides: A Series of Direct n-type Semiconductors" – *Chem. Mater.* **2022**, 34, 16, 7553-7562, DOI: 10.1021/acs.chemmater.2c01244

This chapter was adapted with permission from Wuille Bille, B. A.; Kundman A. C.; Osterloh, F. E.; Velázquez, J. M. "$Ln_{10}S_{14}O$ (Ln = La, Pr, Nd, Sm) Oxysulfides: A Series of Direct n-type Semiconductors" – *Chem. Mater.* **2022**, 34, 16, 7553-7562. © Copyright 2022 American Chemical Society

References

(1) Haxel, G. B.; Hedrick, J. B.; Orris, G. J. Rare Earth Elements - Critical Resources for High Technology https://pubs.usgs.gov/fs/ 2002/fs087-02 (accessed Dec 10, 2021).

(2) Bünzli, J.-C. G. Benefiting from the Unique Properties of Lanthanide Ions. *Acc. Chem. Res.* **2006**, *39*, 53–61.

(3) Tricoire, M.; Mahieu, N.; Simler, T.; Nocton, G. Intermediate Valence States in Lanthanide Compounds. *Chem. – Eur. J.* **2021**, *27*, 6860–6879.

(4) Múnera, J. F.; Irusta, S.; Cornaglia, L. M.; Lombardo, E. A.; Vargas Cesar, D.; Schmal, M. Kinetics and Reaction Pathway of the CO2 Reforming of Methane on Rh Supported on Lanthanum-Based Solid. *J. Catal.* **2007**, *245*, 25–34.

(5) Call, F.; Roeb, M.; Schmu, M.; Sattler, C.; Pitz-paal, R. Ceria Doped with Zirconium and Lanthanide Oxides to Enhance Solar Thermochemical Production of Fuels. *J. Phys. Chem. C* **2015**, *119*, 6929–6938.

(6) Ranjit, K. T.; Bossmann, S. H.; Braun, A. M.; et al. Lanthanide Oxide-Doped Titanium Dioxide Photocatalysts: Novel Photocatalysts for the Enhanced Degradation of p - Chlorophenoxyacetic Acid. *Environ. Sci. Technol.* **2001**, *35*, 1544–1549.

(7) Golubkov, A. V.; Kazanin, M. M.; Kaminskii, V. V.; Sokolov, V. V.; et al. Thermoelectric Properties of SmSx (x = 0.8–1.5). *Inorg. Mater.* **2003**, *39*, 1251–1256.

(8) Jundale, S. B.; Lokhande, C. D. (Photo)Electrochemical Studies on p-Sm2S3 Films. *Sol. Energy Mater. Sol. Cells* **1992**, *28*, 151–157.

(9) Maestro, P.; Huguenin, D. Industrial Applications of Rare Earths: Which Way for the End of the Century. *J. Alloys Compd.* **1995**, *225*, 520–528.

(10) Tomczak, J. M.; Pourovskii, L. V.; Vaugier, L.; Georges, A.; Biermann, S. Rare-Earth vs. Heavy Metal Pigments and Their Colors from First Principles. *Proc. Natl. Acad. Sci. U.S.A.* **2013**, *110*, 904–907.

(11) Schleid, T.; Lissner, F. M10S14O-Type Oxysulphides (M = La, Ce, Pr, Nd, Sm) as an "Oxygen Trap" in Oxidation Reactions of Reduced Lanthanide Chlorides with Sulphur. *J. Less-Common Met.* **1991**, *175*, 309–319.

(12) Liu, Y.; Jing, X.; Wang, P.; Yin, T.; Ji, D.; Zhang, M. Rapid Production of Ln2O2S:Eu3+/Tb3+ (Ln = Sm, La, Gd, and Y) Phosphors by Molten Salt Electrolysis. *ACS Appl. Energy Mater.* **2018**, *1*, 1191–1199.

(13) Lin, S. L.; Liu, T. Y.; Lo, C. L.; Wang, B. S.; Lee, Y. J.; Lin, K. Y.; Chang, C. A. Synthesis, Surface Modification, and Photophysical Studies of Ln2O2S:Ln'3+ (Ln = Gd, Tb, Eu; Ln' = Tb and/or Eu) Nanoparticles for Luminescence Bioimaging. *J. Lumin.* **2016**, *175*, 165–175.

(14) Valsamakis, I.; Flytzani-Stephanopoulos, M. Sulfur-Tolerant Lanthanide Oxysulfide Catalysts for the High-Temperature Water- Gas Shift Reaction. *Appl. Catal. B* **2011**, *106*, 255–263.

(15) Tan, S.; Paglieri, S. N.; Li, D. Nano-Scale Sulfur-Tolerant Lanthanide Oxysulfide/Oxysulfate Catalysts for Water-Gas-Shift Reaction in a Novel Reactor Configuration. *Catal. Commun.* **2016**, *73*, 16–21.

(16) Bludau, W.; Wichelhaus, W. Photoluminescence of Doped La10S14O. *J. Appl. Phys.* **1981**, *52*, 2750–2755.

(17) Ikeue, K.; Ando, S.; Mitsuyama, T.; Ohta, Y.; Arayama, K.; Tsutsumi, A.; Machida, M. Photocatalytic Property and Electronic Structure of Lanthanide-Based Oxysulfides. *Top. Catal.* **2008**, *47*, 175–180.

(18) Schleid, T.; Weber, F. A. Crystal Structure of Dekagadolinium- (III) Oxide Tetradekasulfide, Gd10OS14. *Z. Kristallogr. - New Cryst. Struct.* **1998**, *213*, 32.

(19) Besançon, P.; Carre, D.; Laruelle, P. Mécanisme de La Solution Solide Des Oxysulfures de Terres Rares L10S15–xOX. *Acta Crystallogr., Sect. B: Struct. Crystallogr. Cryst. Chem.* **1973**, *29*, 1064–1066.

(20) Besançon, P. Teneur En Oxygéne et Formule Exacte d'une Famille de Composés Habituellement Appelés "Variété*β*" Ou "Phase Complexe" Des Sulfures de Terres Rares. *J. Solid State Chem.* **1973**, *7*, 232–240.

(21) Vaughan, C. M.; White, W. B. Role of Oxygen in Rare-Earth Chalcogenide Semiconductors. *MRS Online Proc. Libr.* **1987**, *97*, 397–402.

(22) Knight, D. S.; White, W. B. Raman Line Widths in Rare-Earth Sesquisulfides Solid Solutions. *J. Am. Ceram. Soc.* **1996**, *79*, 1394– 1396.

(23) Knight, D. S.; White, W. B. Raman Spectroscopic Study of the Rare Earth Sesquisulfides. *Spectrochim. Acta, Part A* **1990**, *46*, 381– 387.

(24) Asakura, H.; Shishido, T.; Fuchi, S.; Teramura, K.; Tanaka, T. Local Structure of Pr, Nd, and Sm Complex Oxides and Their X-Ray Absorption near Edge Structure Spectra. *J. Phys. Chem. C* **2014**, *118*, 20881–20888.

(25) Loble, M. W.; Keith, J. M.; Altman, A. B.; Stieber, S. C. E.; Batista, E. R.; Boland, K. S.; Conradson, S. D.; Clark, D. L.; Lezama Pacheco, J.; Kozimor, S. A.; Martin, R. L.; Minasian, S. G.; Olson, A. C.; Scott, B. L.; Shuh, D. K.; Tyliszczak, T.; Wilkerson, M. P.; Zehnder, R. A. Covalency in Lanthanides. An X-Ray Absorption Spectroscopy and Density Functional Theory Study of LnCl6 x- (x = 3, 2). *J. Am. Chem. Soc.* **2015**, *137*, 2506–2523.

(26) Gompa, T. P.; Ramanathan, A.; Rice, N. T.; La Pierre, H. S. The Chemical and Physical Properties of Tetravalent Lanthanides: Pr, Nd, Tb, and Dy. *Dalton Trans.* **2020**, *49*, 15945–15987.

(27) Kvashnina, K. O.; Butorin, S. M.; Glatzel, P. Direct Study of the F-Electron Configuration in Lanthanide Systems. *J. Anal. At. Spectrom.* **2011**, *26*, 1265–1272.

(28) Jorgensen, C. K.; Berthou, H. Split Photo-Electron Signals from the Unique Closed-Shell Cation Lanthanum(III). *Chem. Phys. Lett.* **1972**, *13*, 186–189.

(29) Signorelli, A. J.; Hayes, R. G. X-Ray Photoelectron Spectroscopy of Various Core Levels of Lanthanide Ions: The Roles of Monopole Excitation and Electrostatic Coupling. *Phys. Rev. B: Condens. Matter Mater. Phys.* **1973**, *8*, 81–86.

(30) Berthou, H.; Jorgensen, C. K.; Bonnelle, C. Influence of The Ligands on 3d Photoelectron Spectra of the First Four Lanthanides. *Chem. Phys. Lett.* **1976**, *38*, 199–206.

(31) Burroughs, P.; Hamnett, A.; Orchard, A. F.; Thornton, G. Satellite Structure in the X-Ray Photoelectron Spectra of Some Binary and Mixed Oxides of Lanthanum and Cerium. *J. Chem. Soc., Dalton Trans.* **1976**, 1686–1698.

(32) Tauc, J.; Grigorovici, R.; Vancu, A. Optical Properties and Electronic Structure of Amorphous Germanium. *Phys. Status Solidi B* **1966**, *15*, 627–637.

(33) Kubelka, P.; Munk, F. Ein Beitrag Zur Optik Der Farbanstriche. *Z. Tech. Phys.* **1931**, *12*, 593–601.

(34) Makuła, P.; Pacia, M.; Macyk, W. How To Correctly Determine the Band Gap Energy of Modified Semiconductor Photocatalysts Based on UV-Vis Spectra. *J. Phys. Chem. Lett.* **2018**, *9*, 6814–6817.

(35) Souri, D.; Tahan, Z. E. A New Method for the Determination of Optical Band Gap and the Nature of Optical Transitions in Semiconductors. *Appl. Phys. B: Lasers Opt.* **2015**, *119*, 273–279.

(36) Runowski, M.; Stopikowska, N.; Lis, S. UV-Vis-NIR Absorption Spectra of Lanthanide Oxides and Fluorides. *Dalton Trans.* **2020**, *49*, 2129–2137.

(37) Donchev, V.; Kirilov, K.; Ivanov, T.; Germanova, K. Surface Photovoltage Phase Spectroscopy - a Handy Tool for Characterisation of Bulk Semiconductors and Nanostructures. *Mater. Sci. Eng., B* **2006**, *129*, 186–192.

(38) Kronik, L.; Shapira, Y. Surface Photovoltage Spectroscopy of Semiconductor Structures: At the Crossroads of Physics, Chemistry and Electrical Engineering. *Surf. Interface Anal.* **2001**, *31*, 954–965.

(39) Melo, M. A.; Osterloh, F. E. Defect States Control Effective Band Gap and Photochemistry of Graphene Quantum Dots. *ACS Appl. Mater. Interfaces* **2018**, *10*, 27195–27204.

(40) Wu, P.; Wang, J.; Zhao, J.; Guo, L.; Osterloh, F. E. Structure Defects in G-C3N4 Limit Visible Light Driven Hydrogen Evolution and Photovoltage. *J. Mater. Chem. A* **2014**, *2*, 20338–20344.

(41) Ma, X.; Wu, Z.; Roberts, E. J.; Han, R.; Rao, G.; Zhao, Z.; Lamoth, M.; Cui, X.; Britt, R. D.; Osterloh, F. E. Surface Photovoltage Spectroscopy Observes Sub-Band-Gap Defects in Hydrothermally Synthesized SrTiO3 Nanocrystals. *J. Phys. Chem. C* **2019**, *123*, 25081–25090.

(42) Zhuang, G.; Yan, J.; Wen, Y.; Zhuang, Z.; Yu, Y. Two- Dimensional Transition Metal Oxides and Chalcogenides for Advanced Photocatalysis: Progress, Challenges, and Opportunities. *Solar RRL* **2021**, *5*, No. 2000403.

(43) Shin, D.; Saparov, B.; Mitzi, D. B. Defect Engineering in Multinary Earth-Abundant Chalcogenide Photovoltaic Materials. *Adv. Energy Mater.* **2017**, *7*, No. 1602366.

(44) Colombara, D.; Elanzeery, H.; Nicoara, N.; Sharma, D.; Claro, M.; Schwarz, T.; Koprek, A.; Wolter, M. H.; Melchiorre, M.; Sood, M.; Valle, N.; Bondarchuk, O.; Babbe, F.; Spindler, C.; Cojocaru- Miredin, O.; Raabe, D.; Dale, P. J.; Sadewasser, S.; Siebentritt, S. Chemical Instability at Chalcogenide Surfaces Impacts Chalcopyrite Devices Well beyond the Surface. *Nat. Commun.* **2020**, *11*, No. 3634.

(45) Govindaraju, G. V.; Morbec, J. M.; Galli, G. A.; Choi, K. S. Experimental and Computational Investigation of Lanthanide Ion Doping on BiVO4 Photoanodes for Solar Water Splitting. *J. Phys. Chem. C* **2018**, *122*, 19416–19424.

(46) Mikami, M.; Nakamura, S. Electronic Structure of Rare-Earth Sesquioxides and Oxysulfides. *J. Alloys Compd.* **2006**, *408–412*, 687– 692.

(47) Dittrich, T. *Surface Photovoltage Analysis of Photoactive Materials*; World Scientific Publishing Europe Ltd.: London, **1999**; p 188.

(48) Kronik, L.; Shapira, Y. Surface Photovoltage Phenomena: Theory, Experiment, and Applications. *Surf. Sci. Rep.* **1999**, *37*, 1– 206.

(49) Mora-Sero, I.; Dittrich, T.; Garcia-Belmonte, G.; Bisquert, J. Determination of Spatial Charge Separation of Diffusing Electrons by Transient Photovoltage Measurements. *J. Appl. Phys.* **2006**, *100* (10), 103705.

(50) Peter, L. M.; Li, J.; Peat, R. Surface Recombination at Semiconductor Electrodes. Part I. Transient and Steady-State Photocurrents. *J. Electroanal. Chem. Interfacial Electrochem.* **1984**, *165*, 29–40.

(51) Li, K.; Miao, B.; Fa, W.; Chen, R.; Jin, J.; Bevan, K. H.; Wang, D. Evolution of Surface Oxidation on Ta3N5 as Probed by a Photoelectrochemical Method. *ACS Appl. Mater. Interfaces* **2021**, *13*, 17420–17428.

(52) Salvador, P.; Gutierrez, C. Analysis of the Transient Photocurrent-Time Behaviour of a Sintered n-SrTiO3 Electrode in Water Photoelectrolysis. *J. Electroanal. Chem. Interfacial Electrochem.* **1984**, *160*, 117–130.

(53) Larquet, C.; Nguyen, A. M.; Glais, E.; Paulatto, L.; Sassoye, C.; Selmane, M.; Lecante, P.; Maheu, C.; Geantet, C.; Cardenas, L.; Chaneac, C.; Gauzzi, A.; Sanchez, C.; Carenco, S. Band Gap Engineering from Cation Balance: The Case of Lanthanide Oxysulfide Nanoparticles. *Chem. Mater.* **2019**, *31*, 5014–5023.

(54) Sourisseau, C.; Cavagnat, R.; Mauricot, R.; Boucher, F.; Evain, M. Structure and Bondings in Cerium Oxysulfide Compounds I - Electronic, Infrared and Resonance Raman Spectra of Ce2.0O2.5S. *J. Raman Spectrosc.* **1997**, *28*, 965–971.

(55) Larquet, C.; Nguyen, A. M.; Ávila-Gutierrez, M.; Tinat, L.; Lassalle-Kaiser, B.; Gallet, J. J.; Bournel, F.; Gauzzi, A.; Sanchez, C.; Carenco, S. Synthesis of Ce2O2S and Gd2(1-y)Ce2yO2S Nanoparticles and Reactivity from in Situ X-Ray Absorption Spectroscopy and XRay Photoelectron Spectroscopy. *Inorg. Chem.* **2017**, *56*, 14227– 14236.

(56) Pan, G.; Bai, X.; Yang, D.; Chen, X.; Jing, P.; Qu, S.; Zhang, L.; Zhou, D.; Zhu, J.; Xu, W.; Dong, B.; Song, H. Doping Lanthanide into Perovskite Nanocrystals: Highly Improved and Expanded Optical Properties. *Nano Lett.* **2017**, *17*, 8005–8011.

(57) Ravel, B.; Newville, M. ATHENA, ARTEMIS, HEPHAESTUS: Data Analysis for X-Ray Absorption Spectroscopy Using IFEFFIT. *J. Synchrotron Radiat.* **2005**, *12*, 537–541.

(58) Newville, M. IFEFFIT: Interactive XAFS Analysis and FEFF Fitting. *J. Synchrotron Radiat.* **2001**, *8*, 322–324.

(59) Engelhard, M. H.; Baer, D. R.; Herrera-gomez, A.; Herrera- Gomez, A.; Sherwood, P. M. A. Introductory Guide to Backgrounds in XPS Spectra and Their Impact on Determining Peak Intensities. *J. Vac. Sci. Technol. A* **2020**, *38*, No. 063203.

Supporting Information

Powder X-ray Diffraction – Rietveld Refinements

Processing details: Rietveld refinements were performed with the Topas 5 software (Bruker). The emission profile of the Eco-Advance PXRD (Bruker) was a Cu $K_{\alpha1,\alpha2}$ with an area ratio of ~0.65/0.35. Chebychev polynomials of order 9 were used for the background fit, as a well as a 1/x function for the low angle scattering portions.

The instrument parameters used were the following:

Goniometer Radii

- Primary radius (mm) 280
- Secondary radius (mm) 280

Equatorial Convolution

- Linear PSD 2Th angular range (°) 3
- FDS angle (°) 0.3

Full Axial Convolution

- Filament length (mm) 12
- Sample length (mm) 15
- Receiving Slit length (mm) 12
- Primary Sollers (°) 2.5
- Secondary Sollers (°) 2.5

Crystallite and strain were modelled with Lorentzian and Gaussian functions, respectively.

Table S3.1. Summarized Rietveld refinement parameters for all oxysulfides

	Material				
Refinement parameter	**$La_{10}S_{14}O$**	**$Ce_{10}S_{14}O$**	**$Pr_{10}S_{14}O$**	**$Nd_{10}S_{14}O$**	**$Sm_{10}S_{14}O$**
R_{wp}	19.68	21.58	21.76	20.05	18.99
Space Group	I41/acdZ	I41/acdZ	I41/acdZ	I41/acdZ	I41/acdZ
a (Å)	15.359(3)	15.270(8)	15.166(0)	15.016(0)	14.851(3)
c (Å)	20.378(7)	20.248(1)	20.120(8)	19.929(0)	19.724(7)
c/a	1.3268	1.3260	1.3266	1.3272	1.3281

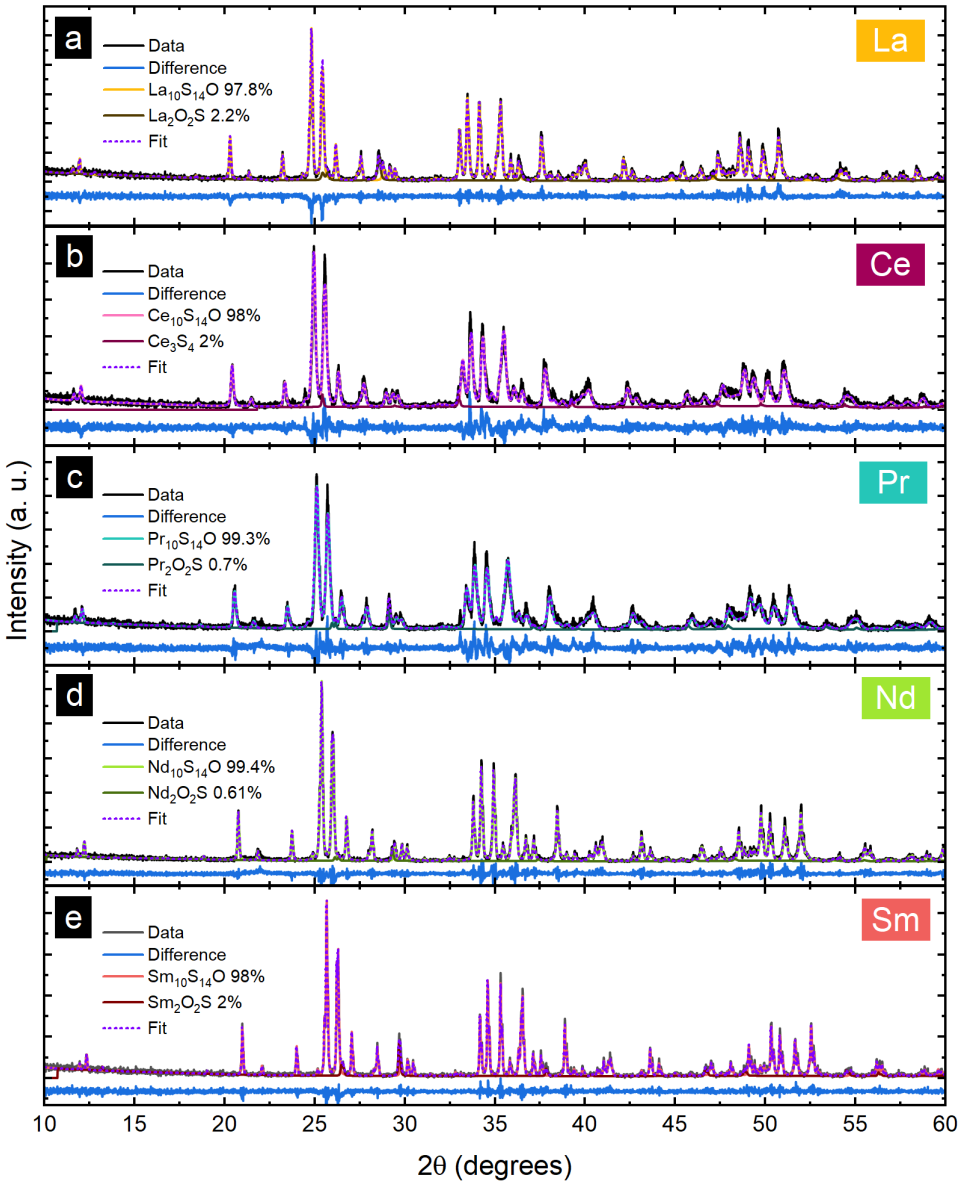


Figure S3.1. Rietveld refinements for a) $La_{10}S_{14}O$, b) $Ce_{10}S_{14}O$, c) $Pr_{10}S_{14}O$, d) $Nd_{10}S_{14}O$, and e) $Sm_{10}S_{14}O$. Traces in black, blue, and violet represent the experimental data, difference, and fit. The remaining 2 traces represent the $Ln_{10}S_{14}O$ and secondary phases.

EXAFS Analysis

S_0^2 was set at 0.73, following a previous report[1] and using the principle of chemical transferability. For all lanthanoid oxysulfides, the scattering paths calculated with FEFF6 (through the Demeter suite) belong to multiple different crystallographic sites. That is, for the fitting process, scattering paths from lanthanoid ions occupying both 32g Wyckoff positions as well as 16f were used. The former are labeled as Ln1 and Ln2 in **Table S3.3**. Ln2 contains one O atom and six S atoms in the first coordination shell. Those ions occupying the 16f Wyckoff positions are labeled Ln3 in said table (if used). In the parametrization process, the effective scattering distance (R_{eff}) was allowed to variate by a fraction of its nominal value obtained from crystallographic data (i. e. $\Delta R = R_{eff}*\alpha$). The parameters "N" were used to fit the coordination number (or degeneracy) of each path.

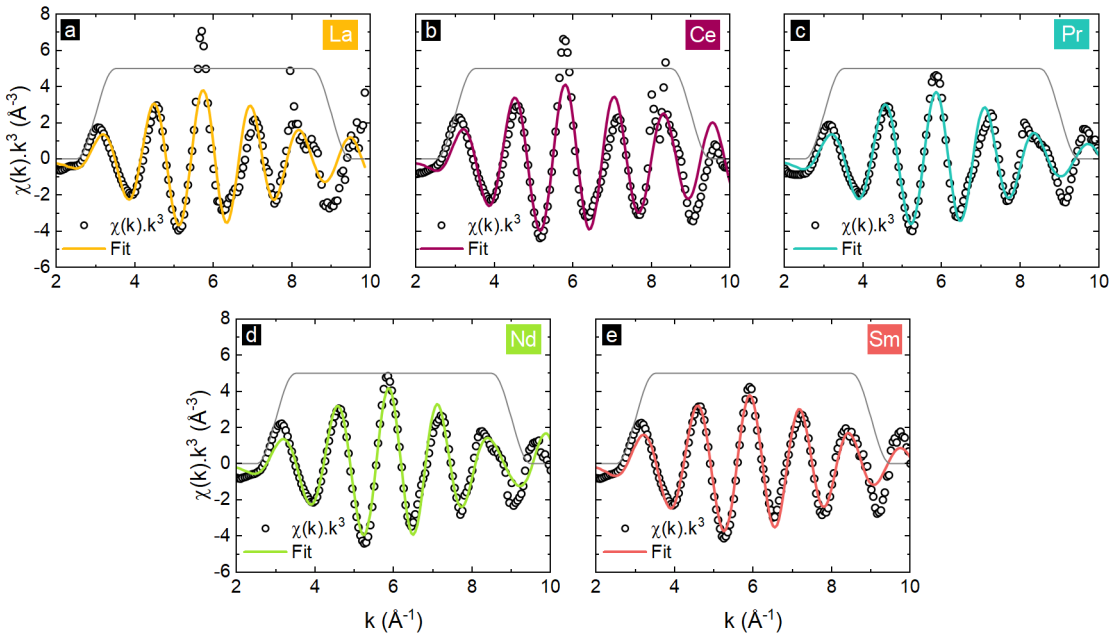


Figure S3.2. k-space FT-EXAFS fit for each oxychalcogenide. In each graph, the scatter plot, solid trace, and grey trace represent the data, fit result, and Hanning window used, respectively.

Table S3.2. Ln L_3-edge EXAFS fitting parameters.

$Ln_{10}S_{14}O$	Parameter	Type	Value	Uncertainty
La	S_0^2	Set	0.73	-
	E_0	Guess	3.34	1.53
	α	Guess	0.0274	0.00678
	σ^2	Guess	0.00776	0.00133
Ce	S_0^2	Set	0.73	-
	E_0	Guess	2.77	1.42
	α	Guess	0.0097	0.00613
	σ^2	Guess	0.00621	0.00126
Pr	S_0^2	Set	0.73	-
	E_0	Guess	1.40	1.04
	α	Guess	-0.00954	0.00417
	σ^2	Guess	0.00835	0.000815
Nd	S_0^2	Set	0.73	-
	E_0	Guess	1.16	1.15
	α	Guess	-0.0120	0.00459
	σ^2	Guess	0.00366	0.000879
Sm	S_0^2	Set	0.73	-
	E_0	Guess	1.01	0.80
	α	Guess	-0.0161	0.00335
	σ^2	Guess	0.00429	0.000672

Table S3.3. Ln-S scattering distances and coordination derived from the fitting parameters detailed in Table S3.2.

$Ln_{10}S_{14}O$	Coord. shell	Absorber site (LnX)	Scattering distance (Å)	Uncertainty	Degeneracy
La	1st	La1	2.944	0.019	2
		La1	3.027	0.020	2
		La2	2.919	0.019	2
		La2	3.024	0.020	1
	2nd	La2	3.522	0.023	2
Ce	1st	Ce1	2.917	0.018	2
		Ce2	2.941	0.018	2
		Ce1	2.967	0.018	2
		Ce2	2.839	0.017	1
	2nd	Ce1	3.491	0.021	1
Pr	1st	Pr1	2.838	0.012	2
		Pr1	2.933	0.012	2
		Pr2	2.983	0.012	1
		Pr2	2.864	0.012	2
	2nd	Pr1	3.408	0.014	2
Nd	1st	Nd2	2.746	0.013	1
		Nd2	2.842	0.013	2
		Nd1	2.869	0.013	1
		Nd1	2.908	0.013	2
		Nd2	3.053	0.014	1
	2nd	Nd1	3.392	0.013	2
Sm	1st	Sm2	2.698	0.0092	1
		Sm2	2.797	0.0095	2
		Sm2	2.925	0.0099	2
		Sm2	2.859	0.0097	1
		Sm3	2.846	0.0097	1
	2nd	Sm1	3.351	0.011	1

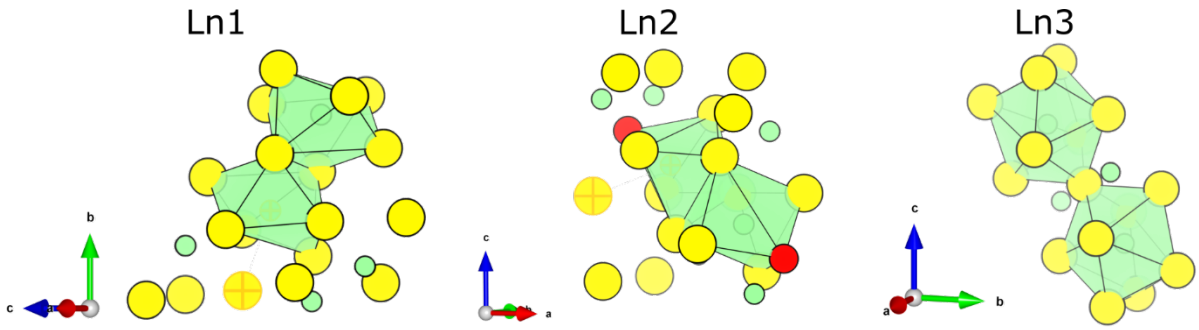


Figure S3.3. Representative coordination environments corresponding to each lanthanoid crystallographic site (enclosed within the light-green polyhedra). The closest second shell S^{2-} ion ($r > 3.3$ Å) is highlighted in Ln1 and Ln2 with an orange crosshair.

Raman Spectro-microscopy

Spectra were recorded in a Renishaw RM1000 Raman microscope with motorized stage with an incident wavelength of 785 nm. The energy alignment was calibrated against a Si standard (Raman shift = 520 cm^{-1}).

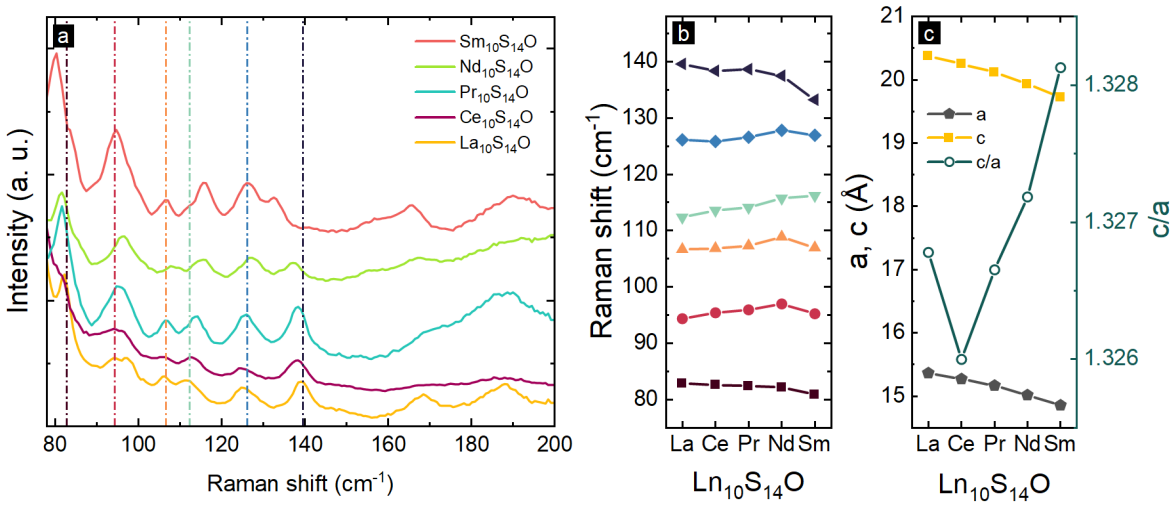


Figure S3.4. a) Raman spectra for all $Ln_{10}S_{14}O$, shown offset for clarity; b) Raman shift of selected peaks [marked with reference lines of matching color in a)] as a function of lanthanoid ion; c) lattice parameter changes (derived from the Rietveld refinements).

$Ln_{10}S_{14}O$ morphology

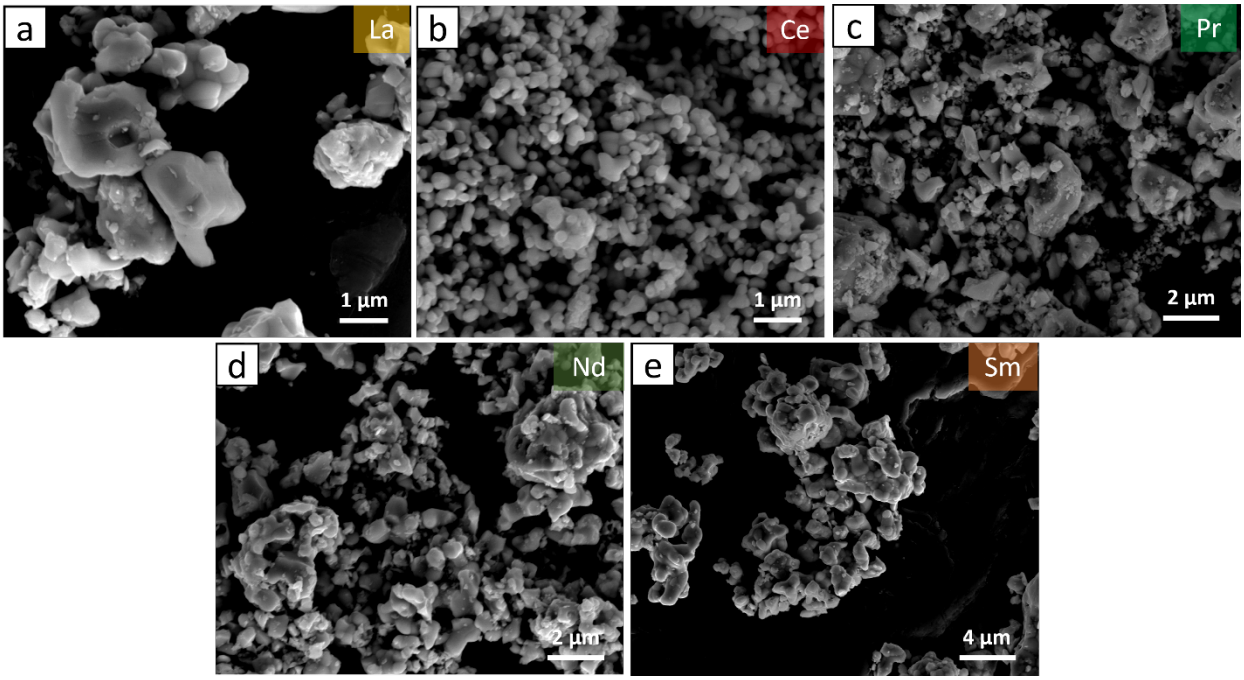


Figure S3.5. Scanning electron micrographs for a) $La_{10}S_{14}O$, b) $Ce_{10}S_{14}O$, c) $Pr_{10}S_{14}O$, d) $Nd_{10}S_{14}O$, and e) $Sm_{10}S_{14}O$.

Electronic Structure – XANES

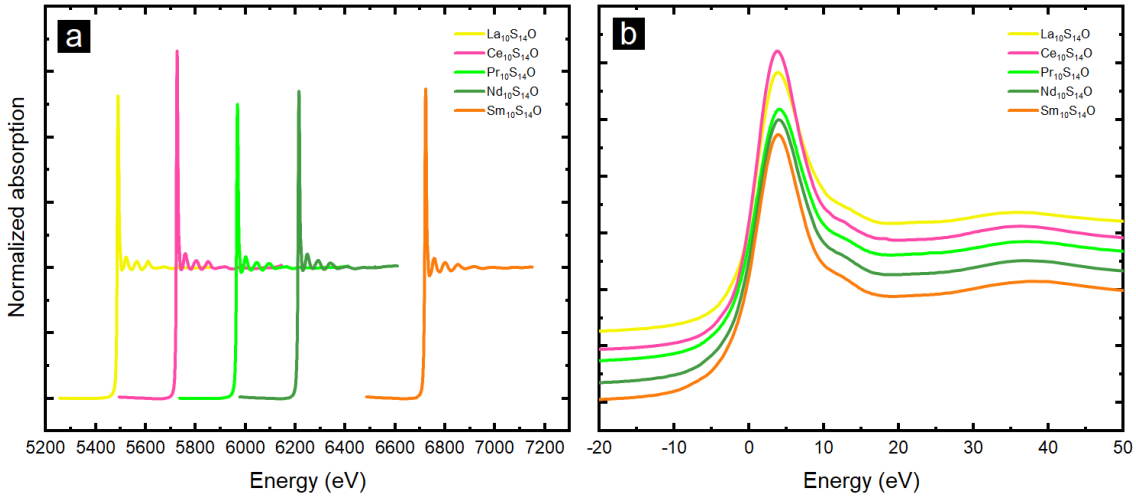


Figure S3.6. L_3-edge XAS spectra of $Ln_{10}S_{14}O$, shown at their corresponding energies, a), and overlaid to highlight the white line region, b).

Diffuse Reflectance UV-Vis Spectroscopy - Tauc Analysis

Table S 3.4. Linear regression fitting parameters from Direct and Indirect Tauc plot analyses.

Tauc Plot Analysis		
Direct		
	Slope	y intercept
$La_{10}S_{14}O$	1237 ± 18	-3511 ± 53
$Ce_{10}S_{14}O$	542.7± 3.3	-1097.9 ± 7.0
$Pr_{10}S_{14}O$	531 ± 15	-1362 ± 41
$Nd_{10}S_{14}O$	1550 ± 71	-4092 ± 192
$Sm_{10}S_{14}O$	269.8 ± 3.2	-650.6 ± 7.9
Indirect		
	Slope	y intercept
$La_{10}S_{14}O$	16.22 ± 0.21	-44.02 ± 0.60
$Ce_{10}S_{14}O$	11.947 ± 0.087	-22.47 ± 0.18
$Pr_{10}S_{14}O$	8.91 ± 0.34	-21.02 ± 0.90
$Nd_{10}S_{14}O$	16.13 ± 0.36	-40.43 ± 0.96
$Sm_{10}S_{14}O$	8.18 ± 0.11	-18.22 ± 0.27

Differential Absorption Spectrum Fitting (DASF)

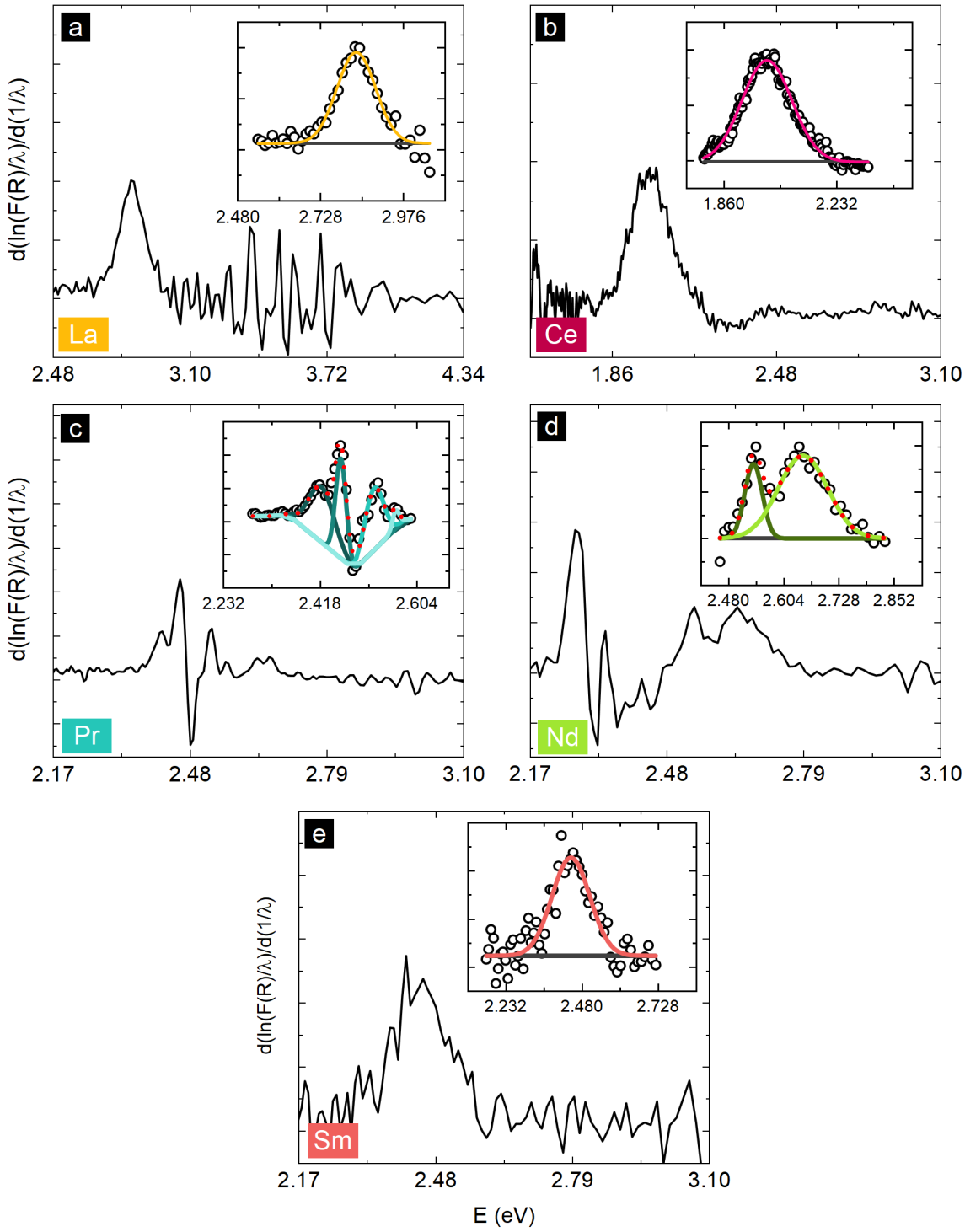


Figure S3.7. Differential absorption spectrum fitting for each lanthanoid oxysulfide. The centroid of the gaussian peaks, shown in the insets, corresponds to the reported E_g through this method.

Surface Photovoltage Spectroscopy

Surface photovoltage spectra for each lanthanoid oxysulfide are shown in **Figure S3.8**.

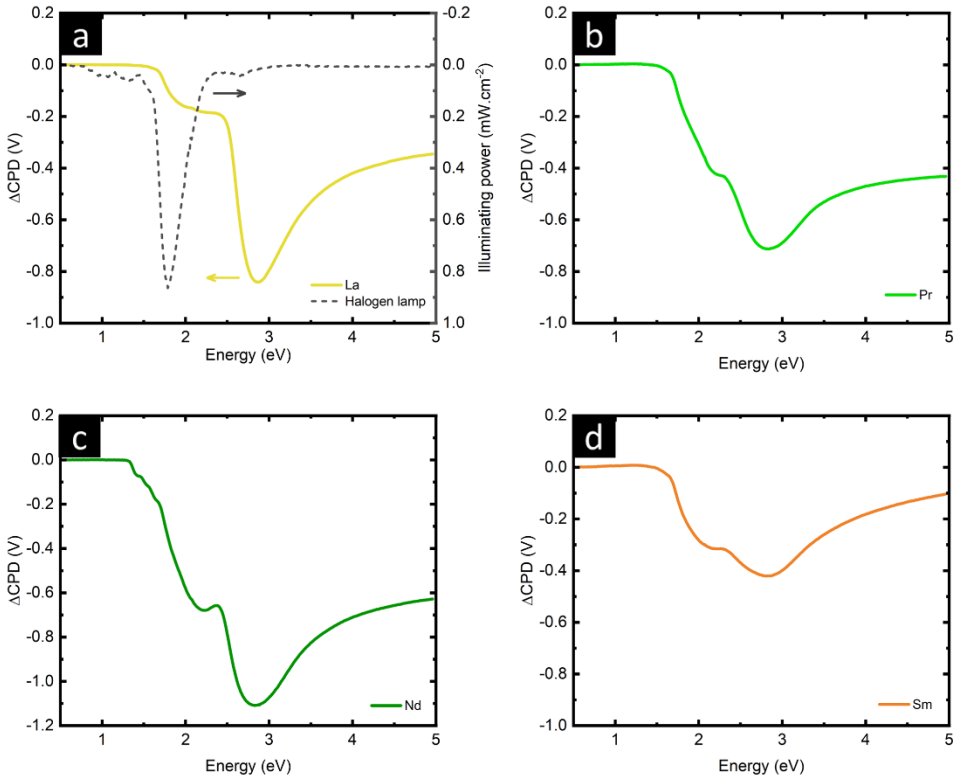


Figure S3.8. Surface photovoltage spectra of a) $La_{10}S_{14}O$, b) $Pr_{10}S_{14}O$, c) $Nd_{10}S_{14}O$, and d) $Sm_{10}S_{14}O$, using a tungsten halogen lamp as illumination source (emission spectrum as dotted line in a).

$Ce_{10}S_{14}O$ films deposited on FTO-coated glass slides exhibited no detectable photovoltage signals as can be seen in **Figure S3.9**.

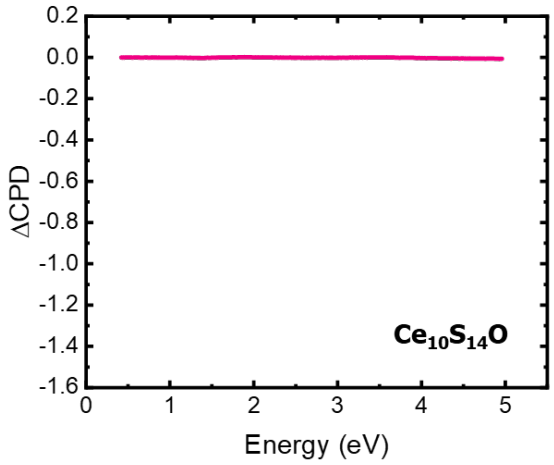


Figure S3.9. Surface photovoltage spectroscopy of $Ce_{10}S_{14}O$ films drop casted onto FTO-coated glass support without thermal treatment.

Table S3.5. Photovoltage decay parameters for each lanthanoid oxysulfide. ΔCPD_{max} corresponds to the maximum photovoltage at the time the illumination was turned off. ΔCPD_f is the photovoltage signal at the end of the experiment, when 27 minutes have elapsed since the end of the illumination time. % ΔCPD_{res} and % $\Delta CPD_{recovered}$ represent the residual and recovered photocurrent signal.

Material	ΔCPD_{max} (V)	ΔCPD_f (V)	% ΔCPD_{res}	% $\Delta CPD_{recovered}$
$La_{10}S_{14}O$	-0.986	-0.053	5.37	94.6
$Pr_{10}S_{14}O$	-0.719	-0.137	19.0	80.9
$Nd_{10}S_{14}O$	-0.947	-0.248	26.2	73.8
$Sm_{10}S_{14}O$	-0.942	-0.076	8.07	91.9

Table S3.6. Photovoltage decay linear fitting parameters corresponding to equation 3.

	$La_{10}S_{14}O$	$Pr_{10}S_{14}O$	$Nd_{10}S_{14}O$	$Sm_{10}S_{14}O$
Slope (s^{-1})	(-1.070 ± 0.001) x 10^{-3}	(-5.367 ± 0.008) x 10^{-4}	(-2.440 ± 0.009) x 10^{-4}	(-8.50 ± 0.01) x 10^{-4}
τ (s)	934.6 ± 0.9	1863 ± 3	4098 ± 15	1176 ± 1

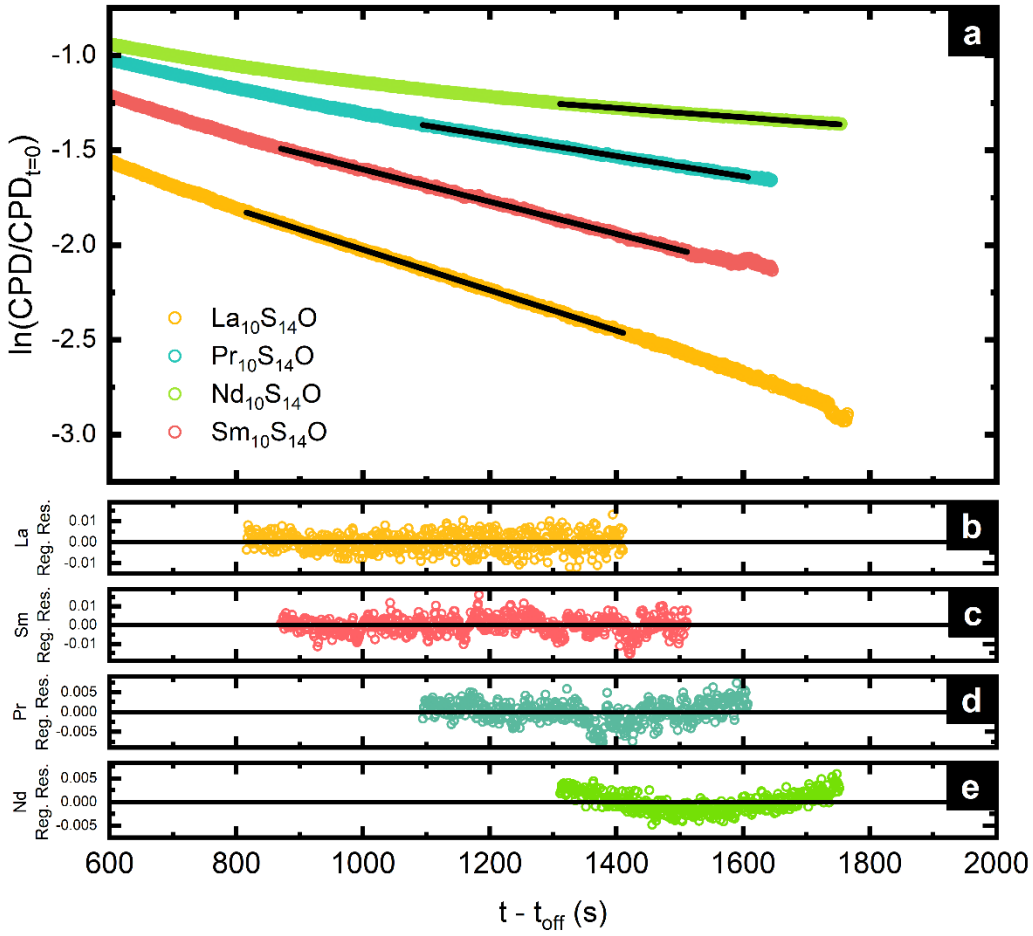


Figure S3.10. a) Linear region of the surface photovoltage decay of $La_{10}S_{14}O$, $Pr_{10}S_{14}O$, $Nd_{10}S_{14}O$, and $Sm_{10}S_{14}O$. Solid black lines represent linear regression curves that best describe the normalized decay (in logarithmic scale) after light irradiation. The corresponding regular residuals are displayed in the following order: b) $La_{10}S_{14}O$, c) $Sm_{10}S_{14}O$, d) $Pr_{10}S_{14}O$, and d) $Nd_{10}S_{14}O$.

Electrochemical Impedance Spectroscopy – Mott-Schottky

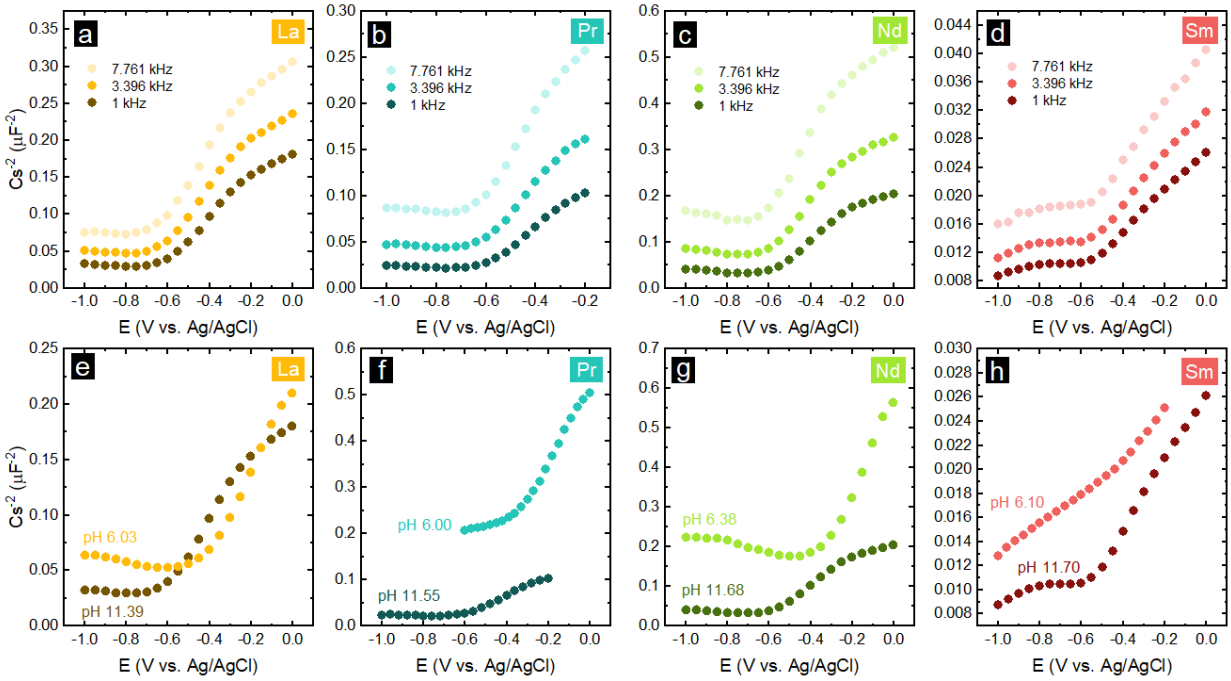


Figure S3.11. Mott-Schottky plots corresponding to $La_{10}S_{14}O$ (a, e), $Pr_{10}S_{14}O$ (b, f), $Nd_{10}S_{14}O$ (c, g), and $Sm_{10}S_{14}O$ (d, h), at 3 different frequencies (1, 3.4 and 7.8 kHz), measured in 0.1 M Na_2SO_4 solution. a) through d) were measured at pH ~ 11.5 and show a frequency dependence, while e) to h) show the effect of pH (at a constant frequency of 1 kHz). The positive slope signifies n-type semiconduction. However, the strong frequency dependence of the signal prevents reliable dopant density and flat-band potential determinations.

References

(1) Malet, P.; Capitan, M. J.; Centeno, M. A.; Odriozola, J. A. EXAFS Data Analysis for Lanthanide Sesquioxides, 1994, *90*, 2783–2790.

4. Chapter 4

Understanding the High-Temperature Reversible Thermochromism in $Ln_{10}S_{14}O$

Abstract

Inorganic thermochromic materials are generally poorly understood from a fundamental basis. Largely represented by metal oxides, transition metal-free chalcogenides are seldom reported for their thermochromic properties. Herein we report on the high temperature reversible thermochromism of $Ln_{10}S_{14}O$ (Ln = La, Ce, Pr, Nd, and Sm). Color space analysis shows that the most dramatic color changes occur in different temperature ranges depending on the lanthanoid ion: at lower temperatures for $Sm_{10}S_{14}O$, between 150 – 300 °C, in the intermediate temperature region for $Pr_{10}S_{14}O$ and $Nd_{10}S_{14}O$, between 250 – 450 °C, and $La_{10}S_{14}O$ exhibiting the highest temperature range for its color change, between 350 – 600 °C. The structural changes that occur with temperature, as probed with *in-situ* X-ray diffraction, involve the expansion of the crystallographic planes up to ~1 %, with no detectable phase changes. In addition, ex-situ heating – cooling experiments showed the reversibility of said structural changes under inert atmospheres and calorimetric studies determined that the greatest oxidation susceptibility occurs at 600 °C. We believe these findings may stimulate the further exploration of this class of materials for exciting new optical and chemical sensing applications.

Introduction

Thermochromism is a concept that defines a change in the color of matter as a function of temperature,[1] which can be reversible or irreversible. The latter tends to originate as a result of chemical reactions, like the dehydration of transition metal complexes, oxidation or thermal decomposition. On the other hand, in inorganic materials, reversible thermochromism can be the result of a variety of different complex phenomena, like semiconductor-to-metal transitions (e.g.,

VO_2),[2] charge transfer between ions (e.g., α-$CuMoO_4$, and transition metal containing garnet structures),[3–5] band gap expansion (e.g., CuO QDs and $(Bi_{1-x}Y_x)_2O_3$),[6,7] or change in the interionic distances (e.g., d-metal containing iodobismuthates).[8] Generally, the origin of the observed thermochromism is a combination of effects, which highlights the difficulty of studying these materials.

Most of the thermochromic inorganic materials with colors in the visible spectrum contain transition metals in their structures, given the availability of valence d-orbitals which are highly susceptible to the strength and symmetry of the ligand field. In comparison, lanthanoids impart luminescent thermochromism to the materials they form, due to their optical activity and unique spectral features.[9] The temperature-dependent photoluminescence of lanthanoid ions has been the subject of extensive investigations as activators and sensitizers for their applications as non-contact nanothermometers.[10–14] These properties have been observed in lanthanoid oxides, fluorides, vanadates and phosphates, with seldom examples of (oxy)chalcogenides and halides.[15]

Herein we report on the high-temperature reversible thermochromic behavior of a series of lanthanoid oxysulfides, synthesized via a high-temperature sulfurization method. All $Ln_{10}S_{14}O$ (Ln = La, Ce, Pr, Nd, and Sm) demonstrate remarkable color changes in the visible spectrum from room temperature to 700 °C, as characterized by their corresponding CIE-Lab color space parameters. In situ X-ray powder diffraction results show that these oxysulfides do not undergo a phase transition within the temperature range. but undergo an expansion of their tetragonal unit cell with heating. The observed thermochromic behavior shows great reversibility under inert sample environments. Conversely, when oxygen is present, at 600 °C the oxysulfides undergo oxidation to the wider band gap Ln_2O_2S, with consequent change in color.

To the best of our knowledge, there are no reports of all-lanthanoid oxysulfide high temperature reversible thermochromic materials in the visible spectrum. We believe these findings may stimulate the further exploration of these class of materials for exciting new optical and chemical sensing applications.

Results and Discussion

Color Change

The colors of all samples from 100 °C to 650 °C are shown in Figure 4.1 a. The initial colors observed at 100 °C match those of the as synthesized lanthanoids, that is, $La_{10}S_{14}O$ and $Sm_{10}S_{14}O$ yellow, $Pr_{10}S_{14}O$ and $Nd_{10}S_{14}O$ green, and $Ce_{10}S_{14}O$ with its characteristic red. As the temperature increased all lanthanoid oxysulfide colors darkened, and then lightened upon cooling, showing great reversibility. The CIELab color parameters[16] (i.e., the color space defined by the coordinates L, a, and b, which measure the lightness level, red-green distribution, and blue-yellow distribution, respectively) were determined from the corresponding photographs and are displayed in Figure 4.1 b, c, and Table S4.1.

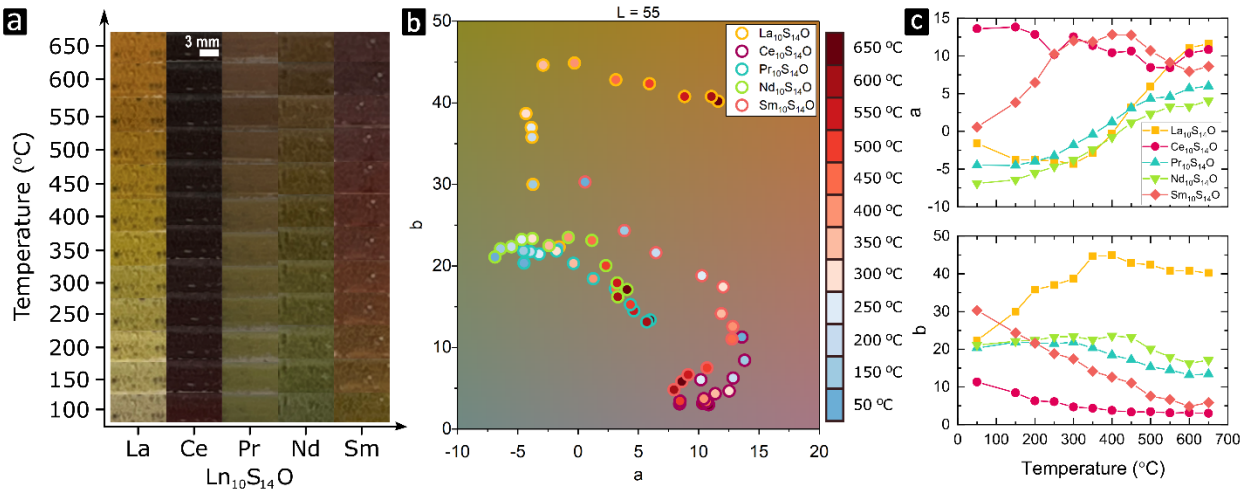


Figure 4.1. a) Photographs of $Ln_{10}S_{14}O$ powders showing the change in their colors as a function of temperature, obtained during the cooling cycle; b) Color space analysis plane (projected in the L = 55) for La, Ce, Pr, Nd, and Sm oxysulfides. The background color represents the observed colors, while the colors inside the scatter plot correspond to the temperature scale on the right. c) demonstrates the progressive changes in *a* and *b* CIE-Lab parameters with temperature

Consistent with its distinct room-temperature optical properties, Ce stands separate from the rest of the lanthanoids, being mostly affected by temperature through a darkening of its visible color (decrease in the *L* value), reaching an essentially black color at the highest temperature. Comparatively, the La, Pr, Nd, and Sm oxysulfides showed considerable changes in their *a* and *b* parameters (i.e., their green-red, and blue-yellow coordinates). The most abrupt color changes for these materials occur at lower temperatures for $Sm_{10}S_{14}O$, between 150 – 300 °C, in the intermediate temperature region for $Pr_{10}S_{14}O$ and $Nd_{10}S_{14}O$, between 250 – 450 °C, and $La_{10}S_{14}O$ exhibiting the higher temperature range for its most appreciable change in color, between 350 – 600 °C.

Crystal Structure

The effect of temperature on the crystal structure of all $Ln_{10}S_{14}O$ are summarized in Figure 4.2. At room temperature, these oxysulfides exhibit their characteristic tetragonal unit cells ($I4_1/acd$ space group).

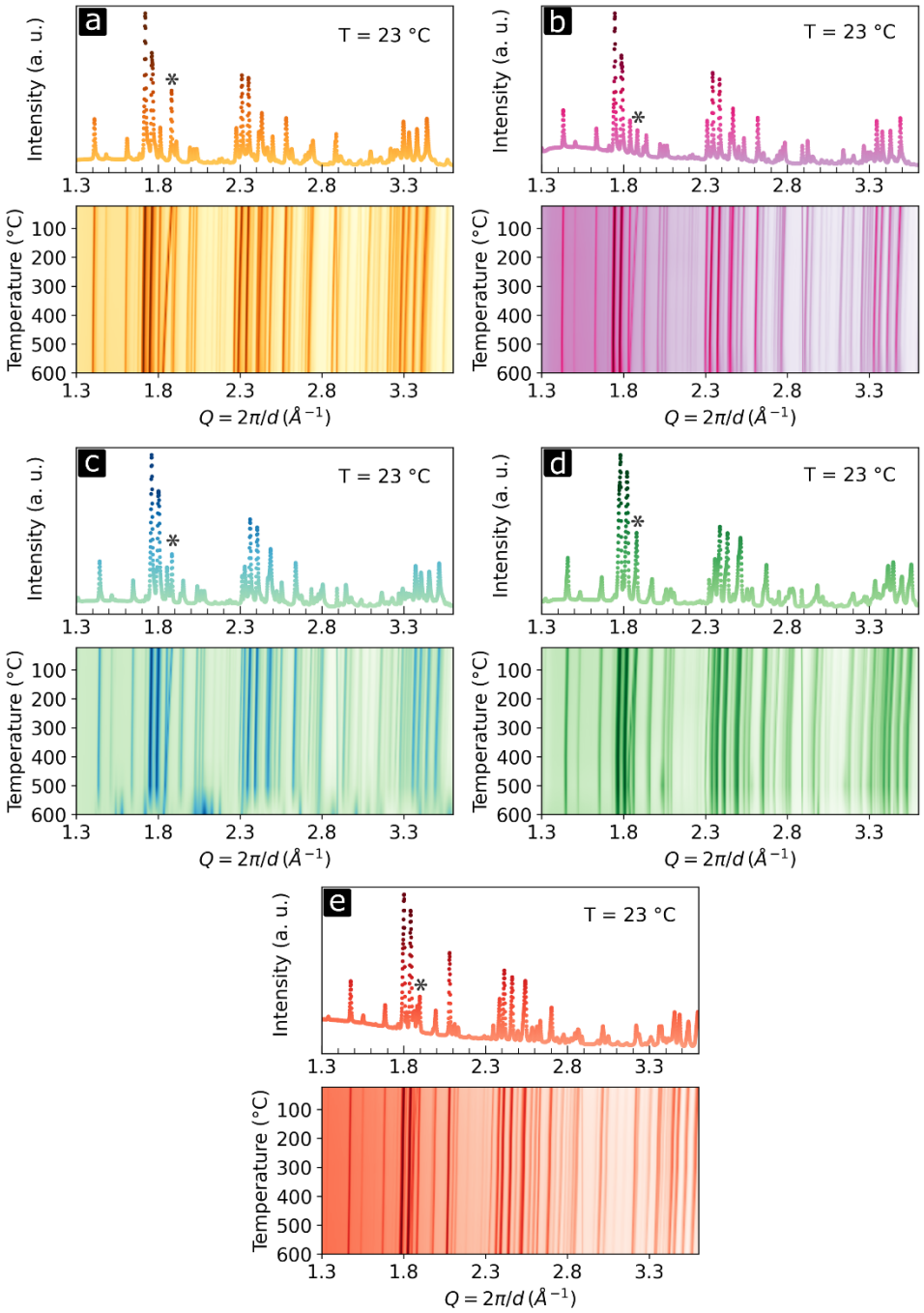


Figure 4.2. In situ X-ray diffractograms for a) $La_{10}S_{14}O$, b) $Ce_{10}S_{14}O$, c) $Pr_{10}S_{14}O$, d) $Nd_{10}S_{14}O$, and e) $Sm_{10}S_{14}O$. The top panels show the room temperature diffractograms, while the bottom panel in each pair represents color maps as a function of temperature. The more intense the color, the higher the intensity of the corresponding reflection. The ⁎ symbol identifies the characteristic peak of BN used as diluent.

Rietveld refinements (Table S4.2) show the presence of the phase $Ln_{10}S_{14.5}O_{0.5}$ for lanthanum and neodymium, which is known to form solid solutions.[17] More critically, *in-situ* PXRD shows the progressive expansion of the interplanar distance between atoms in the crystal structures with an increase in temperature, as indicated by the shift of the crystallographic reflection peaks (visualized as darker lines in the contour plots) to lower reciprocal lattice vector length, *Q*. Furthermore, there is no observation of phase changes occurring in the temperature range 24 – 600 °C. This expected expansion of the lattice parameters due to the higher vibrational energy of the atoms is summarized in Figure 4.3. Notably, all lanthanoid oxysulfides demonstrate a comparable and fairly proportional elongation of the lattice parameters *a* and *c* of their unit cells: 0.75% and 0.81% for La, 0.46% and 0.77% for Ce, 0.51% and 0.73% for Pr, 0.48% and 0.49% for Nd, 0.85% and 0.89% for Sm, respectively (measured from 600 °C vs. 24 °C – except for Nd, starting at 200 °C). In other material systems, the volumetric expansion of the unit cell or the disorder provided by the increasing thermal energy has been linked to the decrease in electrostatic interactions between ligands (O^{2-}) and metal ions (largely transition metals), consequently decreasing the degree of ligand-to-metal charge transfer (LMCT).[3,5,18] While the 5d orbitals of the Ln(III) are involved in bonding with the oxygen ions, as indicative by the characteristic narrow peaks in the O K-edge (Figure 4.4a, ca. 533 eV and 537 eV) it is less clear the degree of interaction between the lanthanoid ions and the softer S^{2-} anions, or its susceptibility to temperature. A better understanding of these interactions could be attained with *in-situ* XAS at high temperature.

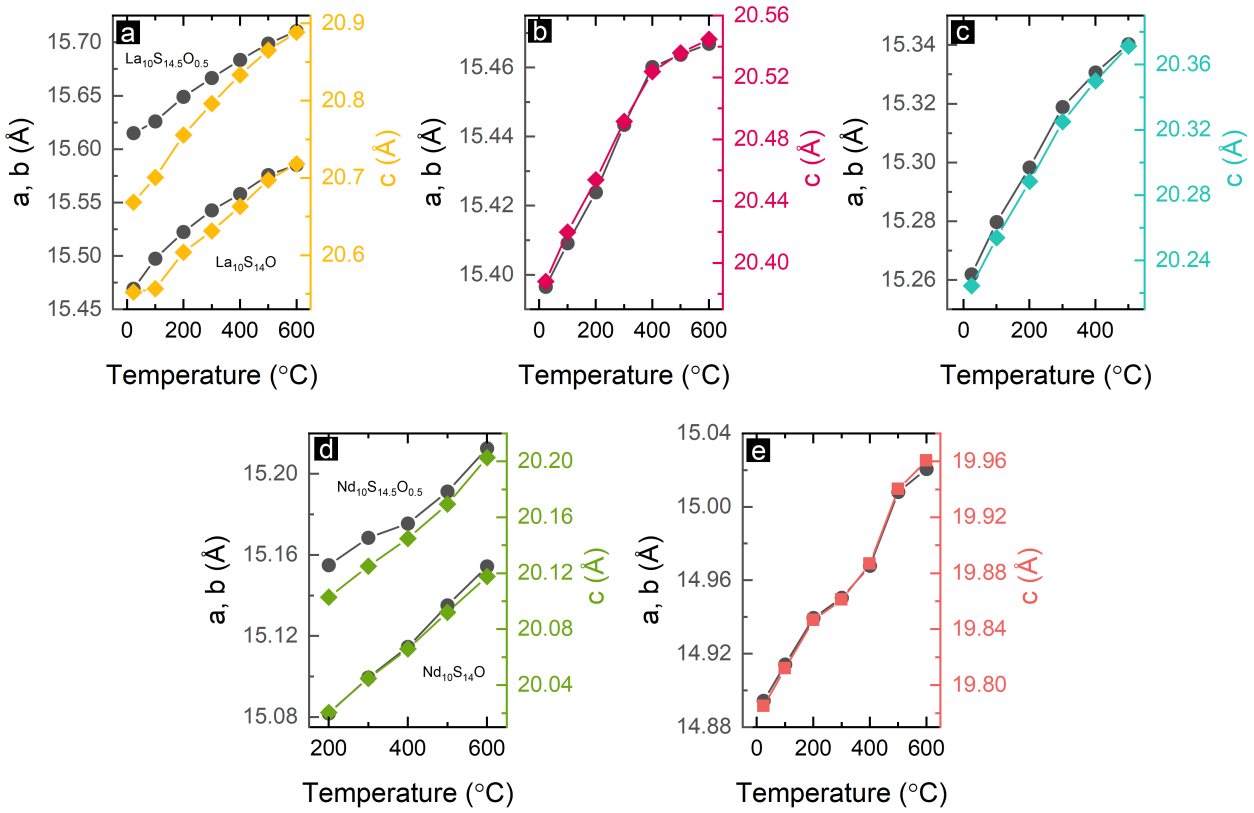


Figure 4.3. Expansion of the tetragonal lattice parameters *a*, *b*, and *c* as a function of temperature for a) $La_{10}S_{14}O$, b) $Ce_{10}S_{14}O$, c) $Pr_{10}S_{14}O$, d) $Nd_{10}S_{14}O$, and e) $Sm_{10}S_{14}O$. Both lanthanum and neodymium showed the presence of a solid solution between the corresponding nominal phase and $Ln_{10}S_{14.5}O_{0.5}$, for which cases their lattice parameters are also included. $Pr_{10}S_{14}O$ data is limited to 500 °C due to oxidation happening at 600 °C because of depletion of inert gas flow in the sample cell at the time of measurement.

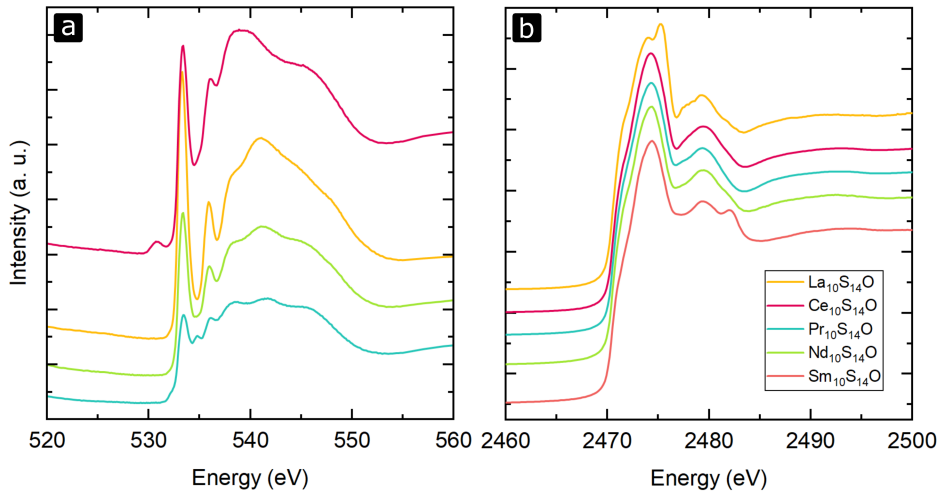


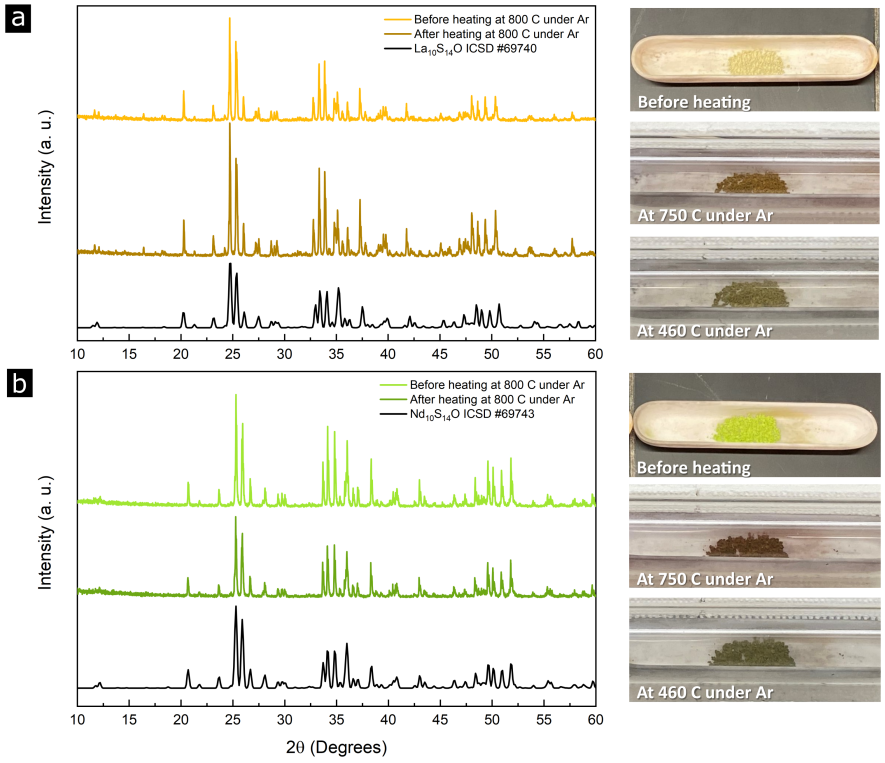
Figure 4.4. X-ray absorption near edge structure spectra corresponding to a) O K-edge, and b) S K-edge of $Ln_{10}S_{14}O$ samples at room temperature.

Reversibility and Stability

A crucial descriptor for thermochromic materials is the capacity for reversibility in their optical properties. Consistent with the detected reversibility in the observed colors, both ex-situ and in-situ powder X-ray diffraction (PXRD) heating – cooling experiments showed that these materials are also structurally reversible, with no observable changes in phase (Figure 4.5). These results further accentuate the potential applications that these materials could hold as temperature sensors.

As the ionic radius of the lanthanoids decreases, it has been shown that the estimated regions of existence of $Ln_{10}S_{14}O$ in the Ln-O-S phase diagrams decrease appreciably.[19] This in part translates in the difficulties to synthesize these oxysulfides in pure phase form. Thus, it is of fundamental value the determination of the thermodynamic stability of these phases under operating conditions. To achieve this, we conducted simultaneous differential scanning calorimetry (DSC) and thermogravimetric analysis (TGA) on two representative samples: $La_{10}S_{14}O$ and $Nd_{10}S_{14}O$ (Figure 4.6). Heating up to 600 °C revealed no characteristic endothermic signals indicative of phase changes.

Ex-situ PXRD



In-situ PXRD

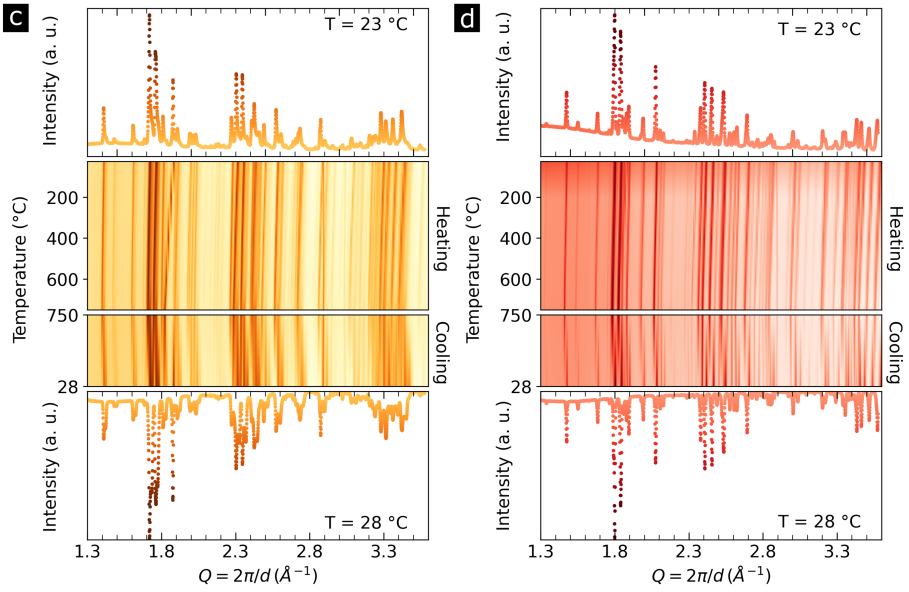


Figure 4.5. PXRD data corresponding to *ex-situ* experiments performed with a) $La_{10}S_{14}O$, and b) $Nd_{10}S_{14}O$; as well as *in-situ* studies in c) $La_{10}S_{14}O$, and d) $Sm_{10}S_{14}O$.

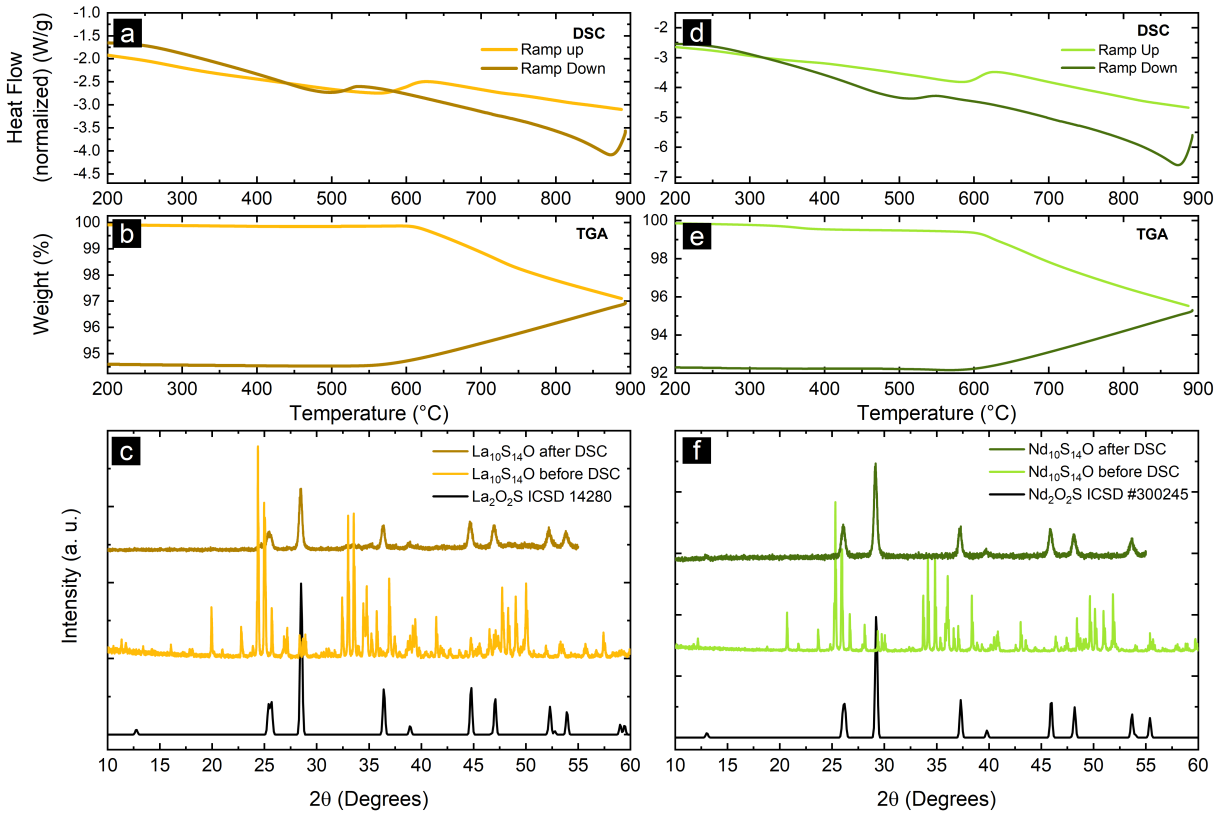


Figure 4.6. Differential scanning calorimetry, thermogravimetric analysis measurements, and PXRD performed for $La_{10}S_{14}O$ (a, b, c) and $Nd_{10}S_{14}O$ (d, e, f).

However, at higher temperatures, the progressive loss of mass identified in the gravimetric analysis in both the heating and cooling cycles (of approximately 8 %) indicated irreversible chemical changes in the oxysulfide samples. X-ray diffraction (Figures 4.6c, f) confirmed the stoichiometric conversion of the $Ln_{10}S_{14}O$ samples into the wider band gap congeners, Ln_2O_2S, with the associated color changes (from yellow to pale yellow for La, and from green to light blue for Nd). While initially conflicting with the *ex-situ* and *in-situ* reversibility studies (*vide supra*), these results indicated the presence of oxygen in the sample environment while calorimetric measurements occurred. Specifically, N_2 gas was flown over the sample, as opposed to the entire instrument being in an inert atmosphere, or the sample chamber being effectively isolated from the atmospheric oxygen. Nonetheless, these experiments were informative on the oxygen

susceptibility of these materials at high temperatures. Further tests are underway to determine the pressure of O_2 necessary to achieve this reactivity threshold and, as a result, explore their applicability as chemical sensors based on sensible color changes, as opposed to luminesce quenching[12] and resistivity.[20]

Conclusions

Within the lanthanoid oxysulfide compositional space, $Ln_{10}S_{14}O$ present multiple interesting optoelectronic properties. Among them is their colors in the visible spectrum and their change upon heating. According to color space analysis, the most dramatic color changes occur in different temperature ranges depending on the lanthanoid ion: at lower temperatures for $Sm_{10}S_{14}O$, between 150 – 300 °C, in the intermediate temperature region for $Pr_{10}S_{14}O$ and $Nd_{10}S_{14}O$, between 250 – 450 °C, and $La_{10}S_{14}O$ exhibiting the highest temperature range for its most appreciable change in color, between 350 – 600 °C. The structural changes that occur with temperature, as probed with *in-situ* X-ray diffraction, involve the expansion of the crystallographic planes up to ~1 %, with no detectable phase changes. In addition, ex-situ heating – cooling experiments showed the reversibility of said structural changes under inert atmospheres. However, calorimetric measurements showed that these oxysulfides are sensitive to oxidation with an onset at 600 °C. Further spectroscopic studies should provide the remaining necessary information to understand the thermochromism exhibited by these materials, which we believe could find applications as visible dual sensors for monitoring high temperatures reversibly, and oxygen pressures irreversibly in harsh or complex environments.

Future Work

Critical to the understanding of the fundamental origin of this thermochromic process is the study of the effect that thermal energy produces in the optical properties of these lanthanoid oxysulfides.

It is well known that both the intensity and energy position of photoluminescence bands of lanthanoids change with temperature. Indeed, this is the principle by which the majority of the ratiometric thermometry methods are based on.[21] However, most of these emissions lie in the infrared region of the electromagnetic spectrum, and much less information is available about the temperature dependance of the optical properties of visible-light lanthanoid-containing semiconductors, specifically, with regards to the contribution of the "rare-earth" ions. Due to the tendency to oxidation at high temperatures, these samples pose instrumental challenges for the acquisition of their diffuse reflectance UV-Vis spectra, with the additional complication arising from the black body radiation convoluting the data at high temperatures. It is, however, possible to obtain the band gap energy as well as information about the change in dielectric properties with temperature if a technique like ellipsometry is utilized. Provided the appropriate inert sample environments can be established, such a spectroscopic technique would be essential to the determination of the underlying electronic origin of the observed thermochromism; work that we are currently undertaking. Furthermore, given the band gap widening that occurs upon oxidation (due to the formation of Ln_2O_2S), there may be promise for these materials to act as irreversible oxygen sensors under high temperatures. This application would demand the accurate determination of the oxidation sensitivity threshold (i.e., concentrations of O_2 in the sample environment).

Experimental Method

Synthesis. All lanthanoid oxysulfides were synthesized through a high-temperature sulfurization route as described in our previous work.[22] Briefly, approximately 100 mg of lanthanoid (III) oxide or hydroxide (with exception of CeO_2) were placed inside of a tube furnace and heated under flowing Ar (forming gas for Ce) to 1100 °C. At this point H_2S gas was added to the medium (~ 10% of the reaction gas) and the reaction proceeded for ~ 1 h.

Color Space Analysis. Samples were heated inside of quartz tubes under continual Ar flow at ~ 100 sccm. After the temperature reached 700 °C, the tube furnace (Lindberg Blue M, Thermo

Fisher) was opened, and the pictures of the cooling cycle were taken. The CIE-Lab values for each lanthanoid oxysulfide were obtained after conversion from RGB with the software ImageJ, using a D65 white point.

In-situ X-ray diffraction. Lanthanoid oxysulfide powder samples diluted with BN (70 wt.% sample-to-30 wt.% BN; ground together) were introduced into 0.5 mm ID quartz capillaries (Charles Supper Company) so as to form 0.5 – 1 cm of sample length. Each powder was packed in between 2 glass wool plugs, to contain the sample while allowing gas flow. These packed capillaries were mounted on a custom heating cell, as described by Hoffman et al..[23] Diffractograms were collected at the Stanford Synchrotron Radiation Lightsource (SSRL) beamline (BL) 2-1 (0.728068 Å) under N_2 flow (16-17 psi.) with a 1.3 Tesla bend magnet and a Si(111) monochromator, providing an energy resolution ($\Delta E/E$) of 5×10^{-4}. Rietveld refinement of all diffractograms was performed with the Topas 5 software (Bruker).

Ex-situ X-ray diffraction. Diffractograms from each solid were obtained using a Bruker Eco-Advance diffractometer equipped with a Cu K_α source (1.5406 Å).

X-ray Absorption Spectroscopy. Sulfur and oxygen K-edge X-ray absorption spectroscopy was performed at the Stanford Synchrotron Radiation Lightsource (SSRL, BL 4–3 and 10-1, respectively). Samples were loaded under air, into a well equipped with Kapton windows. Measurements were performed in fluorescence mode, using a Lytle detector; a sodium thiosulfate powder sample was used for energy calibration of the S K-edge. The beamline was equipped with three ionization chambers through which N_2 gas was flown.

Thermal Analysis. Differential scanning calorimetry (DSC) and thermogravimetric analysis (TGA) were performed in a Simultaneous Dual Analyzer (TA Instruments). Between 20 – 30 mg of sample were placed on a small alumina boat. This was later equilibrated at 50 °C for 1 minute, followed by heating to 900 °C (20 °C/min), held for 1 minute, cooled to 50 °C with the same ramp, and subjected to the starting temperature for a final minute.

Supporting Information

Photographs of experimental configurations; Tables containing color space and Rietveld refinement parameters

Acknowledgements

J.M.V. thanks the University of California, Davis, for start-up funding. J.M.V. also acknowledges support from the Cottrell Scholars program supported by the Research Corporation for Science Advancement (RCSA 26780), as well as support from the National Science Foundation through the Faculty Early Career Development Program (DMR-2044403) and the Camille Dreyfus Teacher-Scholar Awards Program (TC-22-096-0). Use of the Stanford Synchrotron Radiation Lightsource, SLAC National Accelerator Laboratory, is supported by the U.S. Department of Energy, Office of Science, Office of Basic Energy Sciences under Contract No. DE-AC02-76SF00515. We would like to thank Dr. Dimosthenis Sokaras for the help provided in the acquisition of O K-edge XANES. We are grateful to Eric Campbell and Professor Luisa Whittaker-Brooks (The University of Utah) for the calorimetric and gravimetric measurements.

References

(1) Sone, K.; Fukuda, Y. *Inorganic Thermochromism*. *Inorg*. *Chem*. *concepts* Christian K. Jorgensen, Lippard, S. J., Niedenzu, K., Robert W. Parry, Eds. Springer-Verlag: Berlin **1987**, *10* (1).

(2) Warwick, M.; Binions, R. Advances in Thermochromic Vanadium Dioxide Films. *J. Mater. Chem. A*, 2014, *2*, 3275–3292.

(3) Jonane, I.; Anspoks, A.; Aquilanti, G.; Kuzmin, A. High-Temperature X-Ray Absorption Spectroscopy Study of Thermochromic Copper Molybdate. *Acta Materialia*, 2019, *179*, 26–35.

(4) Liu, H.; Qi, H.; Yuan, L.; Wang, B.; Hou, C.; Feng, S. Design Principles for 3d Electron Transfer in a Ga-Based Garnet to Enable High-Performance Reversible Thermochromic Material Color Maps. *Chemistry of Materials*, 2019, *31*, 1048–1056.

(5) Liu, H.; Yuan, L.; Qi, H.; Wang, S.; Du, Y.; Zhang, Y.; Hou, C.; Feng, S. In-Situ Optical and Structural Insight of Reversible Thermochromic Materials of Sm3-XBixFe5O12 (X= 0, 0.1, 0.3, 0.5). *Dyes and Pigments*, 2017, *145*, 418–426.

(6) Tamaki, H.; Watanabe, H.; Kamiyama, S.; Oaki, Y.; Imai, H. Size-Dependent Thermochromism through Enhanced Electron-Phonon Coupling in 1 Nm Quantum Dots. *Angewandte Chemie - International Edition*, 2014, *53*, 10706–10709.

(7) Liu, X.; Staubitz, A.; Gesing, T. M. Thermochromic Behavior of Yttrium-Substituted Bismuth Oxides. *ACS Applied Materials and Interfaces*, 2019, *11*, 33147–33156.

(8) Goforth, A. M.; Tershansy, M. A.; Smith, M. D.; Peterson, L. R.; Kelley, J. G.; DeBenedetti, W. J. I.; Zur Loye, H. C. Structural Diversity and Thermochromic Properties of Iodobismuthate Materials Containing D-Metal Coordination Cations: Observation of a High Symmetry [Bi3I11]2- Anion and of Isolated I-Anions. *Journal of the American Chemical Society*, 2011, *133*, 603–612.

(9) Zheng, B.; Fan, J.; Chen, B.; Qin, X.; Wang, J.; Wang, F.; Deng, R.; Liu, X. Rare-Earth Doping in Nanostructured Inorganic Materials. *Chemical Reviews*, 2022, *122*, 5519–5603.

(10) Runowski, M.; Wozny, P.; Stopikowska, N.; Martín, I. R.; Lavín, V.; Lis, S. Luminescent Nanothermometer Operating at Very High Temperature-Sensing up to 1000 K with Upconverting Nanoparticles (Yb3+/Tm3+). *ACS Applied Materials and Interfaces*, 2020, *12*, 43933–43941.

(11) Zhu, M.; Ma, Q.; Guo, N. Optical Thermometry Based on Europium Doped Self-Activated

Dual-Emitting LiCa3ZnV3O12 Phosphor. *Spectrochimica Acta - Part A: Molecular and Biomolecular Spectroscopy*, 2022, *271*, 120922.

(12) Borisov, S. M.; Wolfbeis, O. S. Temperature-Sensitive Europium(III) Probes and Their Use for Simultaneous Luminescent Sensing of Temperature and Oxygen. *Analytical Chemistry*, 2006, *78*, 5094–5101.

(13) Stich, M. I. J.; Nagl, S.; Wolfbeis, O. S.; Henne, U.; Schaeferling, M. A Dual Luminescent Sensor Material for Simultaneous Imaging of Pressure and Temperature on Surfaces. *Advanced Functional Materials*, 2008, *18*, 1399–1406.

(14) Sedlmeier, A.; Achatz, D. E.; Fischer, L. H.; Gorris, H. H.; Wolfbeis, O. S. Photon Upconverting Nanoparticles for Luminescent Sensing of Temperature. *Nanoscale*, 2012, *4*, 7090–7096.

(15) Amiryan, A. M.; Zolin, V. F.; Soshchin, N. P.; Tsaryuk, V. I. Thermochromic Luminophors Based on Lanthanide Oxysulfides and Oxyhalogenides. *Zhurnal Prikladnoi Spektroskopii*, 1978, *28*, 350–351.

(16) Witt, K. CIE Color Difference Metrics. *Color. Underst. CIE Syst.* Schanda, J., Ed. John Wiley and Sons, Ltd. **2007**, 79–100.

(17) Besançon, P.; Carré, D.; Laruelle, P. Mécanisme de La Solution Solide Des Oxysulfures de Terres Rares L 10 S 15– x O X. *Acta Crystallographica Section B Structural Crystallography and Crystal Chemistry*, 1973, *29*, 1064–1066.

(18) Liu, H.; Yuan, L.; Wang, S.; Fang, H.; Zhang, Y.; Hou, C.; Feng, S. Structure, Optical Spectroscopy Properties and Thermochromism of Sm3Fe5O12 Garnets. *Journal of Materials Chemistry C*, 2016, *4*, 10529–10537.

(19) Vaughan, C. M.; White, W. B. Role of Oxygen in Rare-Earth Chalcogenide

Semiconductors. *Materials Research Society Symposium Proceedings*, 1987, *97*, 397–402.

(20) Manandhar, S.; Battu, A. K.; Devaraj, A.; Shutthanandan, V.; Thevuthasan, S.; Ramana, C. V. Rapid Response High Temperature Oxygen Sensor Based on Titanium Doped Gallium Oxide. *Scientific Reports*, 2020, *10*, 1–9.

(21) Dramićanin, M. D. Trends in Luminescence Thermometry. *Journal of Applied Physics*, 2020, *128*.

(22) Wuille Bille, B. A.; Kundmann, A. C.; Osterloh, F. E.; Velázquez, J. M. Ln10S14O (Ln = La, Pr, Nd, Sm) Oxysulfides: A Series of Direct n-Type Semiconductors. *Chemistry of Materials*, 2022, *34*, 7553–7562.

(23) Hoffman, A. S.; Singh, J. A.; Bent, S. F.; Bare, S. R. In-Situ Observation of Phase Changes of a Silica Supported Cobalt Catalyst for the Fischer-Tropsch Process by the Development of a Synchrotron-Compatible In-Situ/Operando Powder X-Ray Diffraction Cell. *Journal of Synchrotron Radiation*, 2018, *25*, 1673–1682.

Supporting Information

Color Space Analysis



Figure S4.1. Photograph of experimental setup for color space analysis.

Table S4.1. CIE-Lab parameters as a function of temperature for all 5 lanthanoid oxysulfides during the cooling cycle under a flowing Ar atmosphere. (L is the lightness coordinate (L = 0 is black, L = 100 is white); a is the red-green-oriented coordinate (–a means greenness, +a means redness) b is the blue-yellow-oriented coordination (–b means blueness, +b means yellowness).

	$La_{10}S_{14}O$			$Ce_{10}S_{14}O$			$Pr_{10}S_{14}O$			$Nd_{10}S_{14}O$			$Sm_{10}S_{14}O$		
Temperature (°C)	**L**	**a**	**b**	**L**	**a**	**b**	**L**	**a**	**b**	**L**	**a**	**b**	**L**	**a**	**b**
650	49.881	11.612	40.199	3.388	10.821	3.011	29.215	5.974	13.394	26.337	4.051	17.122	20.899	8.6	5.861
600	47.596	11.06	40.778	2.817	10.332	3.162	28.451	5.694	13.171	22.968	3.287	16.238	18.104	7.955	4.856
550	44.069	8.835	40.775	2.71	8.424	3.111	24.241	4.619	14.523	29	3.233	17.926	22.678	9.13	6.694
500	47.864	5.92	42.35	3.213	8.45	3.468	28.1	4.336	15.284	27.864	2.306	20.057	22.553	10.697	7.52
450	50.756	3.128	42.827	3.357	10.636	3.363	29.902	3.103	17.231	28.352	1.143	23.141	22.714	12.762	11.052
400	53.726	-0.307	44.886	3.234	10.431	3.741	31.696	1.25	18.448	28.303	-0.808	23.515	23.243	12.828	12.603
350	57.374	-2.9	44.625	3.208	11.369	4.376	33.594	-0.385	20.336	29.115	-2.41	22.505	24.997	11.877	14.169
300	56.475	-4.321	38.686	3.438	12.525	4.69	35.768	-1.791	21.847	33.161	-3.8	23.38	28.005	12.018	17.45
250	59.154	-3.882	36.974	3.416	10.183	6.071	35.936	-3.24	21.483	34.404	-4.681	23.254	29.077	10.267	18.818
200	65.376	-3.824	35.792	3.367	12.849	6.273	38.174	-3.968	21.755	35.512	-5.526	22.363	31.681	6.456	21.634
150	62.466	-3.753	30	3.896	13.809	8.449	37.983	-4.521	21.877	33.795	-6.423	22.123	33.524	3.832	24.352
50	60.542	-1.574	22.336	6.429	13.589	11.3	36.979	-4.484	20.356	34.646	-6.892	21.112	33.524	0.581	30.307

In-situ X-ray diffraction

Cell design:

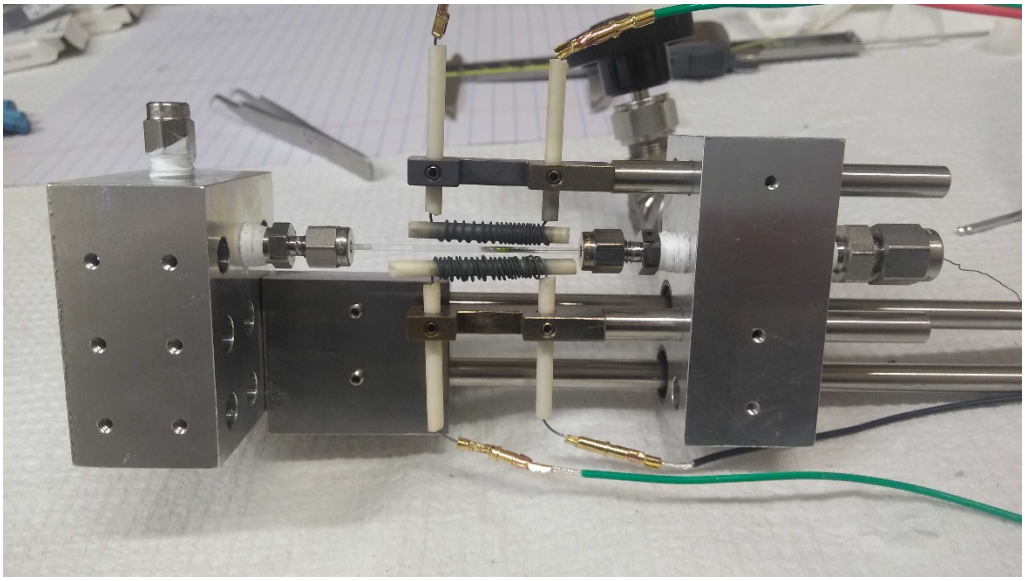


Figure S4.2. Photograph of the custom in-situ cell for the heating PXRD experiments, showing the capillary tube containing the powdered sample, flanked by two metal coils that provide the heating, as well as gas-tight connections for the inert gas flow.

Table S4.2. Rietveld refinement parameters corresponding to the data represented in Figure 4.2.

Sample	Temp. (°C)	R_{wp}	$Ln_{10}S_{14}O$	$Ln_{10}S_{14}O$	$Ln_{10}S_{14.5}O_{0.5}$	$Ln10S_{14.5}O_{0.5}$	Ln_2O_2S	Ln_2O_2S	Ln_3S_4	$Ln_{10}S_{14}O$ (%)	$Ln_{10}S_{14.5}O_{0.5}$ (%)	Ln_2O_2S (%)	Ln_3S_4 (%)
			a (Å)	c (Å)	a (Å)	c (Å)	a (Å)	c (Å)	a (Å)				
$La_{10}S_{14}O$	23	10.42	15.469	20.552	15.615	20.669	-	-	-	14.0	59.1	-	-
	100	8.53	15.497	20.557	15.626	20.701	-	-	-	15.2	51.9	-	-
	200	9.56	15.522	20.604	15.649	20.755	-	-	-	13.9	53.1	-	-
	300	9.35	15.543	20.631	15.667	20.796	-	-	-	14.6	53.1	-	-
	400	9.59	15.558	20.663	15.684	20.833	-	-	-	14.0	53.7	-	-
	500	9.96	15.576	20.697	15.699	20.865	-	-	-	15.0	53.3	-	-
	600	9.68	15.585	20.718	15.710	20.888	-	-	-	19.3	49.1	-	-
$Ce_{10}S_{14}O$	23	8.69	15.397	20.388	-	-	-	-	-	78.9	-	-	-
	100	8.23	15.409	20.420	-	-	-	-	-	73.9	-	-	-
	200	8.11	15.424	20.454	-	-	-	-	-	72.8	-	-	-
	300	7.96	15.443	20.492	-	-	-	-	-	73.5	-	-	-
	400	7.95	15.460	20.524	-	-	-	-	-	73.3	-	-	-
	500	8.01	15.464	20.536	-	-	-	-	-	75.1	-	-	-
	600	7.72	15.467	20.545	-	-	-	-	-	71.3	-	-	-
$Pr_{10}S_{14}O$	24	14.9	15.262	20.224	-	-	3.974	6.900	8.597	70.9	-	0.2	2.6
	100	15.11	15.280	20.254	-	-	3.979	6.902	8.610	70.2	-	0.2	2.5
	200	15.1	15.298	20.288	-	-	3.983	6.910	8.625	70.0	-	0.2	2.5
	300	15.14	15.319	20.325	-	-	3.987	6.917	8.640	69.7	-	0.2	2.5
	400	15.39	15.331	20.350	-	-	3.997	6.880	8.653	69.8	-	0.2	2.4
	500	14.8	15.340	20.371	-	-	4.008	6.823	8.670	70.4	-	0.6	1.4
$Nd_{10}S_{14}O$	200	7.973	15.082	20.020	15.155	20.103	-	-		44.3	25.3	-	
	300	8.78	15.100	20.045	15.168	20.125	-	-		41.7	27.3	-	
	400	8.57	15.115	20.066	15.176	20.145	-	-		38.2	31.2	-	
	500	8.8	15.135	20.092	15.191	20.169	-	-		35.2	32.6	-	
	600	9.15	15.154	20.118	15.213	20.203	-	-		38.9	29.3	-	
$Sm_{10}S_{14}O$	24	5.73	14.894	19.785	-	-	3.900	6.730	8.461	74.7		2.8	1.9
	100	6.27	14.914	19.812	-	-	3.904	6.738	8.475	74.8		2.9	2.0
	200	7.4	14.939	19.847	-	-	3.909	6.748	8.492	75.5		3.0	1.9
	300	7.84	14.950	19.861	-	-	3.911	6.753	8.499	76.8		3.1	1.8
	400	9.39	14.968	19.887	-	-	3.915	6.759	8.513	76.2		3.0	1.6
	500	9.9	15.008	19.940	-	-	3.924	6.774	8.541	59.3		2.5	1.2
	600	11.34	15.021	19.961	-	-	3.926	6.779	8.555	55.1		2.3	1.1